Abstract

Title of Document: Applications of Small Molecule-Carbon Nanotube Interactions

Jarrett Delano Leeds, Doctor of Philosophy 2014

Co-Directed By: Professor YuHuang Wang
Department of Chemistry and Biochemistry

The interactions of single-walled carbon nanotubes (SWNTs) with small molecules are critical to harnessing their remarkable electronic properties. Due to quenching effects, properties such as near infrared fluorescence are only seen in individually dispersed SWNTs. Individually dispersing SWNTs in aqueous solution using surfactants such as sodium dodecylbenzene sulfate has allowed SWNTs to be studied spectroscopically but only at low concentration. I demonstrate that by combining small molecules additives such as sucrose, trehalose, and glycerine into the surfactant dispersion process, the efficiency of the process is greatly increased. Utilizing the additive sucrose allows for the production of individually dispersed SWNT solutions at a concentration 100 times greater (up to 3.3 g/L) than the highest concentration reported previously. Spectroscopic studies suggest the small-molecule additives do not interact electronically with the surfactant-encapsulated SWNTs in solution but instead increase the solution's viscosity, slowing down Brownian motion of molecules in solution. In

solution, SWNTs move slower than surfactant molecules due to the large size difference between the two molecules. After sonication induced cavitation breaks apart a SWNT bundle, the rebundling process is slowed allowing the surfactant molecules more time to stabilize the individualized nanotubes. When dried, the nanotubes from these solutions retain their near-infrared fluorescence, indicating that the nanotubes do not become highly bundled upon solvent evaporation. While the small-molecules do not induce spectral shift in the SWNT solution spectra, in dried films these additives cause the fluorescence of individually dispersed SWNTs to red-shift by nearly 30 nm.

Wax based inkjet printing is a popular method to create paper microfluidic devices. The wax is first printed on paper and then reflowed. During reflow, the paper is heated to the wax's melting point causing the wax to wick into the paper and create a hydrophobic barrier. Wax-reflowing is an inexpensive method to create paper microfluidic devices but gives poor resolution due to a high wicking rate in the lateral direction of the paper. To demonstrate how small-molecules such as trehalose can interact with structures other than SWNTs, I studied the transport kinetics of molten wax through paper. When paper is saturated with trehalose, the wax diffuses more slowly in the lateral direction due to blockage of the transport mechanism through cellulose fibers. Transport through larger fiber-created pores is still available but is omnidirectional due to the structure of paper. This mechanism was used to create high-resolution paper microfluidic devices.

Applications of Small Molecule-Carbon Nanotube Interactions

By

Jarrett Delano Leeds

Dissertation submitted to the Faculty of the Graduate school of the
University of Maryland, College Park, in partial fulfillment
of the requirement for the degree of
Doctor of Philosophy
2014

Advisory Committee:
Professor YuHuang Wang, Chair
Professor John T. Fourkas
Professor Hugh Bruck
Professor Philip DeShong
Professor Christopher Jarzynski
Professor Amy Mullin

DEDICATION

This work is dedicated to my wife, Amy Leeds. Without her endless love, support and encouragement, I could not have persevered.

AKNOWLEDGEMENTS

I would like to thank my advisors, Prof. John Fourkas and Prof. YuHuang Wang, for their support and guidance throughout my graduate career. I feel fortunate to have them as my mentors and their encouragement has helped me to develop and expand my research skills. They serve as an inspiration to my continuous curiosity.

I would also like to extend my gratitude to all of the members of the Fourkas group, especially Dr. Rafael Gattass, Dr. George Kumi, Dr. Kathleen Monaco, Dr. Michael Stocker, Dr. Samrat Dutta and Floyd Bates II. In addition, I would like to offer my appreciation to all of the members of the Wang group, especially Dr. ChienFu Chen, Alexandra Brozena and Brendan Meany.

TABLE OF CONTENTS

LIST OF FIGURES

Chapter 1: Introduction to single-walled carbon nanotubes and their applications

In 1952, Radushkevich and Lukyanovich published scanning electron micrographs that showed tube-like carbon nanostructures.[1] However, it was only in 1991 that the nature of these species was revealed.[2] Carbon nanotubes are carbon allotropes consisting of one or more concentric cylinders where each cylinder is formed by a rolled up repeating hexagonal sheet. The structural and electronic properties of carbon nanotubes have been extensively studied since that time.[3–6] Carbon nanotubes are attractive candidates for many applications because they feature excellent mechanical strength, a Young's modulus in the TPa range,[7] heat conductivity that rivals that of diamond,[8] and photoluminescence in the near infrared.[4] Furthermore, the same molecule can be both a p-type and an n-type semiconductor.[9]

A number of practical problems have stood in the way of large-scale applications of single-walled carbon nanotubes (SWNTs). Dispersing SWNTs to high concentrations while simultaneously retaining their electronic and optical properties is crucial to many applications but remains difficult in large-scale production environments. The interactions of SWNTs with other nanotubes and dispersing agents is well understood. However, when SWNTs are used in complex solutions such as inks, the interactions of nanotubes with other types of compounds must be understood. Also, understanding how SWNTs interact with each other in dispersions as the solvent is removed is important for creating films that retain

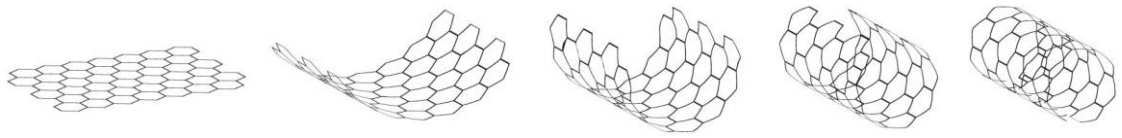

Figure 1.1. A single-walled carbon nanotube can be thought of as a graphene sheet rolled up and connected to form a hollow tube.

the properties of embedded nanotubes. Solving these problems will help SWNTs to be adopted into widespread applications.

1.1 – Structure of SWNTs

A single-walled carbon nanotube (SWNT) can be visualized as a sheet of graphene rolled up to produce a tube with a continuous hexagonal shell (Figure 1.1). The roll-up vector, $\mathbf{C_h}$, wraps around the circumference of the nanotube and is the sum of two component vectors that follow the graphene lattice and are offset by $2\pi/3$ from one another. These component vectors are integer multiples of the basis vectors $\mathbf{a_1}$ and $\mathbf{a_2}$, and are often

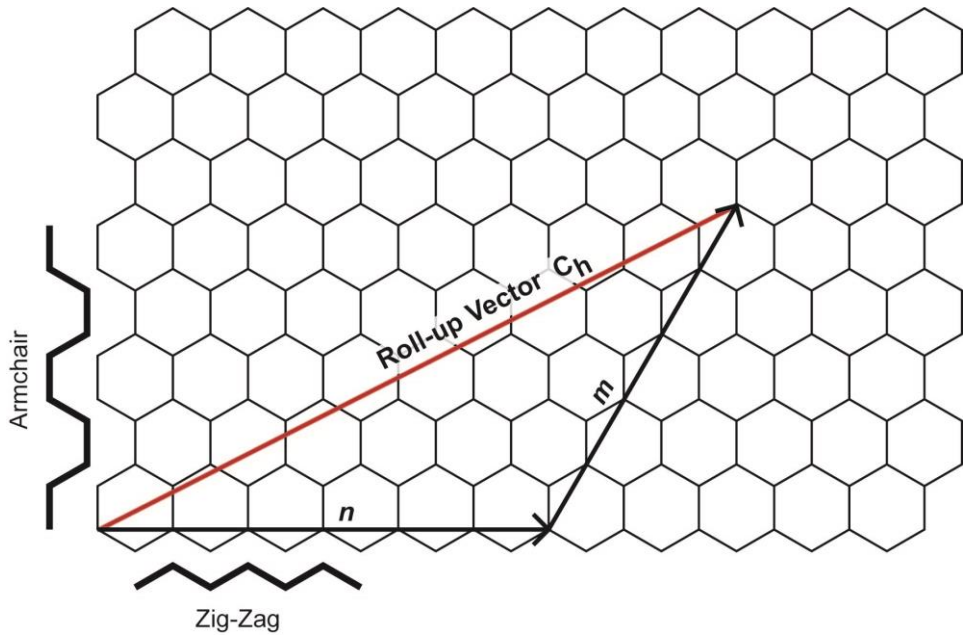

Figure 1.2. A graphene sheet showing the chiral vectors *n* and *m* and the roll-up vector C_h. The edges of the graphene show the end structures of two out of the three classes of SWNTs: zigzag (horizontal) and armchair (vertical).

denoted by their integers *n* and *m* (Figure 1.2). A common way to refer to a specific chirality of SWNT in writing is as (*n*,*m*).

As oriented in Figure 1.2, the graphene sheet contains hexagons with parallel-touching edges aligned vertically. When oriented in this fashion, the roll-up vector forms a chiral angle θ with the *x*-axis (the *n* vector) that can range from 0 to π/6. The limited range of this angle arises from the constraint that *m* cannot be greater than *n*. When the roll-up vector forms an angle of π/6 relative to the *x*-axis in the above orientation, the edge of the SWNT forms an armchair structure (Figure 1.3 A). A roll-up vector angle of 0 causes the parallel touching edges of each hexagon to be parallel to the nanotube axis. This class of nanotube is known as zigzag, due to the structure of the SWNT end. In addition, the graphene sheet can be rotated to a discrete number of angles between 0 and π/6 and rolled up to form what are known as chiral nanotubes.

A nanotube with a roll-up vector angle of $0 < \mathbf{C_h} < \pi/6$ is called chiral, because such nanotubes have non-superimposable mirror images. A given species of chiral nanotube has two different isomers, because the spiral of the primary axis down the tube can be either

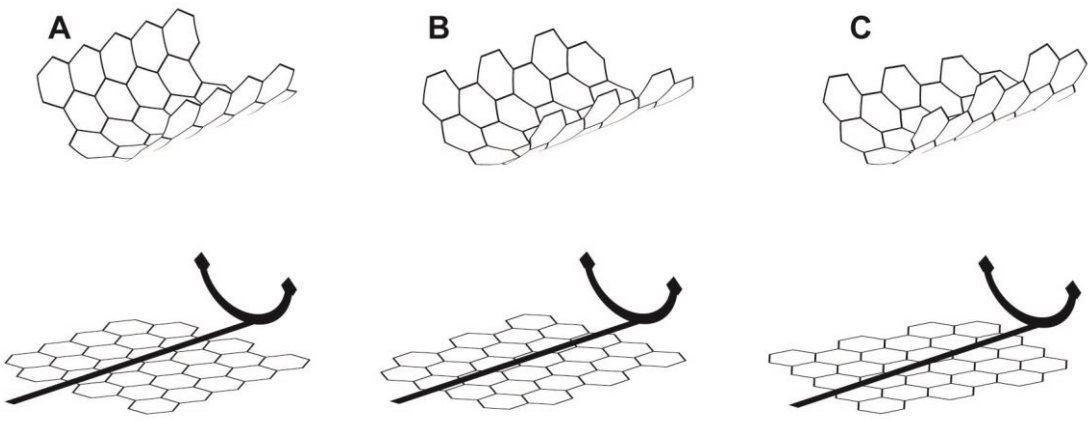

Figure 1.3. Single-walled carbon nanotubes can be grouped into three classes based on the orientation of the graphene sheet before it is rolled up. The three structure classes are (A) armchair, (B) zigzag and (C) chiral.

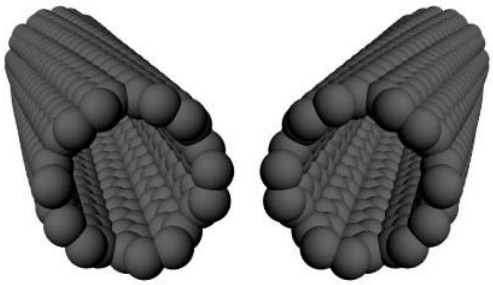

Figure 1.4. Non-superimposable mirror images of a (6,5) carbon nanotube. These structures are often denoted - (6,5) (above left) and + (6,5) (above right) as they have axes that spiral down the nanotube counterclockwise and clockwise, respectively.

left-handed or right-handed (Figure 1.4). The implications of these mirror-image species has not been thoroughly evaluated; however, they may be useful in physical applications where an electron circling, or spiraling, around a chiral nanotube generates a magnetic field.[10] In other areas of chemistry, the term *chirality* derives its meaning from its origin of handedness where molecules have different structures that are non-superimposable mirror images of one another. The term chirality as used in nanotube science refers to the vectors *n* and *m*, and is used without regard to handedness.

1.2 – Electronic properties of SWNTs

The electronic properties of SWNTs have the potential to be useful in many applications.[3] Unfortunately, the class of a SWNT is not exclusive to its electronic type. While the armchair class is exclusively metallic, chiral and zigzag SWNTs can be either semiconducting or metallic. Given the crystalline nature (or high symmetry) of SWNTs, their electronic structure is similar to that of other solid-state crystalline systems. The electronic structure in highly symmetrical materials depends not only on the repeating nature of the crystal structure, but also on any dimensional confinement of the electrons.[11] Because of their high aspect ratio (often greater than 1000) and confinement of electrons

in the circumferential direction, SWNTs can be considered to be quasi-one-dimensional structures. Rolling up a graphene sheet, such as in Figure 1.1, is a good conceptual image for the structure of a SWNT and can also be used as a model to calculate SWNT electronic structure. To understand this electronic structure, it is useful first to consider the electronic structure of graphene.

1.2.1 – Symmetry and crystal structure of graphene

Figure 1.5A shows the graphene lattice of Figure 1.2 reflected across a line rotated $\pi/6$ from the origin so that the basis vectors

$$\boldsymbol{a_1} = \left(\frac{\sqrt{3}a}{2},\ \frac{a}{2}\right) \quad \boldsymbol{a_2} = \left(\frac{\sqrt{3}a}{2},\ -\frac{a}{2}\right) \qquad \text{Eq. 1}$$

are symmetric about the *x*-axis and *a* is 0.246 nm ($\sqrt{3}$ times the carbon-carbon bond length). A primitive unit is the most basic shape (reduced form) from which the lattice can be created by repetition. Due to the periodic nature of the lattice, a Fourier transform of the basis vectors constitutes a reciprocal lattice.[11] The basis vectors used to define the reciprocal lattice are:

$$\boldsymbol{b_1} = \left(\frac{2\pi}{\sqrt{3}a},\ \frac{2\pi}{a}\right) \quad \boldsymbol{b_2} = \left(\frac{2\pi}{\sqrt{3}a},\ -\frac{2\pi}{a}\right). \qquad \text{Eq. 2}$$

The reciprocal basis vectors are also symmetric about the *x*-axis (Figure 1.5).

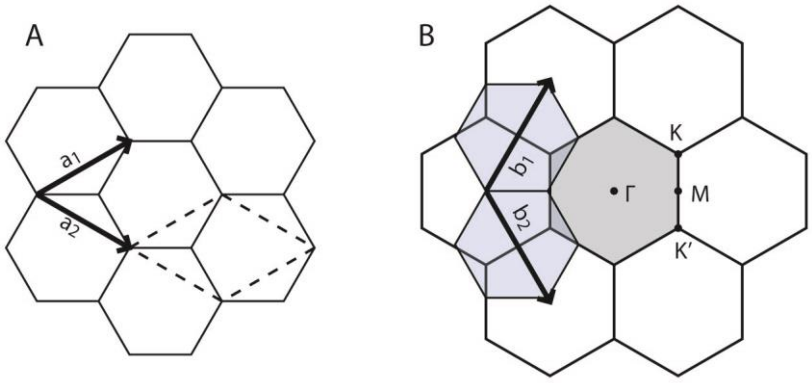

Figure 1.5. (A) Graphene lattice showing the basis vectors $\mathbf{a_1}$ and $\mathbf{a_2}$. The dashed lines represent the primitive unit cell. **(B)** The Brillouin zone of graphene (gray hexagon) within the reciprocal lattice described by vectors $\mathbf{b_1}$ and $\mathbf{b_2}$. The blue hexagons rotated $\pi/6$ represent hexagons in the graphene crystal lattice.

The Brillouin zone of a crystal structure is a primitive unit of the reciprocal lattice.[11] For graphene, the Brillouin zone is a hexagon centered at the origin and rotated $\pi/6$ from the graphene hexagon orientation (the gray hexagon in Figure 1.5B). The hexagon contains the high-symmetry points Γ, M, K and K'. K and K' together are called the K-points. The conduction and valence bands touch at the K-points, causing the highest-energy, ground-state electrons to occupy the Fermi level. The occupied energy level at the K-points is what distinguishes metallic SWNTs from semiconducting SWNTs.

1.2.2 – Symmetry and crystal structure of SWNTs

A (6,5) SWNT has a chiral angle of 26.996° between $\mathbf{C_h}$ and $\mathbf{A_1}$, as shown in Figure 1.6. A line normal to $\mathbf{C_h}$ drawn from point A will repeatedly cross through carbon atoms

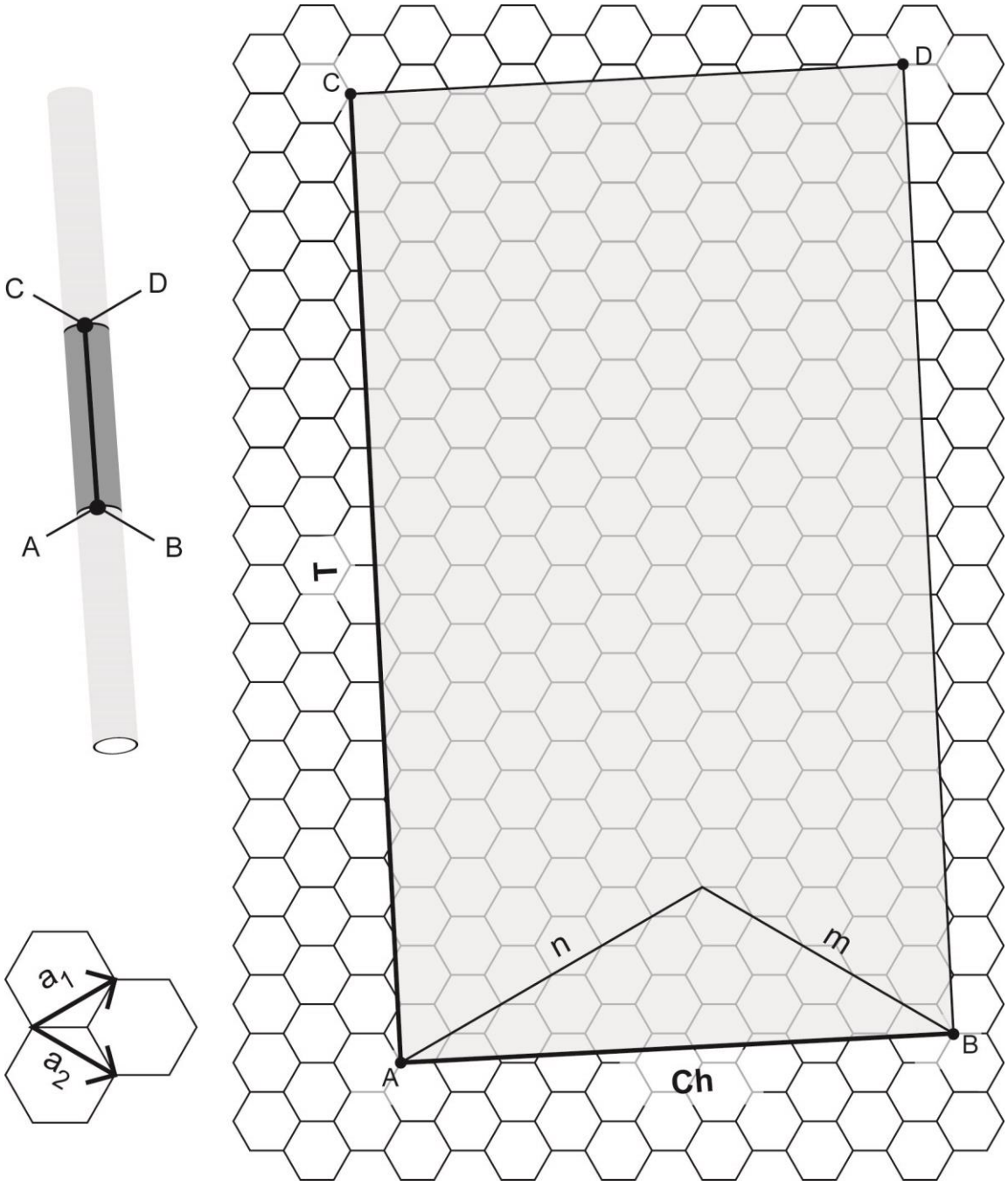

Figure 1.6. Graphene lattice showing the vectors $\mathbf{C_h}$ and **T** that form the primitive unit cell (gray area) for a (6,5) SWNT. Rolling the sheet to connect point A with B and point C with D would form one segment of the tube. $\mathbf{C_h}$ wraps around the tube and **T** is parallel to the tube axis.

on the graphene lattice, the first of which is labeled point C. The line connecting points A and C forms the vector **T** whose length depends directly on the angle θ. **T** can be found from the formula:

$$\boldsymbol{T} = (t_1, t_2) = \left(\frac{2m+n}{g_d}, -\frac{2n+m}{g_d}\right) \quad \text{Eq. 3}$$

where

$$g_d = \gcd(2m + n, 2n + m). \quad \text{Eq. 4}$$

Here, gcd denotes the greatest common denominator. The rectangle formed by the vectors $\mathbf{C_h}$ and **T** create the primitive unit cell for the (6,5) SWNT. The length of the primitive unit cell therefore depends on the chirality of the SWNT. The majority of real SWNTs are thousands of nm long and contain hundreds of repeating primitive unit cells to form a full length nanotube.

Similar to graphene, a SWNT has a Brillouin zone that is related to both the reciprocal graphene lattice and the primitive unit cell. Due to quasi one-dimensional confinement of electrons in the circumferential direction of a nanotube, the Brillouin zone s a series of cross-sections of the reciprocal graphene lattice.[3] The wave vectors of a particular chirality can be calculated using the equations:

$$\boldsymbol{K_a} = \frac{1}{N}(m\boldsymbol{b_1} - n\boldsymbol{b_2}) \quad \text{Eq. 5}$$

and

$$\boldsymbol{K_c} = \frac{\mathbf{1}}{\boldsymbol{N}}(-t_2\boldsymbol{b_1} + t_1\boldsymbol{b_2}), \quad \text{Eq. 6}$$

where *N* is the number of hexagons per unit cell:

$$N = \frac{2\boldsymbol{C_h^2}}{a^2 g_d}. \quad \text{Eq. 7}$$

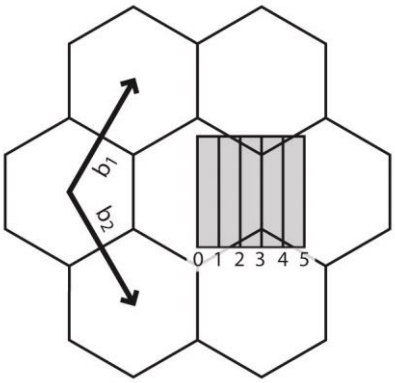

Figure 1.7. The Brillouin zone (gray region) of a (3,3) SWNT containing the wave vectors (vertical lines). Figure adapted from [11]

When combined together to form a rectangle $\mathbf{K_a} \times N\mathbf{K_c}$, these wave vectors form the SWNT Brillouin zone for a specific chirality, which has the same area as the graphene Brillouin zone (Figure 1.7). As depicted, the vertical lines within the Brillouin zone represent the allowed energy states for electrons in the circumferential direction. Starting at and centered on the reciprocal origin, there are N lines (cross-sections) in the positive $\mathbf{K_c}$ direction parallel to **T** and spaced by the length $\mathbf{K_c}$. Unlike the discrete spacing between wave vectors in the circumferential direction, the spacing between the allowed wave vectors in the axial direction approaches zero with long nanotubes.[11]

As discussed above, the valence and conduction bands touch at the K-points in the graphene Brillouin zone.[3] For a SWNT, if a wave vector crosses a K-point, then the nanotube will be metallic due to the absence of a bandgap (Figure 1.8). The distance between the Γ (origin) and the other high symmetry points can be used to determine if the distance between Γ and a K-point is an integer multiple of $\mathbf{K_c}$. For armchair nanotubes, ΓM is always an integer multiple of $\mathbf{K_c}$ and the wave vectors are parallel to KM so all nanotubes of this class are metallic. For zigzag nanotubes, ΓK is in integer multiple of $\mathbf{K_c}$

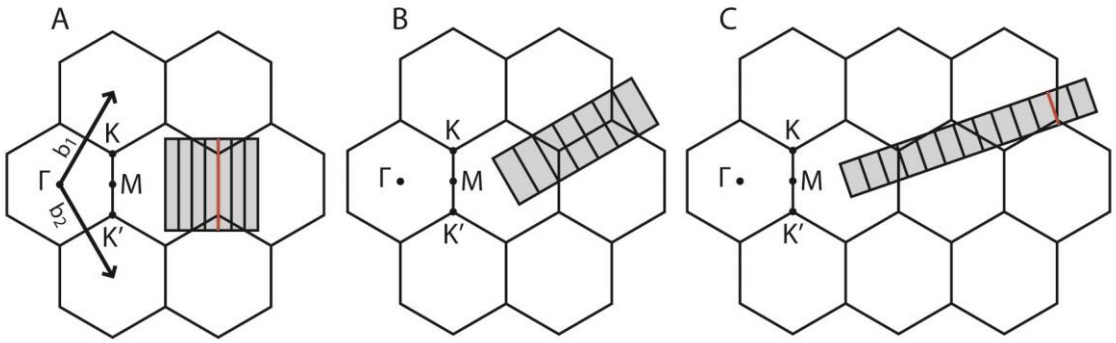

Figure 1.8. The Brillouin zones (gray regions) for (A) a (4,0) SWNT, (B) a (4,4) SWNT and (C) a (4,1) SWNT. The lines within the Brillouin zone are the wave vectors based on allowed energy states. Both the (4,0) and (4,1) nanotubes have wave vectors (red lines) that cross a high-symmetry K point and thus are metallic.

when *n* is divisible by 3. In general, if the chiral vectors *n* and *m* fit the criterion mod(2n+m, 3) = 0, then the SWNT is metallic; otherwise it is semiconducting.

1.2.3 – SWNT bandgap and density of states

The bandgap in semiconducting nanotubes is caused by the confinement of electrons in the circumferential direction and depends on the confinement length, or circumference. Thus, the bandgap is approximately inversely proportional to the nanotube diameter. The quasi one-dimensional structure of nanotubes portrays the quantum mechanical system of a particle in a box.

The density of states (DOS) is the number of available electronic states that can be occupied by electrons at allowed energy levels. The DOS is zero at low energy and rises abruptly at a critical energy due to the quasi one-dimensional structure of SWNTs. The DOS per unit length, $g(E)$, for a one-dimensional solid takes the form:[11]

$$g(E) = \begin{cases} \frac{1}{h}\sqrt{\frac{2m}{E-E_0}} & E > E_0 \\ 0 & E \leq E_0 \end{cases} \qquad \text{Eq. 8}$$

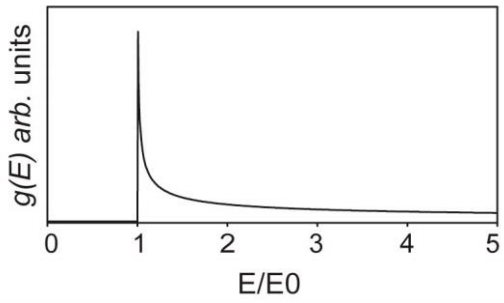

Figure 1.9. The density of states for a one-dimensional material.

where E - E_0 is the electron kinetic energy, h is Planck's constant and m is the electron mass. Eq. 8 is plotted in Figure 1.9. Note that there are no states inside the bandgap or at $E = E_0$. While $g(E)$ is zero at $E=E_0$, it diverges as the limit is approached from the left, forming what is known as a van Hove singularity. Because SWNTs have multiple wave vectors, the true electronic structure is more complicated and contains overlaid singularity structures[12] (Figure 1.10). Metallic SWNTs have a non-zero DOS at the Fermi level due to the conduction band touching the valence band at the K-points (Figure 1.10 B).

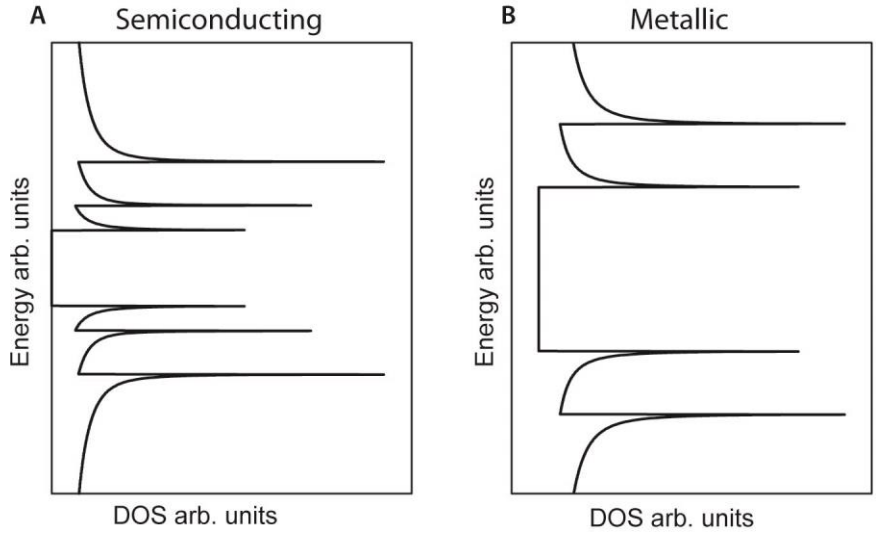

Figure 1.10. The DOS for SWNTs. (A) A semiconducting nanotube that has a bandgap at the Fermi level. (B) A metallic nanotube whose valence and conduction bands touch, resulting in the absence of a bandgap.

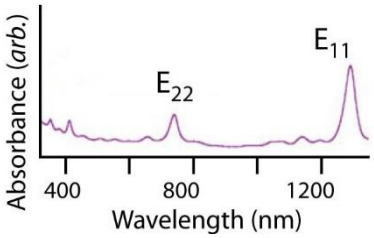

Figure 1.11. The absorption spectrum of a (8,7) SWNT showing the sharp van Hove transitions associated with the nanotubes' electronic structure. Adapted from ref [29]

1.2.4 - SWNT absorption properties

In a SWNT, electronic transitions occur symmetrically across the Fermi level from one singularity to another, due to the high DOS at the singularity. When SWNTs are individually dispersed in solution, these transitions cause sharp peaks in the absorption spectrum (Figure 1.11). The peaks are known as van Hove transitions and are labeled E_{11}, E_{22}, and so on. The sharpness of the peaks is an indication of the percentage of individually dispersed SWNTs in solution. SWNT bundles do not have sharp absorbance features. The structure of an optical absorption spectrum also provides a fingerprint to identify which chiralities of nanotubes are present. However, many species have transitions that overlap with one another. Overlapping peaks in a spectrum can make analysis difficult (Figure 1.12).

1.2.5 – SWNT photoluminescent properties

An exciton is created when a photon with an energy matching the gap between singularities is absorbed by a SWNT. Many pathways exist for the electron to get back to the ground state and re-combine with the hole.[13] For metallic SWNTs, the absence of a bandgap allows the nanotube to relax to the ground state through non-radiative decay. In

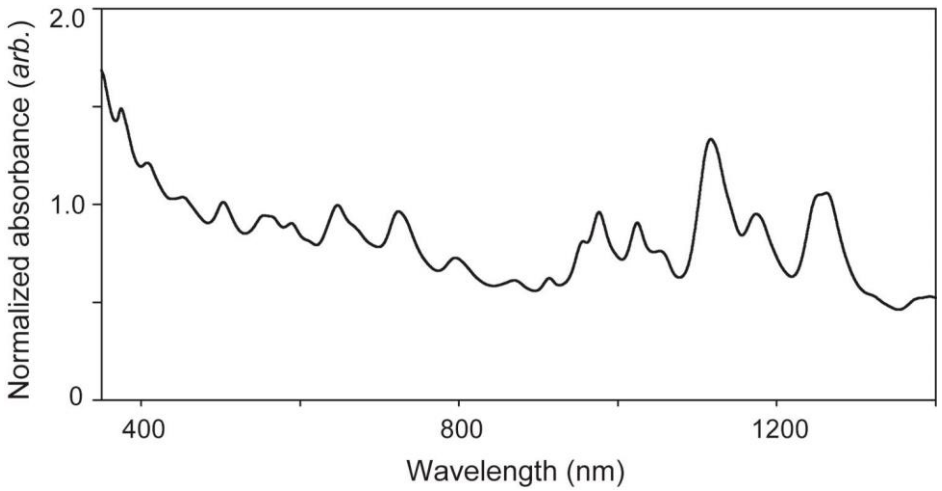

Figure 1.12. The absorption spectrum of HiPco-synthesized SWNTs dispersed in sodium dodecylbenzenesulfate (SDBS). The large number of chiralities in solution causes individual van Hove transitions with similar energies to overlap. The sharpness of the absorption peaks is an indication that the nanotubes are individually dispersed in solution.

semiconducting nanotubes, however, the bandgap makes it possible for an excited electron to lose energy through radiative decay. The photon released during fluorescence has the same energy as the E_{11} transition, which, for many chiralities, is in the near infra-red (NIR) part of the spectrum (between 800 nm and 1600 nm). The 2-D, excitation-emission spectra allow for easy identification of specific chiralities of SWNTs in solution, even when a large number of chiralities are present.

1.2.6 – Quenching of electronic properties

The quantum yield of SWNT photoluminescence is small, typically less than 1%.[14] While quenching caused by collisions between SWNTs and solvent molecules does occur, a more important quenching mechanism is SWNT bundling, especially with metallic nanotubes.[4] Historically, the low luminescence quantum yield of SWNTs made it difficult to obtain detailed emission spectra.[15] SWNTs can now be individually dispersed and

detailed spectra are readily measured. Quenching through bundling can thus be advantageous as it tells the quality, or percentage of individual dispersed SWNTs, of the solutions of nanotubes.

1.3 – Synthesis of SWNTs

Several techniques exist for manufacturing carbon nanotubes. The two most common techniques are the high-pressure carbon monoxide (HiPco) method and the cobalt metal catalyst method (CoMoCat). Together, these techniques produce the most widely available SWNT material. While the CoMoCat process can be finely tuned to provide an enrichment of certain chiralities, including (6,5) and (7,6), the end product still contains a small percentage of other chiralities. A wide distribution of chiralities is created in the HiPco process, with no single species in major proportion. No known synthetic method produces a single species of SWNT.[16]

A problem that arises during the synthesis of SWNTs is bundling. Typically, van der Waals forces between molecules are weak compared to other intermolecular forces such as hydrogen bonding and dipole interactions. However, the cylindrical shape and high aspect ratio of SWNTs enables a large number of carbon atoms to be in close proximity in a nanotube bundle. Therefore, the energy needed to break van der Waals forces holding SWNTs in a bundle are on the order of 8×10^{-17} J per μm of nanotube contact.[6,17]

1.4 – Dispersions of SWNTs

To work with SWNTs, typically they must first be dispersed in solution. Dispersion increases the safety of working with nanostructures by preventing them from becoming airborne. Dispersion also allows for the removal of impurities from the raw material. The weak interactions of the SWNTs with most solvents can make solution dispersion a difficult task. No true thermodynamic solvent is known for SWNTs, so energy must be used to break up nanotube bundles.[18]

Many physical properties of SWNTs have been studied at the single-molecule level, and for many applications it is desirable to have such individualized nanotubes. For example, the high reported mechanical strength of SWNTs is based on studies of individual nanotubes. When nanotubes are bundled together, the van der Waals interactions holding the bundles together limit the overall tensile strength. The electronic properties of nanotubes in bundles also become mixed and, if metallic tubes are present, the semiconducting properties can be quenched completely.

1.4.1 – Solvation of SWNTs

Spontaneous solvation of a solute can occur in a true thermodynamic solvent. With such a solvent, the amount of energy required to break a solid out of its lattice is less than the free energy of solvation. Since SWNTs cannot be solvated spontaneously, the energy required for dispersion must come from a different source. Electrostatic charging of SWNTs by oxidation or reduction causes the nanotubes to repel one another. SWNT oxidation can be achieved with superacids such as chlorosulfonic acid[19,20] or oleum.[20] Reduction can take place in a non-quenching solvent such as anhydrous ammonia with a

solvated-electron source, such as elemental sodium or lithium.[21,22] However, electrostatically charged nanotubes rebundle if the charge is quenched. *In-situ* stabilization by surfactants or polymers is not possible, because the stabilizers are incompatible with the harsh chemical environment. The electronic properties of SWNTs are also changed under these chemical conditions.[23] Thus, the use of electrostatic dispersion is usually limited to predispersion for covalent functionalization or to applications in which changes in the electronic properties are not of consequence.

Mechanical exfoliation (i.e., the input of mechnical energy) can also be used to solvate nanotubes. High-shear mixing can predisperse SWNTs by breaking up large bundles. High-power ultrasonication (discussed further in Chapter 2) can be used to break apart bundles into individual nanotubes. With mechanical exfoliation, a stabilizing agent can be included during processing, helping to increase the efficiency of the process by preventing rebundling. Care must be taken when using mechanical exfoliation, because high powers and extended processing periods can lead to drastic shortening of the nanotube lengths.[4] However, if some shortening of tubes can be tolerated, mechanical exfoliation is a favorable processing tool that can produce individualized nanotubes that are stable over a time scale of months.

1.4.2 – Stabilization of individualized SWNTs

SWNTs can be encapsulated with surfactants or wrapped with polymers to increase their interaction with polar solvents and stabilize them against rebundling. Encapsulating with surfactants such as sodium dodecylsulfate (SDS) or sodium dodecylbenzenesulfate (SDBS) is a common and inexpensive way to disperse nanotubes.[5] Other surfactants can

provide better results than SDS/SDBS, but at an increased cost. Wrapping with DNA,[24] polymers[25,26] or chitosan[27] can also provide stable nanotube solutions at moderate concentrations. However, polymers are difficult to remove cleanly and the use of DNA can be cost-prohibitive.

SDS molecules prefer to lie along the secondary (zigzag) nanotube axis and, in chiralities in which this axis is bent along the curve of the SWNT, the surfactant molecules interact less with the nanotube. The difference in interaction among different nanotube structures is small but it is large enough be used to separate SWNTs by chirality.[28] In addition, DNA oligomers with certain sequences prefer to wrap around specific chiralities of SWNTs. This preference for certain SWNT species has been used successfully to isolate certain chiralities of SWNTs to a high purity.[29] However, separating SWNTs with DNA produces small quantities of purified nanotubes and finding the proper oligonucleotide sequence for each chirality is time consuming. The number of chiralities that have been separated using this technique is therefore limited.

1.4.3 – Removal of contaminants

Mechanical exfoliation/surfactant encapsulation has a low yield for nanotube dispersion. Typically, less than 5 mass% of SWNTs are individualized, leaving a large quantity of bundles as contaminants.[5] Amorphous carbon and catalyst particles are also suspended in solution. These contaminants can be removed by density sorting in an ultracentrifuge. When encapsulated by SDS, the catalyst particles and amorphous carbon have the highest density, followed by bundled SWNTs and then individual SWNTs. For encapsulated individualized SWNTs, the density depends on the chirality, and ranges from

1.055 to 1.110 g/ml.[10] During ultracentrifugation, the suspended particles settle to their respective isopycnic points. If D_2O is used as the solvent, then the isopycnic point for the individualized tubes is above that of the pure solvent. If H_2O is chosen, then the isopycnic point of individualized SWNTs is below that of the solvent. With both of these solvents, a time is chosen that is long enough to force the higher-density contaminants out of solution but short enough that the individualized tubes will stay in solution. Fractionation allows individualized tubes to be collected with high purity.

1.4.4 – Self-contamination of SWNTs

As synthesized, nanotube material contains not only catalyst, amorphous carbon, and bundled nanotubes, but also multiple species of SWNTs. Ultracentrifugation can remove non-nanotube species and nanotube bundles; however, the remaining solution is a mixture of SWNT species. This mixture of species is detrimental for many applications. For example, in an application requiring a high electrical-conductivity-to-weight ratio, it is desirable to use only metallic nanotubes. However, as synthesized, approximately 2/3 of nanotubes are semiconducting.[11] The same problem holds true for applications of semiconducting nanotubes, especially when a single chirality is desired.

1.5 – Scaling to mass production

Individual dispersion of nanotubes is generally feasible at the research level. However, it has proven difficult to scale the techniques used in the research laboratory up to an industrial level. Most applications require a higher concentration than can be

achieved with traditional surfactant dispersion.[30] In addition, steps such as film drying can cause aggregation.

1.5.1 – Concentration of dispersed SWNT solutions

The low yield of mechanical exfoliation makes it difficult to achieve highly concentrated and individually dispersed SWNT solutions. Typically, concentrations in the low mg/L range are produced in research laboratories. For many applications, concentrations in the g/L range are required. In principle, the amount of starting material could be increased. However, the cost of the raw material can be prohibitive. In Chapters 2 and 3, I discuss ways to generate higher concentrations of individually dispersed SWNTs.

1.5.2 – Aggregation of dried SWNT solutions

When forming films or coatings from individually dispersed SWNT solutions, the nanotubes often bundle as the film dries.[31] While the surfactant molecules are good at decreasing the interfacial surface tension between SWNTs and water, the molecules are unable to do the same in air. Nanotubes aggregate and their optical properties change as a solution of individually-suspended SWNTs surfactant dries. Chapter 3 discusses a way to hold the SWNTs in place as the film dries to prevent aggregation and Chapter 5 presents a detailed study of the interaction of SWNTs in a dry film.

1.6 – Thesis outline

The goal of the work presented here is to develop a better understanding of the interactions between single-walled carbon nanotubes and small molecules. The focus of

the work is on using interactions between sugars and SWNTs to increase the concentration of individually dispersed nanotubes (Chapters 2 and 3). The optical properties, including absorption, photoluminescence and printed contrast ratio of SWNTs in highly concentrated solutions are studied both in solution and following inkjet printing (Chapters 3 and 4). The ability of printed SWNT solutions to fluoresce after drying is significant, and the interactions after drying are evaluated in depth in Chapter 5. Chapter 6 presents studies of similar systems in which cellulose rod structures (paper fibers) interact with the same sugars to control the kinetic material transport rate, or bleeding, through the paper structure. Chapter 7 presents future directions for the work.

Chapter 2: Preparing solutions of individually-dispersed SWNTs

As discussed in Chapter 1, to take advantage of many SWNT properties, the nanotubes should be individually dispersed in solution. A number of methods have been developed for dispersion of SWNTs, with varying success.[5,21,24,32–35] The most promising of these methods is surfactant dispersion using high power sonication[36] followed by ultracentrifugation.[4] While solutions processed in this way contain almost exclusively individualized nanotubes, the yield is typically 5% at most.[5] In Chapter 2, I discuss two methods to increase the efficiency of SWNT dispersion with surfactants: Using a more efficient surfactant and controlling the solution temperature during processing.

2.1 - Surfactant molecules

A surfactant molecule contains two distinct regions, one that is polar and one that is non-polar. Typically, surfactants have a small polar head region that interacts well with polar solvents. The remaining part of the molecule, often referred to as the tail, makes up the non-polar region. When surfactants are placed in a solution containing a polar and a non-polar solvent, the surfactant molecules help to reduce the surface tension between the solvents. This interfacial activity is the source of the term *surfactant*, which is a contraction for surface active agent.

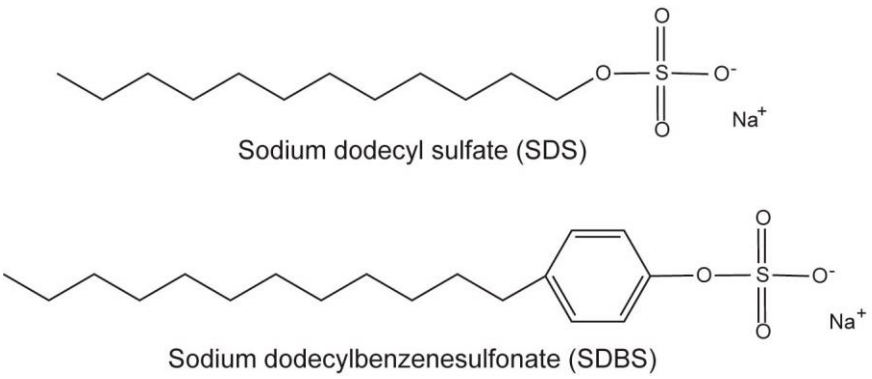

Figure 2.1. Sodium dodecyl sulfate (SDS) and sodium dodecylbenzenesulfonate (SDBS) are common surfactants that can be used to encapsulate and disperse single-walled carbon nanotubes.

One of the most readily available surfactants found in many consumer products is sodium dodecyl sulfate (SDS). SDS is an amphiphilic molecule containing a polar sulfate head group and a non-polar, twelve-carbon alkyl tail (Figure 2.1). At low concentration in a solution with two phases of solvent , SDS molecules accumulate at the interface between the two solvents to lower the surface tension between the solvents. If a system consists of only a polar solvent, then surfactant molecules will accumulate at interfaces; either the solution-container (for a hydrophobic container) interface or the solution-atmosphere interface (Figure 2.2). Above what is known as the critical micelle concentration (CMC), the surfactant concentration becomes high enough that a global energy minimization can

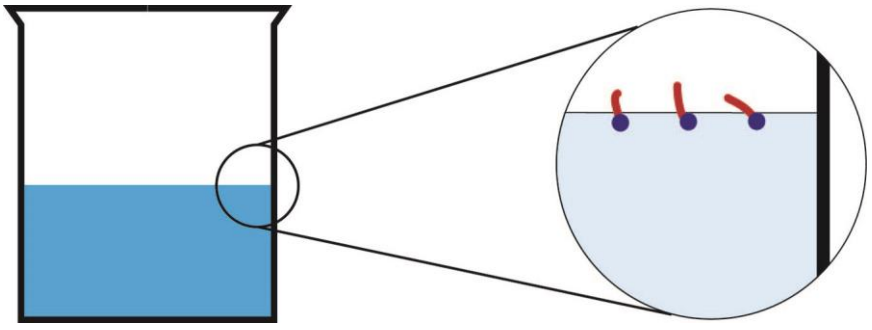

Figure 2.2. Surfactant molecules in a polar solution lower the interfacial tension by placing their tails at the interface between the solution and air.

occur if SDS molecules interact with themselves, thus forming an ordered structure known as a micelle. Micelles feature an internal, non-polar region and an external, polar shell

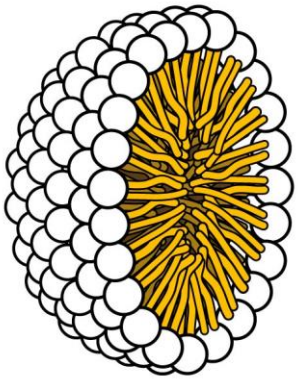

Figure 2.3. Schematic cross section of a micelle showing the internal non-polar sphere and external polar shell. Image courtesy of Wikimedia Commons.

(Figure 2.3). Above the CMC, the concentration of free surfactant molecules becomes constant. Any increase in the surfactant concentration creates more micelles. All surfactants exhibit a CMC, but its value depends on the surfactant and conditions such as temperature.[5] In a mixture of polar and non-polar solvents, micelle formation around small volumes of non-polar liquid help to decrease the interfacial tension between a polar and a non-polar liquid, creating an emulsion.

It might be expected that surfactants would form micelle-like structures around SWNTs in solution. It has been observed, however, that the surfactant tails interact with the nanotube but a micelle-like structure is not formed.[37] Even at concentrations below the CMC, SWNTs can be dispersed in surfactant solutions indicating a different surfactant encapsulating geometry than micelles.[38] Functionalized SDS was shown to from hemimicelles on SWNTs.[39] TEM experiments showed that short-chain polymers containing benzene moieties also form a hemimicelle structure on graphatic surfaces.[40]

However, molecular simulations have shown that surfactant molecules form a compact, disordered structure on SWNTs due to the surfactant molecules lying flat against the nanotube sidewall.[37] In both hemimicelles and disordered systems, surfactant molecules lay flat against the SWNT sidewall. Due to this flat orientation, a surfactant molecule containing benzene ring(s) such as SDBS should do a better job of dispersing nanotubes because of π-π stacking between the structures.[30]

SDBS is a close analog to SDS, but contains a single benzene ring between the tail and head (Figure 2.1). Previous work has suggested that SDBS is more efficient at dispersing SWNTs than SDS; however, the linearity of the mass conversion of raw SWNT material to individually dispersed SWNTs has only been reported for low concentrations of SWNTs.[5] Islam *et al*. suggested that SDBS could be used to disperse SWNTs to a concentration near 20 g/L with 63% individualized nanotubes.[30] While sonication was used to achieve these results, centrifugation was not employed to remove bundles. The estimate of final dispersed SWNT concentration was based on the initial mass of HiPco material added to solution. In addition, the percentage of individually dispersed nanotubes was based on the number of AFM-resolved features rather than on the mass of SWNTs. The reported percentage is therefore only a count. To convert the count to mass base, one must account for the nanotube length, tube diameter and bundle size. It was also assumed that the largest individually dispersed nanotubes had a diameter of 1.3 nm. HiPco materials typically have a diameter range from 0.6-1.3 nm with an average of 0.93 nm.[12] The AFM results are skewed toward 1.3 nm diameters, suggesting that most of the features between 1 nm and 1.3 nm are in fact small bundles. Based on these issues, it is likely that the concentration of individualized tubes was below 1%. Such a value is consistent with later

experiments of Moore *et al.*, who reported a 3.9% yield[5] and of Matarredona *et al.*, who reporteded a maximum concentration of ~0.25 mg/mL.[41]

Specialized surfactants have also been used to disperse SWNTs. For instance, surfactants that feature non-ionic hydrophilic regions composed of materials such as polyethylene(oxide)[42] are preferred for biological applications. While some of these surfactants give higher yields than SDS and SDBS when processing SWNTs,[5] they are more expensive than SDS and SDBS.

2.2 – Sonication

Sonication can be used to induce erosion or exfoliation of solid materials through cavitation.[43] Due to the large amount of energy involved in sonication, sample temperatures can increase dramatically, especially for high-power, probe-tip sonicators. This Section provides details about the sonication mechanism and the specific equipment used to disperse SWNTs individually.

2.2.1 - Mechanism

During sonication, a probe surface oscillates at a frequency that is usually in the range of 20-40 kHz. This oscillation drives sound waves in the solution, creating propagating regions of high pressure and low pressure (Figure 2.4). As the low pressure section of the wave passes through a region of the solvent, the solvent experiences tension. Cavitation can occur in the low-pressure regions, especially in the presence of dissolved gas or surface defects, which lower the threshold for cavity nucleation.[43] When the propagating high-pressure region of a wave encounters a void, implosion can occur. Voids

smaller than a critical size of approximately 170 μm are more likely to implode.[43] Implosion of a void releases energy which can overcome the van der Waals forces between nearby bundled SWNTs, causing exfoliation.

2.2.2 - Temperature effects of sonication

Sonication can heat a sample substantially, which can disrupt the sonication process or even destroy the sample. During sonication, the power provided to the probe is typically on the order of 10-100 watts. Some of this energy is absorbed by the sample. At room temperature, neglecting energy flow to the surroundings by convective and conductive cooling, sample exfoliation and loss in the sonicator, a 10-W sonicator can increase the temperature of 50 mL of water by 10 °C in 3.5 minutes. For this reason, it is important to have an efficient way to remove excess heat, especially as sonication processing times for nanotube exfoliation are typically many hours.

Temperature control is also important for efficient and reproducible sonication. At high temperature, dissolves gases come out of solution. Dissolved gases act as nucleation point for the creation of voids so their removal decreases sonication efficiency.[43] The speed of sound is a function of temperature. Inconsistent temperature will therefore cause a

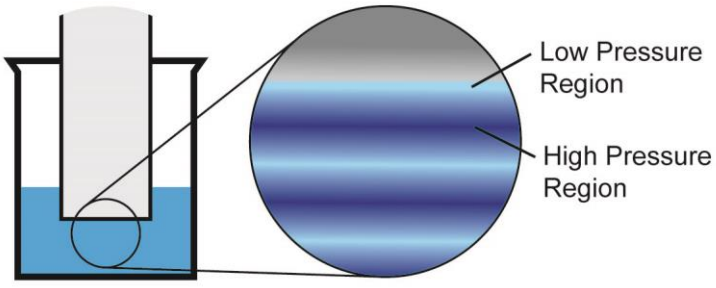

Figure 2.4. Sound waves created by the sonicator probe tip generate alternating regions of high and low pressure in the medium.

variation in the sound propagation speed causing the sonication characteristics of the solution to change. This is especially true with increases in temperature where the decrease in the speed of sound can allow voids to grow past the critical void size preventing implosion.[43] It is therefore desirable to maintain a constant temperature during sonication.

2.2.3 – Misonix Sonicator 4000

A Misonix 4000 Ultrasonicator was used to exfoliate bundled nanotubes. This sonicator creates high-intensity sound at a frequency of 20 kHz. The sonic energy is focused using a mechanical amplifier to enhance the oscillation amplitude at the tip. The Misonix uses a feedback loop to maintain a constant probe oscillation amplitude. Ideally, a constant amplitude gives more reproducible results under varying conditions, such as slight changes in temperature, atmospheric pressure and viscosity.

The Sonicator 4000 has a ½-inch probe tip for direct-coupled sonication and a 2-inch cup-horn for indirect sonication in temperature-controlled systems (Figure 2.5 and Figure 2.6). The probe tip has the advantages of a higher amplification and direct coupling of the tip to the solution being sonicated, resulting in better energy transfer to the sample solution. Direct coupling has the disadvantage of introducing contaminants including titanium nanoparticles from tip consumption during sonication. Direct coupling also requires a direct-flow cooling system such as a temperature-controlled jacket to cool the sample properly during operation. The cup-horn setup is indirectly coupled to the sample through a cooling solution, resulting in a lower chance of contamination, as the only contaminant source is erosion of the sample container itself. The disadvantage of the cup-

horn is that sound waves must be transferred through the sample container, where much of their intensity is lost.[44]

During sonication, the sound amplitude can be adjusted in real time. In addition, the system monitors power, total energy delivered, and the program process. The system allows for samples to be processed in a continuous sonication mode or a pulsed mode. During the dead time in the pulsed mode, any cavitated bubbles larger than the critical diameter can exit the sample and the sample can cool.

2.2.4 – Cooling Jacket Design

Due to the inefficient coupling of the cup-horn sonicator and the need to keep temperature stable during sonication, an aluminum cooling jacket that fits a 100-mL stainless steel beaker was designed and fabricated. Stainless steel provides better heat

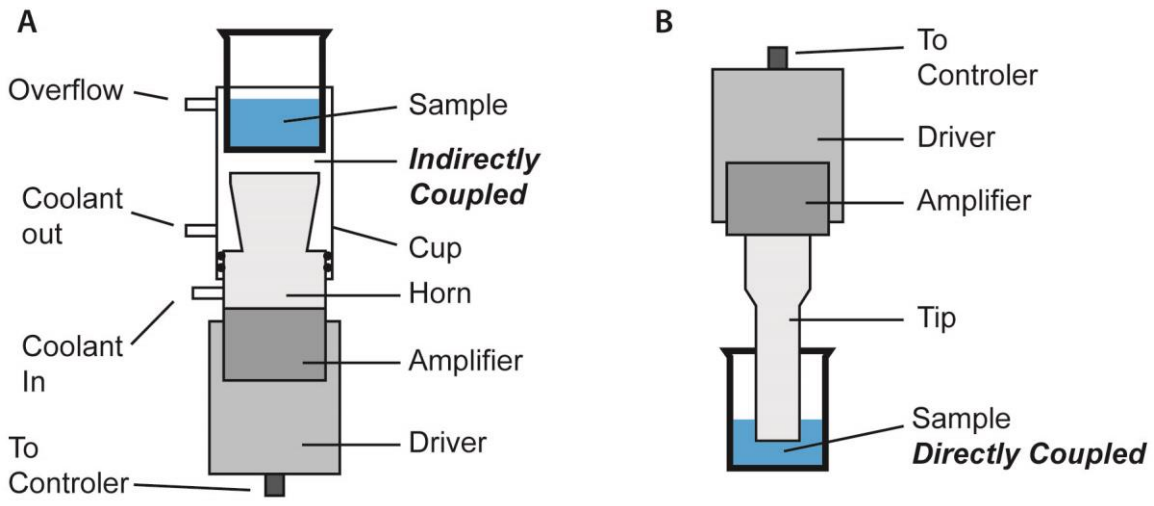

Figure 2.5. Two different setups for the Misonix Sonicator 4000 Ultrasonicator. (A) The cup-horn setup has better temperature control but indirect coupling of the probe to the solution causes the power received in the sample to be low. (B) The probe tip setup has extremely good energy transfer into the sample due to the direct coupling of the tip immersed in the sample. This setup requires a separate cooling system.

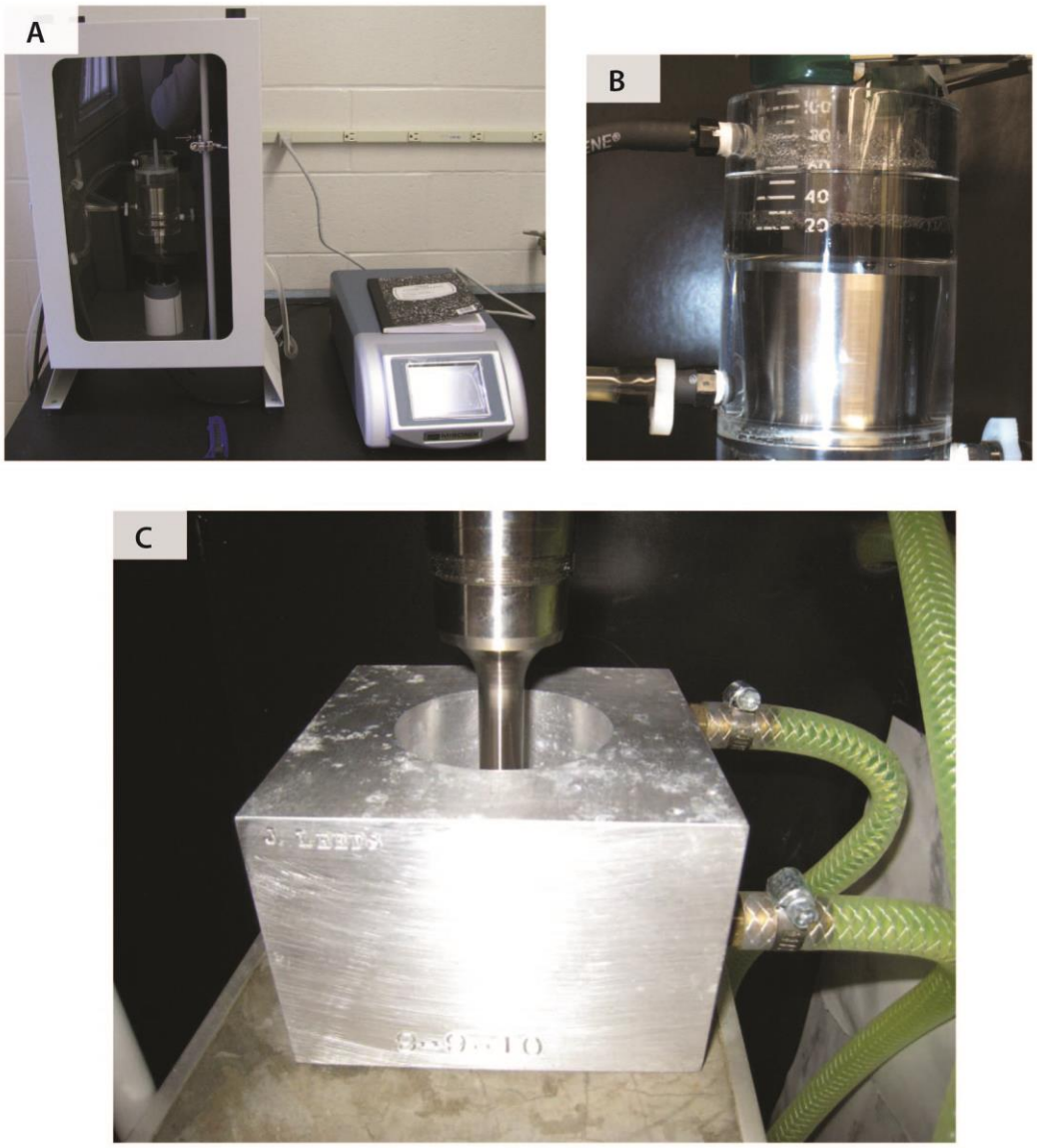

Figure 2.6. The Misonix Sonicator 4000 Ultrasonicator (A) showing the controller and soundproof enclosure with the cup-horn setup. The cup-horn setup (B) is rarely used due to the inefficient indirect coupling and problems with reproducible placement of the sample beaker in the cup. The probe tip setup (C) along with aluminum cooling jacket allows for precise placement of the sample and a consistent temperature during sonication.

transfer and mechanical wear resistance than glass. An ice bath was determined not to produce consistent results. A ThermoFisher refrigerated cooling system was used to provide chilled water to the jacket. A one-to-one mixture of ethylene-glycol to water gave an expanded operating temperature range of -30 – 105 °C. The lower coolant temperature (<5 °C) can provide quicker heat removal from the system. A heat-transfer solvent of either water or ethanol was used between the jacket and the stainless steel beaker.

2.3 – Methods and Materials

SDS (Sigma) and SDBS (TCI) were dissolved in nanopure water (18.2 MΩ). In experiments using the refrigeration system and cooling jacket, the system was allowed to equilibrate for 30 minutes prior to processing. A HiPco SWNT/ethanol slurry (Unidym) was used as the raw nanotube stock. Stainless steel beakers (Polar Ware) were used as sample containers during sonication.

After SWNTs were processed with the sonicator, ultracentrifugation was used to remove contaminants, leaving the individually dispersed SWNTs in solution. The samples were centrifuged at 122,000 g for 4 hrs in a preparative ultracentrifuge (Beckman Coulter Optima LE-80k) with a 70-Ti rotor and 26.3 mL polycarbonate Oakridge bottles filled to 100% volume. After ultracentrifugation, the rotor was decelerated under slow braking power. The centrifuge bottles were fractionated, removing the top 70% as the individually-dispersed sample. After fractionation, samples were tested for individual dispersion with absorption spectroscopy and NIR fluorescence spectroscopy (see Chapter 3 for sample spectra).

2.4 – Results and Discussion

The cup-horn was found to give inconsistent results and an unsatisfactory yield of individually-dispersed SWNTs. The sample container was hard to place in the cup reproducibly. The coolant level was difficult to control and problems occurred with coolant overflowing due to the small coolant outlet diameter. Most sample processing runs resulted in little to no individually-dispersed nanotubes.

The probe-tip setup yielded a higher concentration of individually dispersed SWNTs than the cup-horn setup. However, the original probe-tip setup was cooled with an ice bath, so automated runs were not possible due to rapid ice consumption. Temperature instability also led to results that were not reproducible. The aluminum cooling jacket successfully addressed these issues.

With this system, SWNTs can be reproducibly dispersed in an aqueous 2% SDBS solution with ultrasonication followed by ultracentrifugation. The sample is first sonicated at 3% amplitude for 30 minutes and then 25% amplitude for 1 hour. Both programs use a 10-second pulse and a 2-second dead time. The cooling jacket is set to 7 °C for the duration of the run. After ultrasonication is complete, the samples are ultracentrifuged to remove contaminants.

The mass conversion reveals how much raw material is dispersed as individual nanotubes. The linearity of the mass conversion was studied to see how effectively the individually dispersed SWNT concentration could be changed by adjusting the initial raw material concentration. This mass conversion, or product yield, is expected to be linear up to the point at which tube-tube interactions become too great for the surfactant to stabilize

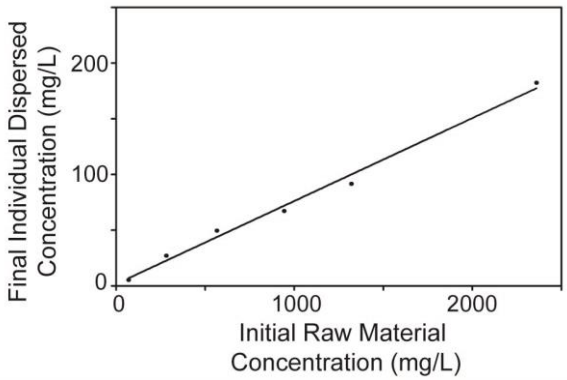

Figure 2.7. The mass conversion of SWNTs from raw material to individually dispersed nanotubes. The slope of the line is equal to the yield of the process. The process is linear up to a starting raw material concentration of at least 2450 mg/L and gives a constant, linear yield of 7.44%.

the dispersed SWNTs adequately. Mass conversion has rarely been studied at high concentrations, so little was known about how the tubes would interact with each other and the surfactant. We found that our mass conversion remained linear at 7.44% efficiency surpassing concentrations well past our anticipation (Figure 2.7). In fact, we did not discover the end of the range of linear behavior.

Our process has nearly twice the efficiency of previously reported methods that use SDS and SDBS. Moore *et al.* used ultrasonication to disperse SWNTs with a number of different surfactants.[5] They found that SDS and SDBS have mass percent conversions of 3.3% and 3.9%, respectively, when starting with a raw material concentration of 300 mg/L.[5] In addition, they reported that the mass percent conversion for SDS remains linear up to an initial raw material concentration of 500 mg/L, after which it begins to fall off. We believe that the greater temperature control available in our system allows for such an increase to the mass conversion. However, additional experiments need to be performed to verify this hypothesis.

2.5 - Conclusion

Sonication can be used to individually disperse SWNTs in surfactant solution. However, only low concentrations of SWNTs were achievable due to a small dispersing efficiency and non-linear mass conversion which decreased for high raw material loading concentrations. We showed that the achievable concentration can be increased by two means. Increasing the temperature control capability of the sonication system gives a stable low temperature during sonication. When this temperature control is combined with a superior surfactant such as SDBS, the efficiency of the dispersing SWNTs nearly doubles. In addition, the mass conversion remains linear to concentrations as high as 2450 mg/L, allowing highly-concentrated solutions of SWNTs to be prepared.

Chapter 3: Sweet nanotube inks

In Chapter 2, the efficiency of individually dispersing SWNTs was increased by adding temperature control to the ultrasonication process and switching to a better surfactant. As discussed, ultrasonication produces cavitation which releases large amounts of energy capable of breaking the large van der Waals forces holding the SWNTs in bundles; however, it takes a discrete amount of time for surfactant molecules to surround and encapsulate the nanotube. In Chapter 3, the solvent viscosity is increased to extend the amount of time for surfactant molecules to stabilize the nanotube against rebundling. It was found that individually dispersed SWNT solutions made with these modifiers have inkjettable parameters allowing them to be used in a consumer inkjet printer as an ink. In addition, when films of these SWNT inks are dried they retain their fluorescent properties. Chapter 3 is adapted from a manuscript published in *Small* titled Achieving Ultrahigh Concentrations of Fluorescent Single-Walled Carbon Nanotubes Using Small-Molecule viscosity modifiers.

3.1 - Introduction

Single-walled carbon nanotubes (SWNTs) have remarkable electrical and optical properties, particularly when they are individually dispersed.[3] However, high concentrations of individually dispersed nanotubes have been difficult to attain, which has hampered the adoption of solution-based technologies such as self-assembly,[32,45] thin-film

coating,[46,47] fiber spinning,[48] and printing.[49–52] In addition to individually dispersed solutions, recent work in thin-film transistor devices has underscored the need for producing bulk quantities of nanotubes that can remain individually dispersed after drying and/or curing.[31]

One of the interesting properties of SWNTs is the optical absorption and emission features that are associated with the electronic transitions between van Hove singularities (kinks) in the density of states.[12] These optical properties make it possible to take advantage of the unique near-infrared (NIR) fluorescence of SWNTs as a spectral signature in applications such as document security.[53] Tuning of the band-gap fluorescence by the surrounding environment[54] or through chemical doping methods[55] also enables nanotube applications such as bio-optical sensors. However, these sharp optical absorption features appear only when the nanotubes are well dispersed. Due to coupling of electronic states, fluorescence is often completely quenched when nanotubes are bundled, especially when metallic nanotubes are present.[4]

There is great interest in the individual suspension of SWNTs in solution in order to take full advantage of the optical properties of these materials.[4,12,53–55] However, the dispersion degree and solution concentration can depend greatly on the dispersing agent(s) and methods used. A wide variety of surfactants (e.g., sodium dodecyl sulfate and sodium dodecylbenzene sulfonate) have been used to suspend SWNT materials in water with concentrations of individually dispersed nanotubes typically on the order of 10-100 mg/L.[5] Although higher concentrations have been reported with surfactant dispersion, the samples are often substantially contaminated by bundles,[30] compromising the SWNT optical properties. Dispersions at moderate concentrations have been produced by wrapping

SWNTs with polymers[25,26] and DNA.[24] However, it is difficult to remove these types of polymers cleanly, and DNA is prohibitively expensive for high-volume applications. Molecules such as chitosan and neutral-pH chitosan derivatives have excellent biocompatibility but can only disperse nanotubes at low concentrations.[27] Superacids such as chlorosulfonic acid make it possible to disperse nanotubes at concentrations as high as 5000 mg/L, but the protonated nanotubes have severely altered properties and neutralizing the acid causes the nanotubes to re-bundle.[32] An inexpensive, scalable and consistent technique that gives highly concentrated, individually dispersed nanotubes in aqueous solutions is essential for applications such as nanoelectronics[56,57] and biosensors[54] that require the unique electrical and optical properties of SWNTs.

Here we report a simple method for dispersing SWNTs in water at ultra-high concentrations while preserving their unique optical properties. Our approach is based on surfactant encapsulation with sodium dodecylbenzene sulfonate (SDBS).[4,5] However, we demonstrate that by adding sucrose as a co-dispersant to lock the nanotubes in a viscous matrix, SWNTs can be dispersed to a concentration as high as 3350 mg/L while largely retaining the optical properties characteristic of individually dispersed SWNTs.

3.2 – Results and discussion

High-pressure-carbon-monoxide-synthesized (HiPco) SWNTs were dispersed in a solution containing 2% SDBS and 24.7% sucrose by ultrasonic processing followed by ultracentrifugation. These solutions were analyzed for retention of optical properties (% individually dispersed) and dispersion yield (the ratio of the post-processed, individually

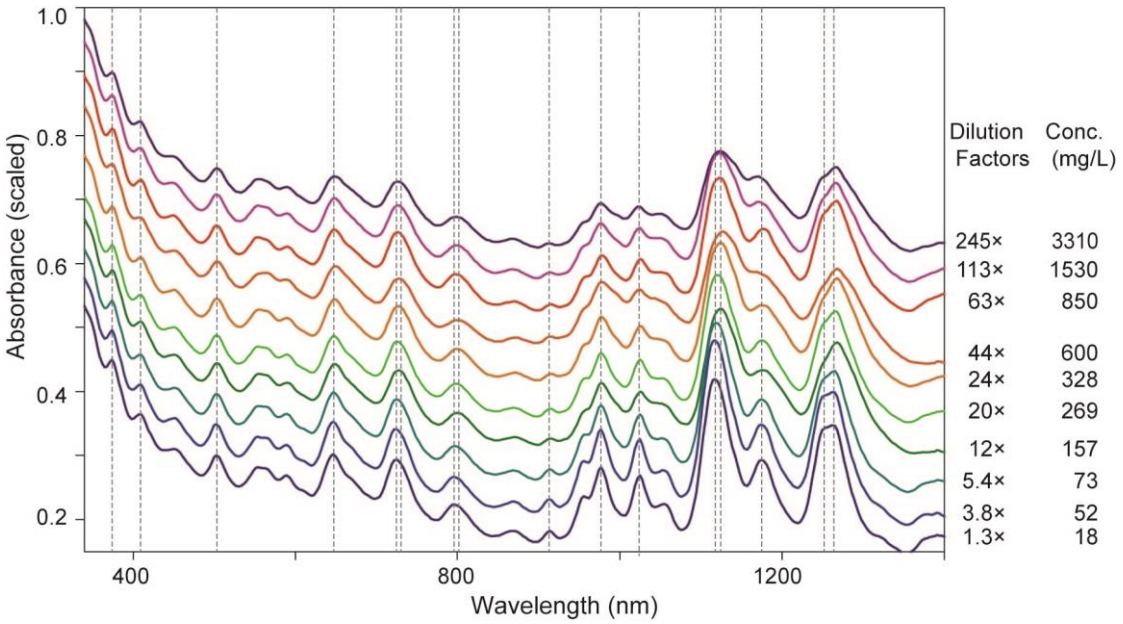

Figure 3.1. Visible-NIR absorption spectra of SWNTs individually dispersed in SDBS-sucrose solutions. Solutions were diluted to 0.5× the control concentration for comparison (spectra are offset for clarity). Sharp optical features in the visible and NIR regions indicate that SWNTs are individually dispersed in each solution, even at high concentrations. Vertical dashed lines are guides to the eye for comparing peak position and asymmetry (see Figure S1).

dispersed concentration to the pre-processed concentration) using absorption and fluorescence spectroscopies.

To confirm the presence of individually dispersed nanotubes, we used comparative spectroscopic studies of the SWNT/SDBS-sucrose dispersions against a low-concentration SWNT/SDBS control that was prepared using the conventional method.[4,5] A series of the SWNT/SDBS-sucrose samples with increasing nanotube concentrations was prepared. The samples were then diluted with SDBS-sucrose solutions to an optical density of 0.5× that of the SWNT/SDBS control. This dilution was necessary for linear absorption and photoluminescence studies. As the undiluted nanotube concentration was increased by over two orders of magnitude, from 19 mg/L to 3350 mg/L, the diluted samples continued to show the sharp optical absorption peaks in the visible (E_{22} transitions) and the NIR (E_{11} transitions) that are characteristic of individually dispersed SWNTs (Figure 3.1 and Figure

3.2). However, these features diminish in intensity and are spectrally broadened at the highest concentrations, indicating the need to monitor for the presence and quantity of nanotube bundles.

A variety of methods have been used to measure the dispersion of SWNTs in solution. Islam *et al.* employed atomic force microscopy (AFM) to measure the diameters of nanotube features and estimated their highly concentrated solutions contained around 63% individual tubes.[30] Although AFM has accurate height resolution, its poor lateral resolution poses challenges in distinguishing between individually dispersed nanotubes and small bundles. Converting from feature count to nanotube mass adds further complications to the determination of a mass-based concentration using AFM. Other reports using more accurate processing and measurement techniques[5,41] have been unable to match these high estimates of concentration and yield. Alternatively, fluorescence spectroscopy is highly sensitive to the electronic state of nanotubes and so can give direct insight into their aggregation, or dispersion state.[4] Emission intensity decreases and peaks broaden with increasing SWNT bundling. For the SWNT/SDBS-sucrose samples, excitation-emission maps show consistent peak positions and similar peak shapes for both the diluted SWNT/SDBS-sucrose dispersions and the control sample (Figure 3.3). At the highest concentration (245× dilution), the fluorescence intensity drops to about 35% of that of the control, indicating the presence of at least this percentage of individual nanotubes. To corroborate this high degree of dispersion, the number of individual nanotubes remaining in solution at these high concentrations was estimated by diluting individually

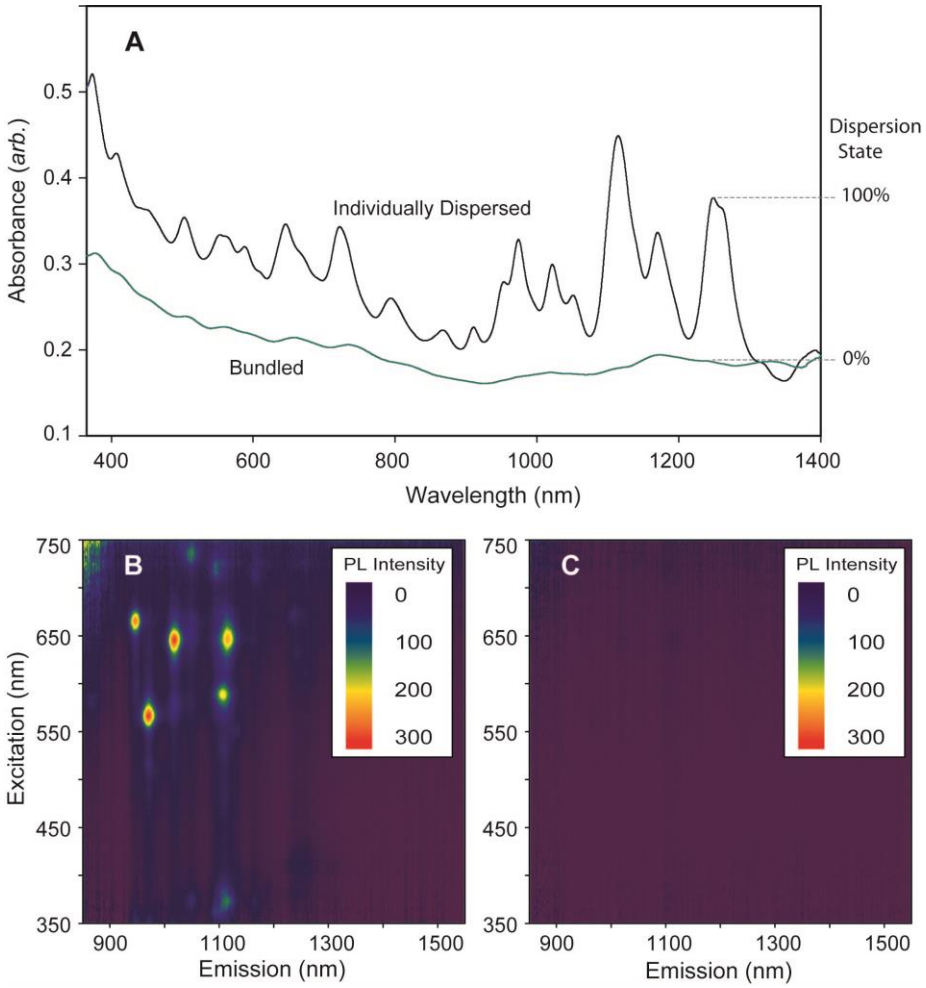

Figure 3.2. The absorption spectrum (A) of individually dispersed SWNTs contrasts that of bundled nanotubes. The sharp peaks arising from excitonic transitions between van Hove singularities are mostly absent in the bundled spectra. The Photoluminescence excitation-emission map of individually dispersed (B) nanotubes has sharp emission peaks arising from individual semiconducting nanotubes. When nanotubes bundle, fluorescence is almost non-existent (C).

dispersed nanotube solutions with bundled solutions. Comparison of the absorption spectra of these mixed solutions (Figure 3.4) with those in Figure 3.1 indicates that the highly concentrated SWNT/SDBS-sucrose solutions contain at least 25% individual nanotubes by mass, supporting the estimates from our fluorescence data.

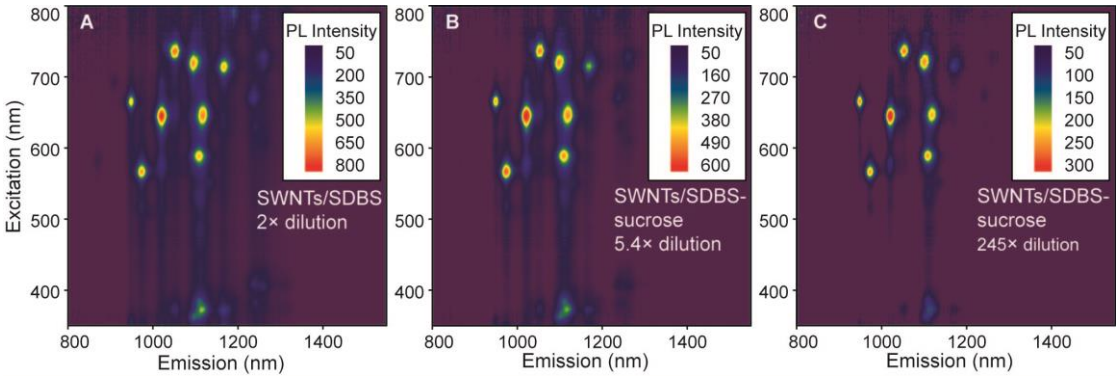

Figure 3.3. Fluorescence excitation-emission maps of SWNTs in aqueous solutions containing (A) SDBS and (B, C) SDBS and sucrose, normalized to have the same concentration by diluting (A) 2×, (B) 5.4× and (C) 245× relative to their final concentration. Even at the high concentrations, SWNT/SDBS-sucrose samples show fluorescence that is characteristic of individually dispersed SWNTs.

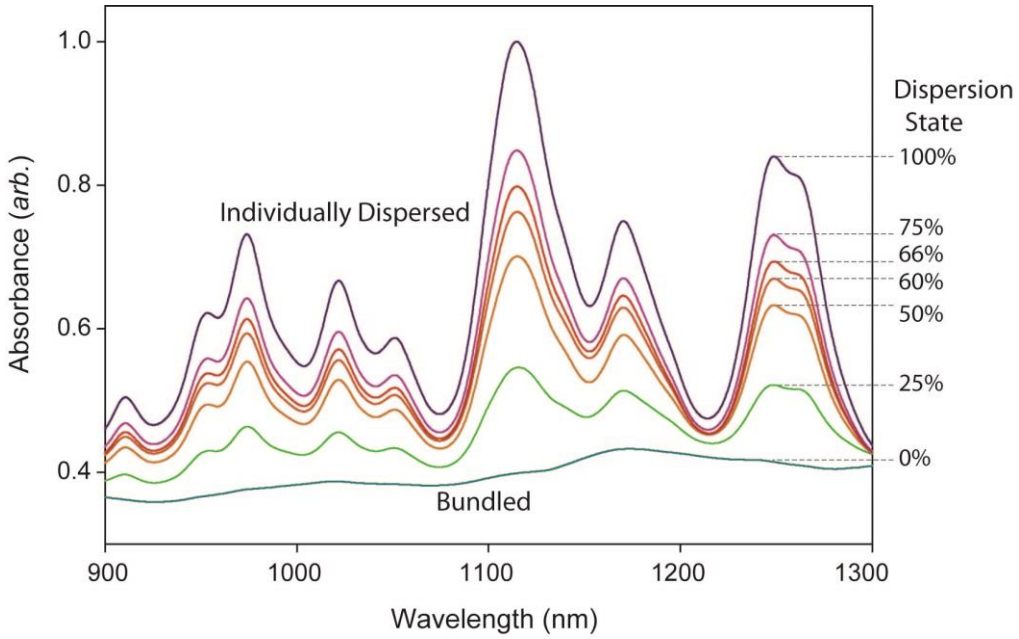

Figure 3.4. The absorption spectra of different dispersion states of carbon nanotubes made by diluting a solution of individually dispersed nanotubes with a solution containing only bundled nanotubes. As the dispersion state percentage, or number of individual nanotubes in solution decreases, peak intensities drop and broaden.

To determine the cause of the increase in nanotube concentration when sucrose is added during processing, the interaction of sucrose with nanotubes was considered. Previous research has demonstrated the ability of glucose[58] and glycerol[59] to increase the aqueous solubility of DNA and lecithin, respectively, by modifying the hydration layer of

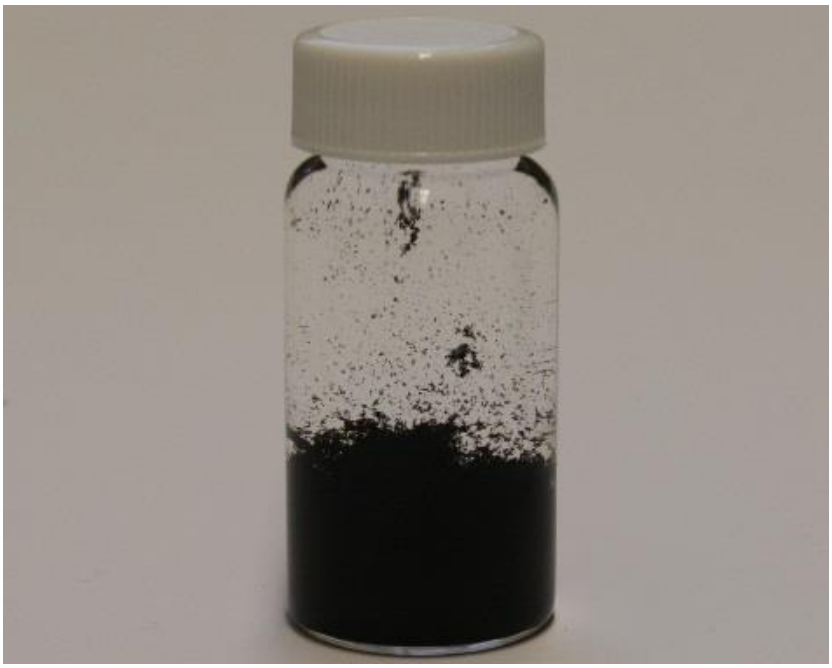

Figure 3.5. SWNT solution post-sonication. Without a surfactant, sucrose solution failed to disperse SWNTs during sonication.

the solvent surrounding the solute. However, in the absence of SDBS, sucrose fails to disperse nanotubes in water. When only sucrose is used, the solution is clear after sonication and solid chunks of undispersed nanotube material remain at the bottom of the beaker (Figure 3.5). Spectroscopic evidence also suggests that sucrose is unable to interact with nanotubes to an extent great enough for dispersion. In the SDBS-encapsulated control, both the dielectric screening by the SDBS and the π-π interactions between SWNTs and SDBS decrease the exciton energy gap.[60] Thus, the nanotube absorption and fluorescence peak positions are sensitive to changes in the interactions with surrounding molecules. Sucrose does not contain π-bonds, and so cannot have π-π interactions with carbon nanotubes. Comparison of the absorption spectra of the SWNT/SDBS control with a SWNT/SDBS-sucrose sample shows an absence of peak shifts, verifying that sucrose is unable to replace the encapsulating SDBS molecules (Figure 3.6). Slight differences in the

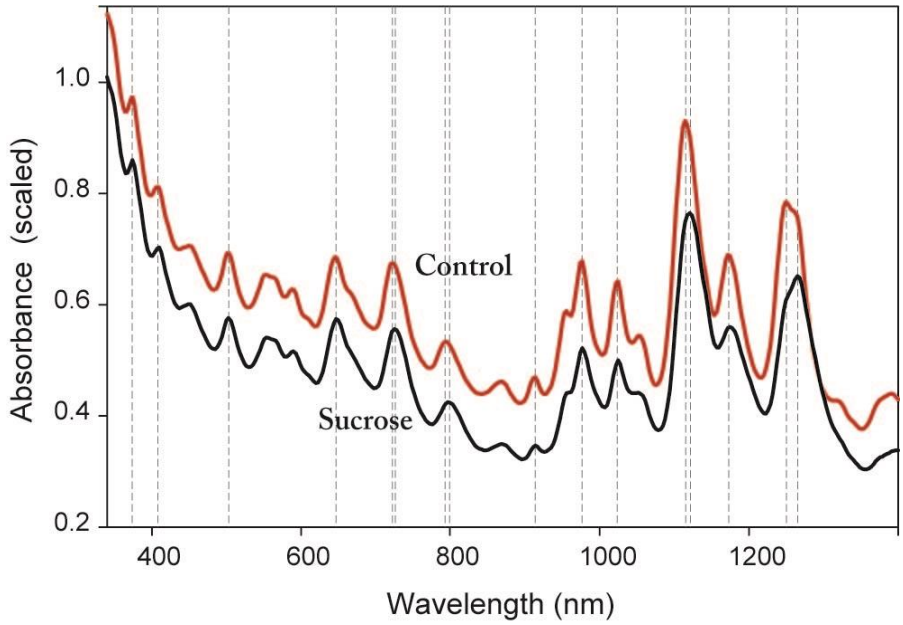

Figure 3.6 Comparison of the visible-NIR absorption spectra of the SWNT/SDBS-sucrose sample and the control normalized to the same concentration. The absence of blue-shifting in the peaks in the SWNT/SDBS-sucrose sample is evidence that sucrose is a co-dispersant. The similarities in intensity and peak width show that the sucrose sample is dispersed to a similar degree as the control sample. The spectra are offset for clarity.

peak structures can be seen, but these differences can be attributed to statistical variances in the distribution of nanotube chiralities for each sample preparation (Figure 3.7). Excitation-emission maps of the samples do not show peak shifts upon the addition of sucrose (Figure 3.3). Due to the absence of blue shifts in the spectra when sucrose is present, we can conclude that sucrose does not displace SDBS from the nanotube surface. These observations indicate that sucrose is a co-dispersant as opposed to a co-surfactant.

To provide further insight into the role of sucrose as the co-dispersant, we have tested other potential non-surfactant co-dispersants, including trehalose and glycerol. These species were chosen to mimic the viscosity (glycerol) and molar concentration (trehalose) of the sucrose solution. Our experiments revealed that these substances disperse

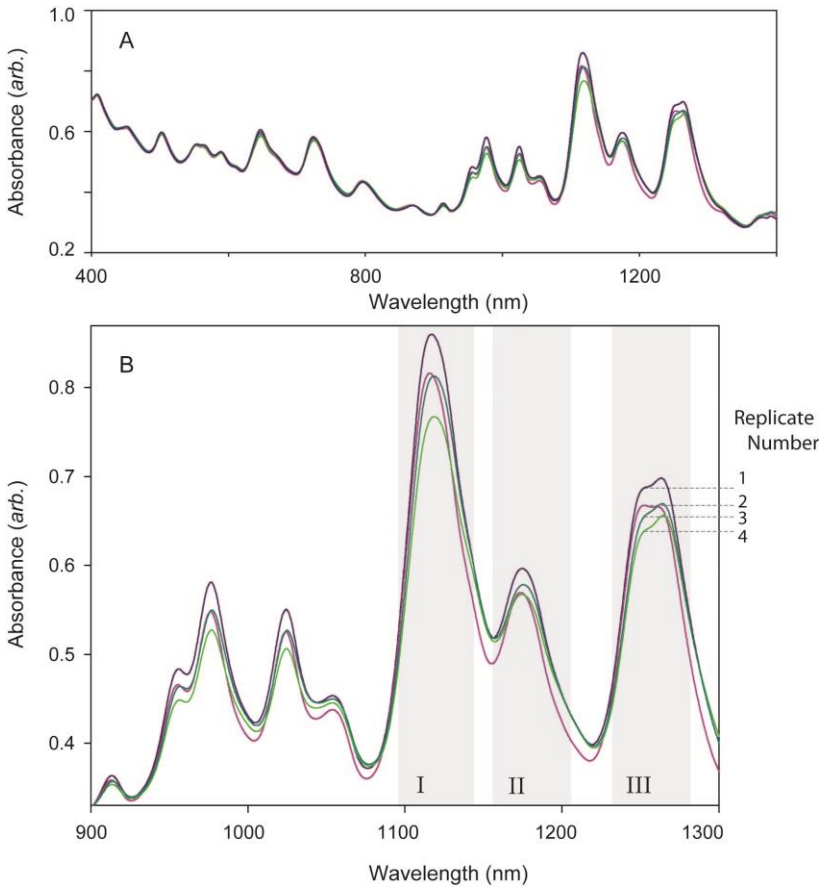

Figure 3.7. Absorption spectra of 4 replicate SWNT/SDBS-sucrose samples prepared on different days with the same batch of HiPco nanotubes. Slight variations in the final concentration have been accounted for by varying the dilution factor. Only a small variance in the absorption of the four replicates can be seen in the visible region of the spectra (A) which consists mainly of E_{22} transition. However, there exists a large statistical variance in the NIR region (B), where the peaks correspond mainly to E_{11} transitions. Evaluating the fluorescence excitation-emission maps for these solutions, the number of species in each of shaded regions I, II, and III can be shown to be 3, 2 and 4, respectively, causing the peaks to be highly asymmetric. In region III, replicates 1, 3 and 4 appear to be red shifted from replicate 2, an illusion that is created due to the distribution of nanotubes being skewed toward species with lower-energy E_{22} transitions. This same phenomenon is evident in regions I and II to a lesser degree.

nanotubes to a similarly high concentration as sucrose. While trehalose is a disaccharide with a size and structure that is similar to that of sucrose, glycerol is a much smaller molecule (Figure 3.8). These experiments provide insight into the role of viscosity enhancers in stabilizing nanotubes during ultrasonic processing for efficient surfactant encapsulation.

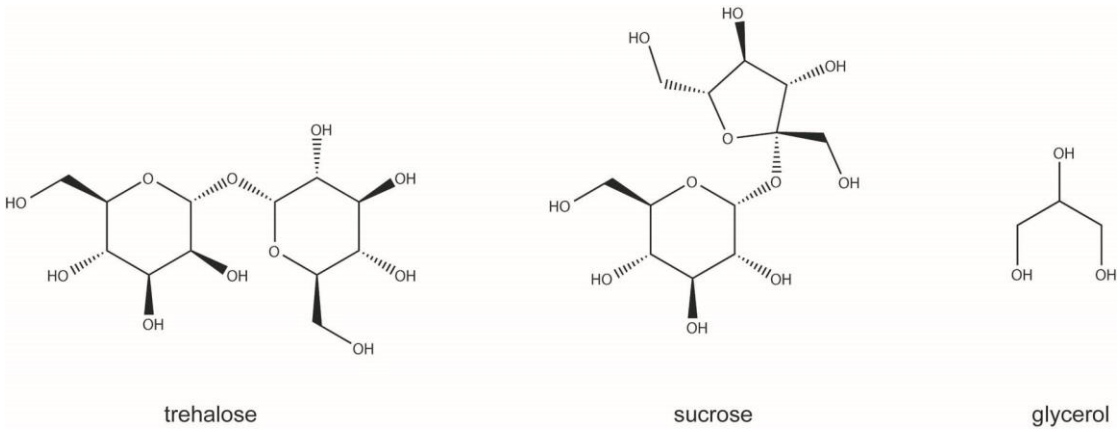

Figure 3.8. Molecular structures of viscosity enhancing agents used in the experiments.

Previous reports of the nanotube dispersion yield using SDBS have varied from 3.9%[5] to higher than 50%.[30,41,61] The differences in these reported values are due in part to differences in experimental techniques, which leave nanotubes in different states of dispersion (bundles vs. individual) at various concentrations. Individually dispersed nanotubes with higher yields have been reported, but these high yields are attainable only at low nanotube concentrations.[41] The introduction of sucrose with SDBS significantly increases this dispersion yield. We found that sucrose increases the yield to 24%, which is more than a factor of 6 higher than a previous report that used a technique similar as what was used to prepare our control.[5] Our yield remained constant even when the initial nanotube load reached a concentration of 13,800 mg/L (Figure 3.9), after which point it became difficult to mix the large amount of nanotubes with the small volume of solvent. This constant yield allows solutions of individually dispersed SWNTs in the g/L range to be prepared simply by increasing the initial amount of raw material. The highest nanotube concentration achieved has an optical density 124 times higher than those prepared following a conventional method.[4,5] Figure 3.10 shows a photograph of the solutions sealed in capillary tubes with a 400 μm inner diameter. Even with this small optical path

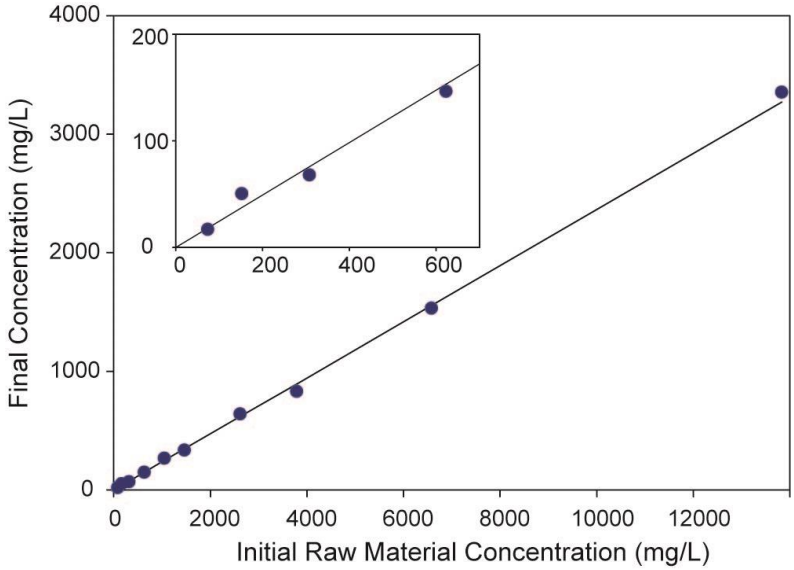

Figure 3.9. The yield of individually dispersed SWNTs in an SDBS-sucrose solution as a function of initial nanotube load. The high yield (24%) persists linearly over a range of more than three orders of magnitude in concentration, allowing individually dispersed SWNT solutions to be prepared in the g/L range by increasing the initial nanotube load. The inset expands on the lower concentration region to show detail.

length, the most concentrated solutions (1530 and 3350 mg/L) are indistinguishable from one another due to their high optical densities.

Nanotube concentration is typically estimated based on optical absorbance, which is influenced substantially by both composition and aggregation state.[62] The ultrahigh concentrations of our nanotube dispersions enabled us instead to use gravimetric calibration to determine the nanotube concentration. The SWNT/SDBS-sucrose solutions with the highest concentrations were coagulated and filtered to remove the surfactant and sucrose. The collected pure nanotubes were then weighed to determine both the yield and the final mass concentration after processing. The highest concentration of dispersed SWNTs achieved was 3350 mg/L.

Due to the high retention of the electronic and optical properties of nanotubes, aqueous solutions of individually dispersed SWNTs may have broad implications as inks in applications such as document security,[53] anti-counterfeiting measures,[53] and nanotube

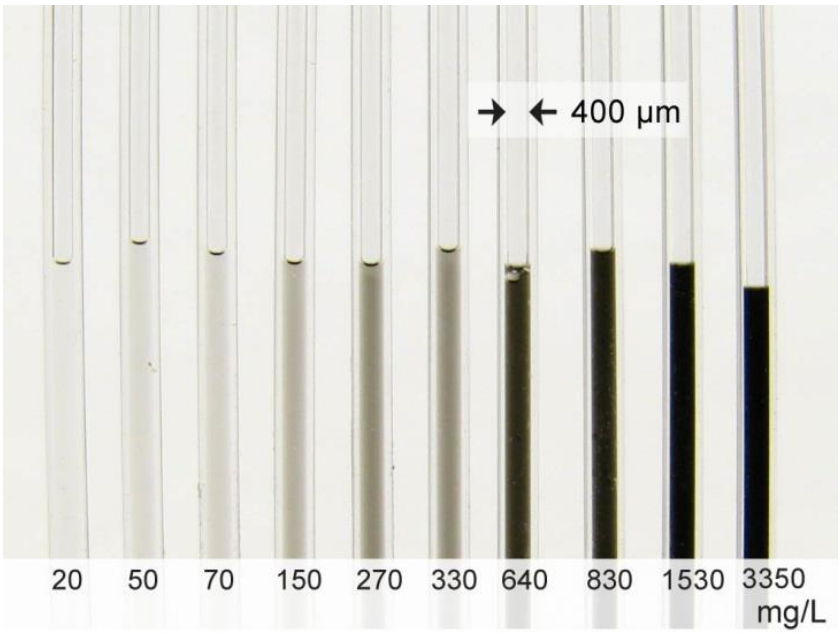

Figure 3.10. Capillary tubes containing different concentrations of SWNTs in an aqueous solvent with both SDBS and sucrose. The samples with the two highest concentrations are visually indistinguishable from one another due to their high absorbance.

electronics.[56] We tested the viability of our solutions as SWNT-based inks for printing on paper and polymer substrates. The 3350 mg/L concentration SWNT/SDBS-sucrose solution was used in a technical pen to draw lines with widths of 300 µm as defined by the pen on a variety of substrates. The SWNT/SDBS-sucrose samples had a similar viscosity to the technical pen ink and could be used in the pen unaltered. The high optical density of the nanotube ink gave a large enough contrast ratio on the silicon and paper products that the drawn lines could be seen readily (Figure 3.11).

Another advantage of nanotube inks is their compatibility with bottom-up processing using techniques such as inkjet printing.[63] Previous aqueous dispersions of polymer wrapped or functionalized nanotubes have been inkjet-printable but lacked the optical properties of pristine nanotubes due to bundling or sidewall covalent modifications.[64] Nanotubes suspended in organic solvents can also be printed using specialized inkjet systems.[65] However, these solvents are incompatible with the plastic

Figure 3.11. SWNT/SDBS-sucrose solutions were used as an ink in a 300 μm technical pen. Several substrates were written on using the SWNT/SDBS-sucrose ink including paper products, silicon and glass.

components used in typical consumer-grade inkjet printers. To our knowledge, there have been no reports of inkjet printing patterns of fluorescent nanotube inks with any solvent.

Solutions containing concentrations of nanotubes from 0 mg/L to 800 mg/L were used directly as inks in a consumer-grade inkjet printer (Canon PIXMA MG6120). At nanotube concentrations above 800 mg/L, the viscosity of the solution is too high to allow for consistent, uninterrupted printing in this style of inkjet printer. The character formation from the inkjet drops is consistent across the stock ink, the SWNT/SDBS-sucrose ink and the SWNT/SDBS ink (**Figure *3.12***). However, the contrast ratio (blackness) of the SWNT/SDBS-sucrose ink is much higher than that of the SWNT/SDBS control. Placement of the SWNTs can be verified with Raman mapping of the printed characters using the G-band of the SWNTs (Figure 3.13C). Only the SWNT/SDBS-sucrose sample showed intense nanotube spectral features with fluorescence spectroscopy of the bulk printed area (Figure 3.13B). At lower excitation/emission wavelengths broadband

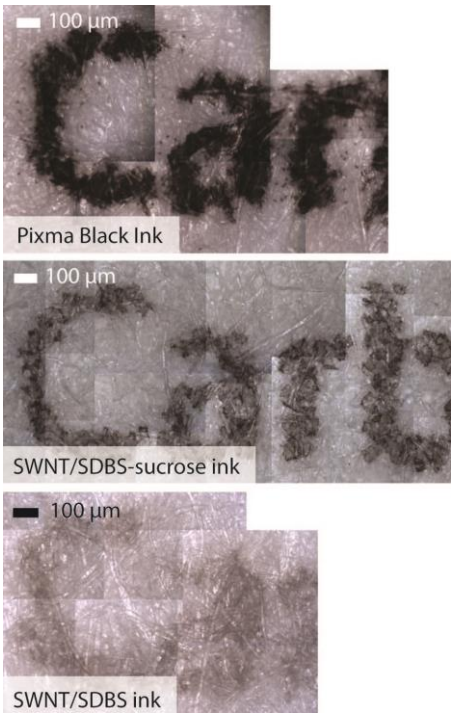

Figure 3.12. Composite optical micrographs of the word 'Carbon' inkjet-printed on paper using Canon PIXMA black ink (stock), SWNT/SDBS-sucrose ink and SWNT/SDBS ink (control). The SWNT-based ink jetted with a uniform coating on the substrate, comparable to the PIXMA black ink.

fluorescence from the paper substrate saturates the fluorescence map. However, the characteristic NIR fluorescence peaks for the dominant SWNT species are clearly distinguishable in the unobstructed region of the map. This offset in nanotube fluorescence places the signal in a region unhampered by background and environmental signals, making nanotube ink ideal for applications such as document security.

Our sucrose-based nanotube inks can also be used for making thin films. It has been shown that high-concentration solutions of SWNTs prepared by sonication in SDBS/polyvinylpyrrolidone without centrifugation can form thin films when coated on oxidized silicon surfaces.[47] However, these films crack and become inhomogeneous

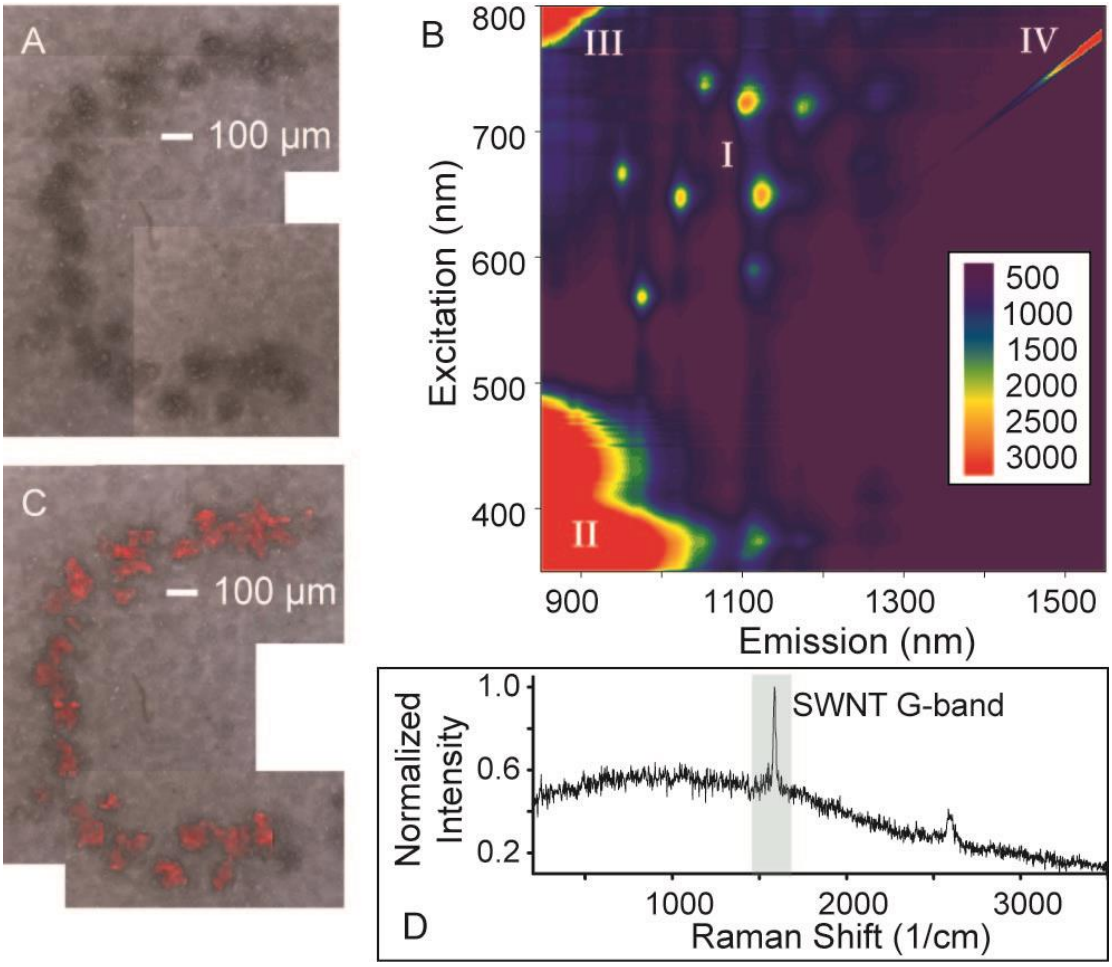

Figure 3.13. Inkjet-printed fluorescent features on paper. (A) Composite optical micrograph of the character 'C'. (B) Excitation-emission fluorescence map of a bulk area of the inkjet-printed sample showing the characteristic nanotube fluorescence. The SWNT fluorescence is in a spectral region (I) that is unimpeded by the substrate fluorescence (II), source reflection (III) and second harmonic reflection (IV). (C) Raman map of the ink-jet printed SWNT features overlaid on image (A) using the SWNT G-band shown in (D).

during solvent evaporation leaving nanotubes suspended across the fissures. Consistent with the literature result, with our control sample the nanotubes tended to coagulate into bundles when the solution was drop-cast and dried on a glass substrate (Figure 3.14). When typical nanotube solutions are dried, the high surface tension caused by capillary forces as the solvent front retracts typically leads to nanotube bundling that suppresses the characteristic optical properties of nanotubes, and especially the NIR fluorescence.

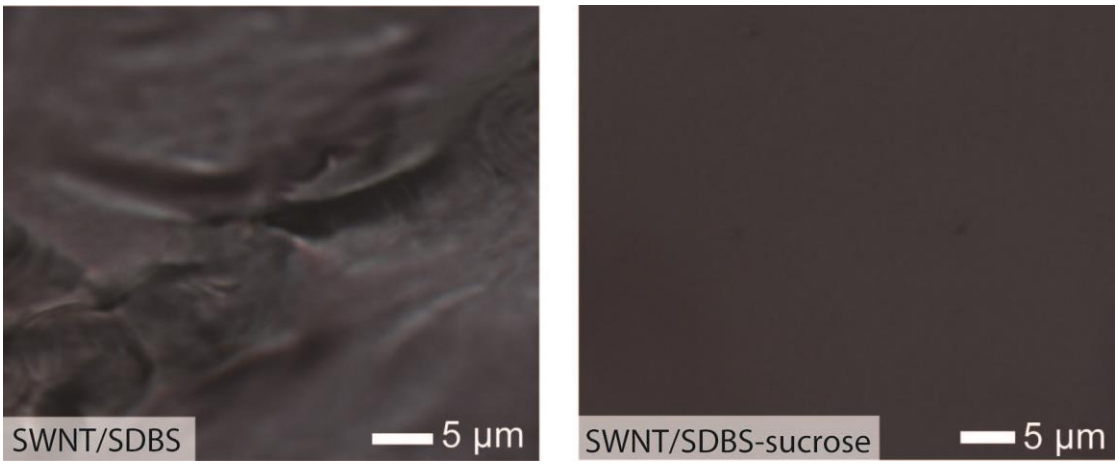

Figure 3.14. Drop cast solutions of SWNT/SDBS (left) and SWNT/SDBS-sucrose (right). Sucrose keeps the SWNTs from bundling creating a uniform film upon drying.

However, sucrose allows the nanotubes to remain individually dispersed upon drying, even at high concentration. Thus, due to the increased viscosity of the SWNT/SDBS-sucrose sample, the ink dries into a uniform film (Figure 3.14). This feature of the ink not only enables efficient drop casting but also allows for thin films to be created using a modified Mayer Rod coating technique.[66] After casting a thin film using the SWNT/SDBS-sucrose solution, the sucrose matrix and surfactant can be subsequently removed by washing with ethanol and water. Within the sucrose matrix, the SWNTs remain individually dispersed even after the thin film dries which is evident by the retention of fluorescent features. When the thin film is washed with ethanol and water the sucrose and surfactant are removed and the nanotubes quickly bundle, which quenches the nanotube fluorescence (Figure 3.15).

3.3 – Conclusion

The addition of viscosity enhancers such as sucrose to aqueous dispersions of SWNTs with SDBS makes it possible to achieve individually dispersed nanotube

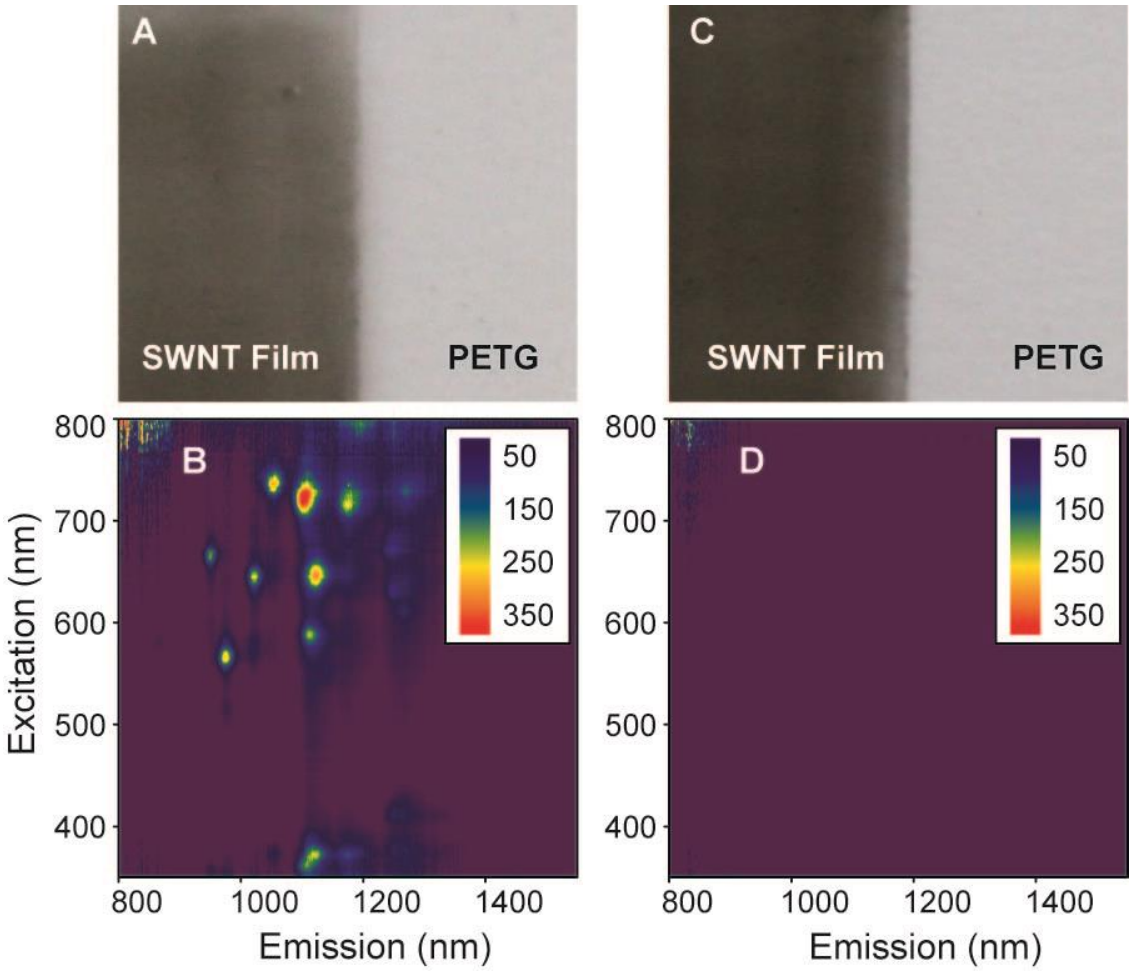

Figure 3.15. Carbon nanotube film produced with a modified Mayer Rod coating technique (A) before washing shows fluorescence of nanotube species (B) indicating that tubes are individually dispersed to a high degree. After washing away the sucrose matrix with an ethanol-water mixture (C) the nanotubes bundle eliminating the sharp fluorescence peaks (D).

concentrations in the g/L range while retaining the nanotube optical properties. Similar effects were observed with other small-molecule viscosity enhancers such as trehalose and glycerol, suggesting the role of solution viscosity in stabilizing aqueous dispersions of carbon nanotubes during processing to provide ultrahigh nanotube concentrations. Due to the retention of optical properties, the nanotube dispersions can be used as fluorescent inks in consumer-grade inkjet printers, technical pens, and other printing techniques such as Mayer Rod coating. The printed structures show strong, well-resolved fluorescence peaks that are characteristic of individually dispersed SWNTs.

3.4 – Methods and materials

3.4.1 – Solvent preparation

Sucrose in water was used to prepare a solution that was isopycnic with D_2O. Sucrose (ACS grade, Mallinkrodt Chemicals) was added to Nanopure™ water (18.2 MΩ) and adjusted to 24.7% w/w using the solution's index of refraction as a reference. SDBS (TCI) was then added at 2% w/v to the solution and dissolved. Control solutions were 2% w/v SDBS in Nanopure water.

3.4.2 – Dispersion

Raw HiPco SWNTs (Unidym Lot #R0513) were added to a stainless steel beaker along with 26 g of solvent (hereafter SWNT solutions containing SDBS-sucrose are referred to as SWNTs/SDBS-sucrose samples). Samples without sucrose were used as controls. The SWNT materials are received as a slurry in ethanol containing 12.3 wt% solid material with approximately 35 wt% metal catalyst/ash impurities. The nanotube mass was adjusted to account for only the solid material and reported as *initial nanotube load*. The beaker was cooled in a custom refrigerated jacket to 7 °C and subsequently sonicated with a probe tip sonicator (Mysonix 4000: 12.7 mm diameter tip) immersed in the sample. Two stages of sonication were used: 3% amplitude for 30 min followed by 25% amplitude for one hr. This first, low-power stage of sonication can replace the traditional high-shear mixing used by others.[4,25] A pulsed energy profile (10 s pulses with 2 s dead time) was incorporated for both stages to avoid heating. After sonication, the dispersions were

centrifuged at 122 kg for 4 hrs (Beckman Coulter Optima LE-80k) to remove bundled nanotubes and metal particle impurities.[4] The centrifuged tube was separated into 2 fractions: Fraction 1 (top 2 mL) and Fraction 2 (middle 12 mL). Fraction 2 was used for the primary analysis.

3.4.3 - Characterization

Solutions were characterized for individual dispersion and concentration using optical absorption, photoluminescence, and Raman spectroscopies. UV-Vis-NIR spectra were collected in the range of 350-1400 nm using a Perkin Elmer Lambda 1050 equipped with a InGaAs detector. All spectra were normalized by diluting with the respective solvent to an absorbance of 0.592 at 500 nm, so that each solution's concentration was in the linear absorption range.

Fluorescence excitation-emission maps were recorded with a Horiba Jobin Yvon NanoLog fluorescence spectrometer using a liquid-N_2 cooled InGaAs array detector. Samples were excited in the range of 350-800 nm using a 450 W xenon arc discharge lamp while collecting emission spectra in the range of 800-1500 nm.

Raman spectra were collected with a Horiba Yvon LabRam ARAMIS Raman microscope. The excitation source was a He-Ne (632.8 nm) laser. The samples were drop cast onto a microscope slide and the solvent was allowed to evaporate. Optical images and the corresponding Raman scattering spectra was collected for multiple areas on each sample and compared. Additionally, Raman mapping using the G peak was performed on ink-jet printed samples.

3.4.4 – Gravimetric analysis

The high-concentration solutions were subjected to gravimetric analysis. A fraction of the centrifuged solution was coagulated by addition of ethanol and subsequently filtered with a 1.2 μm pore membrane filter (Millipore Isopore RTTP). The collected solid was washed with a 50/50 mixture of Nanopure water/ethanol and then bath sonicated to re-disperse the cake. This process was repeated 4 times, after which the solid was dispersed in 100% ethanol, filtered (Millipore Fluoropore FGLP 0.2 μm), washed and then dispersed with a minimal volume of dichloromethane. The solvent was evaporated and the remaining solid was dried overnight in a vacuum oven. The mass of this dry material was recorded and the nanotube purity was determined by thermogravimetric analysis using a TA Instruments Q500 Thermogravimetric Analyzer. Samples were heated from 35 °C to 700 °C at 10 °C/min in an inert argon atmosphere.

3.4.5 – Nanotube ink

The highest concentration SWNT/SDBS-sucrose solution (3350 mg/L) was used as an ink to write on various substrates. A technical pen (Kohinoor Rapidograph 300 μm) was used as the writing instrument to give a well-defined line width. This style of pen was chosen due to its removable ink-tank and a pen head that can be disassembled for easy cleaning of all internal components. The aqueous nanotube solution was loaded into the pen after centrifugation as prepared. Writing was performed on substrates including general-purpose laser printing paper (Boise X-9), note cards (Oxford White), Post-It® Notes (3M), adhesive labels (Avery 8160), glass microscope slides (Sailing Boat #7101),

and silicon wafers. Control prints were made on the same substrate materials using the SWNT/SDBS control sample.

3.4.6 – Inkjet printing

A consumer-grade Canon PIXMA MG6120 multifunction printer was used to inkjet-print the nanotube solutions on various paper substrates including Kodak photo paper (Matte), general purpose printing paper (Boise X9), note cards (Oxford White) and Southworth 100% cotton premium resume paper (32 lb Ivory). The original, water-soluble PIXMA ink was flushed from the cartridge with 4 L of Nanopure water followed by 50 mL of isopropyl alcohol. Drying in a vacuum chamber removed traces of the alcohol. Both SWNT/SDBS-sucrose solutions and the control were used unaltered by loading into individual ink cartridges. Purging removed traces of prior samples from the system.

SWNT/SDBS-sucrose solutions with nanotube concentrations ranging from 0 mg/L to 800 mg/L were used as ink for inkjet printing. Two test patterns were then printed on paper substrates. The first test pattern (Figure S9) consisted of text and logos of decreasing size to evaluate how the nanotube ink printed in the inkjet system. The second, a geometric pattern, (Figure S10) was used to evaluate contrast ratio and fluorescence.

3.4.7 – Sucrose removal

Highly concentrated SWNT/SDBS-sucrose solutions (~2 g/L) were coated on a polyethylene teraphthalate-cyclohexane dimethanol copolymer (PETG) with a thickness of 50 μm using a modified Mayer Rod coating technique. After drying in an oven at 75 °C for 90 sec, fluorescence of the nanotube film was measured to evaluate whether the film

contained individually dispersed nanotubes. The film was then washed with 100% ethanol followed by a gradient of ethanol and water ending with a 1/1 ethanol-water mixture.

Chapter 4: SWNT inks – contrast ratio

The large absorbance background of individually dispersed SWNTs suggests that these materials would be excellent blackbody absorbers. Furthermore, only a limited number of chiralities have fluorescent E_{11} transitions in the visible region of the electromagnetic spectrum. Thus, Sweet Nanotube Ink could be an attractive material for use as a pure black ink in applications that require high contrast ratios and/or anti-reflective properties. In consumer ink applications, the contrast ratio as perceived by humans is the key element. In this Chapter, I discuss measurement of the perceived contrast ratio of SWNT ink using a consumer-grade, digital point-and-shoot camera.

4.1 – Contrast ratio

Contrast ratio is used to measure the difference between two colors in a chromic system. For a black-and-white system, contrast ratio is determined by the luminance (amount of light reflected and/or emitted) from a black area of the medium compared to a white area of the medium.[67] Contrast can be thought of as the difference in brightness between a black element and a white element of the medium. Figure 4.1 compares two patterns with different contrast ratios; image A has a higher contrast and is easier to see than image B. In a perfect system in which the white area is purely reflective (a *perfect reflecting diffuser)* and the black area absorbs all incident light (a *blackbody absorber*), the

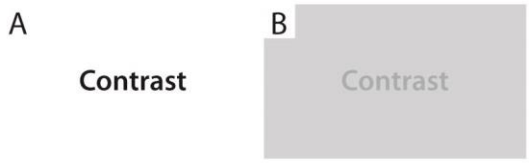

Figure 4.1. For printed text media, the contrast ratio tells the level of white to the level of black for the media and text respectively. The print in (A) has good contrast with black text on media. The off-white (light-gray) background and gray text give the print in (B) poor contrast.

contrast ratio is undefined because the luminescence intensity of the black region is zero. However, in the real world not only are the white and black areas not perfect reflectors and absorbers, but non-ideal conditions exist, such as interference from adjacent elements (Section 4.3.1).[68,69] Therefore, the luminance of any real black element is greater than zero and the contrast ratio of a real chromic system can be defined.

Contrast ratios can vary greatly depending on the medium. The contrast ratio of consumer electronics is usually much higher than that of print media. For backlit electronic displays that display static images, such as computer screens and televisions, the contrast ratio is the amount of light reflected and emitted from a black area of the screen relative to that of a white area of the screen. Due to backlighting, the luminance of a white element is significantly higher than that of a black element. Many manufacturers artificially inflate the contrast ratio by measuring black elements with the screen's backlight off (pure reflection) and comparing to white elements with the screen's backlight at 100% intensity. In this measurement scheme, contrast ratios of 100,000,000:1 or higher are possible.[70]

4.2 – Contrast ratio in color systems

In a system with ideal black and white elements, the contrast ratio could be characterized completely using only a single wavelength of light. The images we wish to

measure are not ideal, but rather contain real black and white elements that have a wavelength-dependent reflectivity. Also, the spectrum of real-world illumination sources, including the sun, fluorescent lights and LEDs, do not have equal intensity at all wavelengths. For real media viewed in non-ideal lighting scenarios, luminance values must be measured for a range of wavelengths. To determine the perceived contrast ratio, the range of wavelengths should be ones that can be seen by humans.

Due to the relatively low energy of photons in the visible region of the spectrum, the energy of a single photon cannot be directly measured using a solid-state sensor (unlike the case, for instance, of gamma ray spectrometers).[71] To measure visible photon energy, the incoming light must be separated by wavelength using either color filters or a monochromator and then integrated for a period to minimize noise. For systems using monochromators, optics divide the incoming light into separate paths (in either space or time), with each path containing an individual spectral range. Individual sensors must detect each wavelength range, or a mechanical system must be used to move the light path relative to a single sensor. The integration time required depends on the number of paths sensed divided by the number of detectors, making measurements over large spectral ranges slow. The presence of adjacent elements with a sharp difference in contrast can also affect both the measured luminance and the perceived brightness of each element. Absorption and reflection spectrometers are not capable of taking measurements when multiple elements are present. Due to the time required to scan multiple wavelengths along with the problem of adjacent elements, a different color acquisition system was pursued.

While factors such as reflected interference can be accounted for, the same is not true for some other factors. The pattern of an image is important and can cause the human vision system to misinterpret the colors viewed. Therefore, the perceived contrast ratio will not be equal to the measured contrast ratio.[68,69] Figure 4.2 shows an optical illusion in which the level of gray in regions A and B is the same. However, due to the checkerboard pattern, the human vision system misinterprets B as being lighter than A. Most detection systems do not contain image processing algorithms to account for this type of perceived error, and as a result the systems will pick up the true color instead of the human perceived color.

4.3 - Human color vision

The human vision system does not measure color by scanning individual wavelengths. Instead, a linear combination of multiple types of receptors, each with a

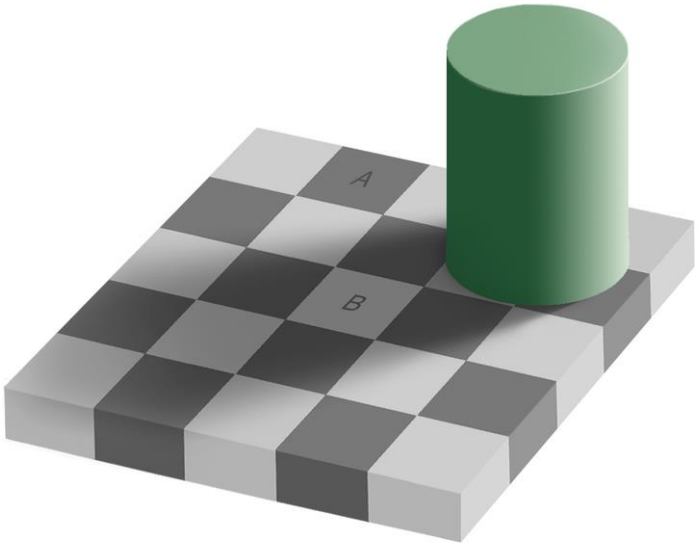

Figure 4.2. An optical illusion that uses patterns to trick the human vision-processing system. Squares A and B are the same shade of gray; however, B is perceived as being significantly lighter than A. (image courtesy of Wikimedia Commons)

non-linear response to different wavelengths, is used to measure a set of colors.[67] Using a combination of multiple receptors in this way allows for fast determination of color without measuring each wavelength individually. A problem exists, though, in that the set of colors represented in this way is only a subset of the continuous spectrum, so every color cannot be represented.[72] However, since we are interested in the perceived contrast ratio, a color set generated by mimicking the human vision system will show only wavelengths humans can perceive. A closer look at the human vision mechanism follows.

4.3.1 – Human vision and color planes

Early empirical evidence suggested that human color vision could be stimulated accurately by varying only three parameters[67] In the simplest of cases, the three parameters can be represented by three colors, so long as any one of the three cannot be represented by linear combination of the other two. The primary colors, red (R), green (G), and blue (B), are most commonly used. The mixtures of these colors in all possible proportions makes up what is known as a colorspace. A defined colorspace can have more than 16 million colors, any of which is represented by a specific proportion of the three defining colors while holding all other conditions constant.[67] The set of colors that can be represented by the primary colors is called the RGB colorspace. Parameters other than color can also be chosen, such as hue, saturation and lightness, which make up the HSL colorspace.[73] The concept of colorspace is used to define colors with only three values in disciplines such as art, image acquisition, lighting, printing and color display systems.

The evidence for color reproduction by three parameters was later strengthened by the finding that the human color vision system contains only three distinctly different color

receptors. Each type of sensor has a wavelength-dependent response function with a maximum sensitivity in a different spectral region. Even though these sensors work in real time, they do not report photon energy. Their response instead depends upon the sum of the energies of the photons detected at any moment. Many commercial colorspaces have been created with slightly different components that better represent human color vision. Work in the past several decades to measure the response function of individual types of receptors[74] has allowed for the production of more accurate representations of the intrinsic human colorspace. These modern colorspaces, such as sRGB, are used in color-reproduction systems such as cameras, televisions and graphics programs.[67]

4.4 – Digital cameras

Digital cameras take an approach similar to human vision to acquire color images, which is compatible with simple optics and short integration times. A mosaic-patterned color filter array (CFA) is placed over a sensor array (specific CFAs will be discussed more in Section 4.4.3). This filter blocks out the appropriate wavelength of light so that each pixel is illuminated with a limited range of wavelengths. This type of acquisition closely mimics human vision, in that the sensor response function is imitated by the CFA, and only three types of sensors are used.

4.4.1 – Imaging with consumer digital cameras

A consumer-level digital camera can be used to measure the reflected light from a printed medium for human-perceived measurement and comparison of contrast ratio. A charge-coupled device (CCD) sensor, as found in most consumer point-and-shoot digital

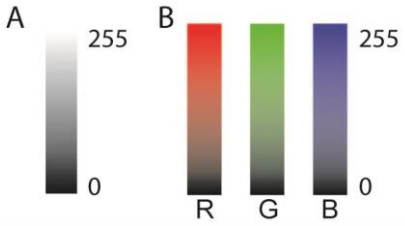

Figure 4.3. 8-bit color planes showing (A) black and (B) the red green blue, or RGB, colors. A value of 0 indicates black and 255 represents white/full color, with intermediate shades in between.

cameras, contains an array of sensors that are called pixels (from "picture elements"). The CCD measures the radiant exposure of light hitting each pixel. Although they are not real-time systems, digital cameras are a close representation of human vision.

When a picture is taken with a digital camera, the shutter opens for a specified amount of time to collect light with the CCD. During this integration time, each pixel converts sensed photons to a stored electric charge. At the end of integration, the amount of stored charge is converted with an analog-to-digital converter to an 8-bit integer having 2^8, or 256 possible values. In an 8-bit monochromatic colorspace, a value of 0 indicates black and 255 indicates white. Values in between are shades of gray that get progressively lighter as the value approaches 255 (Figure 4.3A). With all camera sensors, a value of 0 indicates an underdeveloped pixel and a value of 255 indicates an over-saturated pixel; thus, a value of 0 or 255 is not an accurate portrayal of the actual brightness. The dynamic range of a point-and-shoot CCD is generally smaller than 254 due to dark counts and leakage current.[75] For instance, the dynamic range of the camera used in these studies is only ~160.

4.4.2 – Exposure Control

To measure the level of reflected light in a system with even a moderate contrast ratio, a large detection dynamic range is required. Digital camera CCDs do not have large sensing ranges, especially insofar as the dynamic range is smaller than the 256 available bins. CCDs are integrating detectors, however, and have three methods of light metering that can be controlled manually to allow the camera to sense a large range of light intensities while remaining within the dynamic range of the sensor. Light metering is accomplished using the aperture (F-number or F-stop) which controls the amount of light getting to the sensor, the shutter speed which controls integration time, and the ISO (film speed) which that translates to detector gain in digital cameras.

4.4.3 - Color acquisition in digital cameras

As discussed in Section 4.4.1, digital cameras take advantage of color planes to measure and reproduce color images digitally. A CFA is used in effect to bin photons into three groups represented by the red, green, or blue values. The most common type of CFA used in digital cameras is the Bayer filter.[76] A traditional Bayer filter setup contains two green filters for every red and blue filter (Figure 4.4). With the demand for smaller CCDs and low light levels coupled with faster digital processors, some companies have turned to other, less lossy CFA designs.[77]

After the charge from each pixel is collected from a CCD that has a CFA in front of it, each pixel contains a single value referenced to the filter color over that specific pixel (either green, red or blue). A color image requires three pixel values, though, so the missing values must be interpolated using a process known as demosaicing. The simplest

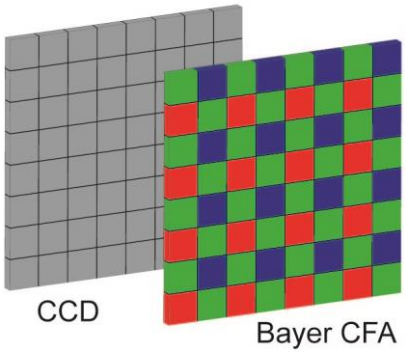

Figure 4.4. A Bayer color filter array placed over a CCD array detector used to bin photons into three different ranges of energy.

demosaicing process involves calculating the missing value from its surrounding neighbors or kernel.[67] Due to the increased sensitivity of the human eye to green light, the Bayer CFA contains more green filters than red or blue filters, and so the green plane has lower interpolation error.[76]

4.4.4 – Errors in measuring contrast ratio with a point-and-shoot camera

Consumer-grade, point-and-shoot cameras are susceptible to several types of errors in measuring the luminance intensity and calculating the contrast ratio. These errors should be considered and weighed against using a more advanced system, such as an absorbance or reflectance spectrometer.

The most significant source of error in the experiments reported here likely arises from the compression of the images that is performed automatically by the camera. Digital cameras can save images in various raw and compressed formats. In a raw image format such as TIFF, each pixel contains a full 24 bits of RGB color information. This type of image retains the most information at the cost of a large file size. For the type of calculations being performed here, a raw image format is the best to use. Unfortunately,

many point-and-shoot cameras do not have the ability to save in raw image formats but instead use compression engines to save in formats such as JPEG. Depending on the specifications of the particular JPEG format used and the level of compression, information may be lost during compression. Usually, JPEG compression offers substantial compression with little information loss; however, high-frequency features can suffer a larger loss than low-frequency features.[67] In the images being evaluated, the surface roughness of the paper could introduce error through high-frequency algorithm artifacts. The compression in these areas becomes more efficient, with less information loss, when an image is under- or over-saturated.

4.5 – Digital image storage

A digital color image contains three 8-bit planes, (one for each of the RGB values) and therefore requires 24 bits of storage per pixel. However, some systems add a fourth plane (the alpha plane) that is often left blank or may contain transparency information for each pixel, creating a 32-bit image.[67] During processing, the image can be pixelated to show the plane values for each pixel or, alternatively, the color planes can be separated from one another to evaluate the entire color plane.

4.6 – Lighting

In addition to the metering device, a light source is required to measure the contrast ratio in reflected-light systems such as printed media and non-backlit E Ink screens. To measure the contrast ratio as would be perceived by the human vision system in common

settings, the light source should be common to areas in which the medium is often viewed and the sensor should closely mimic human vision.

Traditional fluorescent lighting can be used as a source for measuring contrast ratio. This type of light source is especially good for measuring real-world systems, as fluorescent lighting is found in a large number of commercial buildings. The color of fluorescent lighting is defined by its temperature as a blackbody emitter (i.e. 4100 K). The spectral distribution of a 4100-K blackbody emitter can be calculated using Planck's law, and is shown in Figure 4.5

4.7 – Comparison of contrast ratios

For benchmarking of contrast ratios, the correct systems should be carefully chosen due to the different types of contrast ratios discussed in Section 4.1. The contrast ratio of Sweet Nanotube Ink is best compared with pure reflective media, as our system is not backlit. For traditional printed media, good comparisons would be with inkjet-printed media and newsprint. The low whiteness of the newsprint leads to a lower contrast ratio than that of features inkjet-printed on general-purpose, white paper. For comparison with

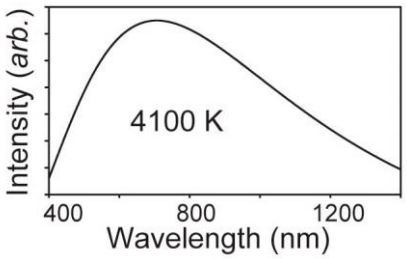

Figure 4.5. The expected spectral distribution from fluorescent lighting with a 4100 K color temperature, as used in our laboratory. The distribution has a hue that appears to the human eye as near the wavelength of the maximum intensity.

electronic media, systems must be limited to those using reflected light (non-backlit), such as eBook readers with non-backlit electronic ink screens.

Inkjet systems generate shapes by printing a pattern of individual dots or drops of ink. Often, these drops do not overlap completely. The device used to image the printed features is assumed to be unable to resolve individual drops, so the macroscopic shape will appear solid. The perceived color of the feature is a mixture of the colors of each drop along with the color of the medium. Thus, an inkjet printer can blend its black ink with the white of the medium to print a gray shape. The printer uses a lower drop density to print light gray shapes, which causes the resolution in these areas to be lower. Some newer styles of inkjet printers contain gray and/or white inks to allow for the higher resolution of light gray shapes.[70] Our system prints SWNT ink with an inkjet printer, so the best benchmark comparison is with consumer inkjet ink printed with the same system.

4.8 – Materials and Methods

The preparation of Sweet Nanotube Ink was presented in Chapter 3. Patterns were inkjet-printed (Canon PIXMA MG6120) on various media to measure the contrast ratio of the ink and to compare it to other types of ink. The pattern featured a series of overlapping rectangles printed with different consecutive passes of the inkjet heads (Figure 4.6). This pattern was used to evaluate the effect of multiple layers of ink (up to five) on the same sample and allowed for the averaging of separate areas with the same number of ink layers. The medium was cut into three inch by five inch cards. A series of the six images was sent consecutively to the printer with the print settings set to high-quality, black-and-white. After each rectangle was printed, the card was removed from the printer, dried under a

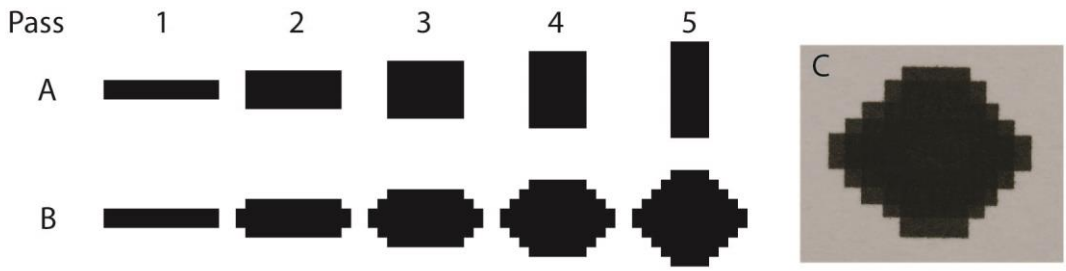

Figure 4.6. Printed patterns used for measuring contrast. **A** shows the individual feature sent to the printer with each print cycle, while **B** shows the sum of all the designs. The interior region in **B** appears darker due to an optical illusion; the pattern is a continuous shade throughout. The optical image taken from the digital camera after printing on white paper is shown in **C.** In this case the darker interior is real, and arises from the overlap of features. This overlap allows for the measurement of contrast ratio of media printed with multiple layers of ink.

stream of nitrogen, and then reloaded into the printer input tray with the original orientation. The next image was then printed over the previous image until all six images had been printed. Low-concentration carbon-nanotube solution, Sweet Tube Ink and Canon PIXMA black pigment were used for comparison.

Contrast ratio is not just a function of the ink, but also of the medium on which the ink is printed. An off-white medium will have a lower contrast ratio than a pure white medium, as the off-white medium reflects less light. The contrast-measuring pattern was printed on multi-purpose laser paper (Bose X9), off-white (ivory) resume paper (Southworth 100% cotton: Ivory), and photo paper (Kodak Matte). The ultra-white color of the photo paper was expected to give the highest contrast ratio for each type of ink used.

Digital images of the printed patterns were obtained under 4100-K fluorescent lighting. The lights were turned on at least one hour prior to image acquisition. A Canon PowerShot SX110 IS camera held in a vertical stand was used to acquire images. The camera's exposure settings were set manually.

A series of images was obtained to measure the contrast ratio of the printed media. The images were collected with exposure settings so that the black and white areas of the

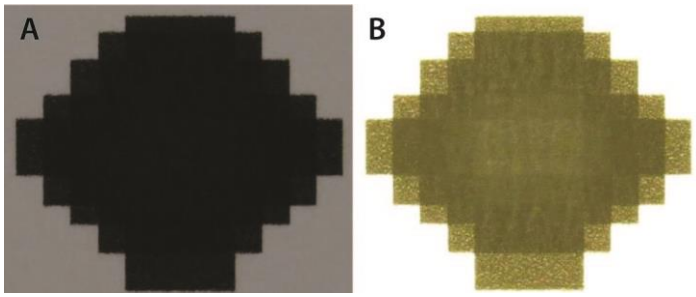

Figure 4.7. Contrast patterns imaged with a digital camera. The under-saturated image in **A** allows the white area (light gray) to fall within the dynamic range of the camera's CCD. Conversely, image **B** is oversaturated, allowing the black region (gold) to fall within the dynamic range of the sensor.

media were within the dynamic range of the CCD. The detector gain and f-number were held constant, and the shutter speed was adjusted to limit the light arriving at the CCD so that the white area of the print looked gray (Figure 4.7). At this point, the white area was in the CCD's dynamic range but the black area was under-saturated (i.e., had a value near 0). Next, the shutter speed was increased until enough light arrived at the CCD to bring the black area into the sensor's dynamic range. At this exposure setting, the white area was oversaturated (i.e., had a value close to 255). To find the correct saturation range accurately and reproducibly, a series of images was taken by varying the shutter speed for each image. The settings used for the image with the highest luminance value were considered to produce the best saturation.

The pixels were weighted by a color function and converted to the relative luminance ($Relum$) using:

$$[R(r) + G(g) + B(b)]^{\gamma} = Relum, \qquad \text{Eq. 4.1}$$

where RGB is the color plane values of each pixel; r, g, and b are the color-plane weights of 0.2, 0.6, and 0.2 respectively and γ is the gamma decoding value of 2.2 for the sRGB colorspace used in the camera.[78] This value can be converted to luminance with the shutter speed, ISO and f-number: [67,79]

$$85.5 \times \frac{f-number}{ISO \times Shutter\ Speed} \times Relum = Luminance. \qquad \text{Eq. 4.2}$$

The factor 85.5 is used to adjust for the manufacturer-specific f-number and ISO. The same camera was used throughout the experiment, so the factor can be omitted for direct comparison without changing the results. Comparing the luminance of a white area to that of a black area gives the contrast ratio. A second set of data using the same sample was acquired by changing the f-number by one stop and repeating the experiment.

4.9 – Data Processing

Due to the large number of images processed and the need to evaluate multiple areas of each image (Figure 4.8), a National Instruments LabVIEW program was written to automate the processing. The program consisted of three parts: Vision Development to load and evaluate the images, LabVIEW to process the collected data, and Visual Basic scripts to write the data to a Microsoft Excel template.

The Vision Development suite from National Instruments is an add-on module for LabVIEW. During image acquisition, the camera and sample remained stationary, so the location of the printed features in each frame was considered constant. The first image

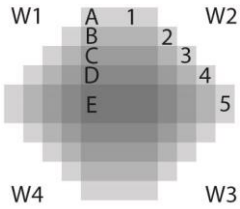

Figure 4.8. The contrast measuring pattern showing white regions W1-W4, rows A-E, and columns 1-5. Note the symmetry of the pattern across the horizontal and vertical axes. At least four replicates were measured and averaged over areas with the same layers of ink (with the exception of E1).

from a set (same sample with constant f-number and ISO but varying shutter speed) was loaded into the program and a region of interest (ROI) was selected for the alignment of the first feature, A1. Based on the location of A1, the program then automatically measured regions with no ink (W1-W4), one layer of ink (A1, B2, C3, D4 and E5), two layers of ink (B1, C2, E3 and D4), three layers of ink (C1, E3, and symmetric counterparts), four layers of ink (D1, E2 and symmetric counterparts) and five layers of ink (E1). The integer values from each plane were averaged over the selected region. After each of the 23 regions was evaluated, the next image in the series was loaded and the 23 regions were automatically measured based on the A1 ROI location selected for the first image. The luminance values for each region were calculated using Eq. 4.2 and then recorded in an Excel file.

4.10 – Results and discussion

The luminance data for a blank index card and two layers of ink are plotted in Figure 4.9. Due to the logarithmic spacing of the shutter speeds, the *x*-axis is plotted as *ln*(1/shutter speed). As the shutter speed increases, the faster integration time brings the region of interest into the dynamic range of the CCD and the luminance value increases. When comparing luminance value with shutter speed, the peak of the graph indicates the shutter speed that gives the best saturation of the region of interest. The noise at the peak is likely due to errors introduced by the compression algorithm (as discussed in Section 4.4.4). Given an appropriate model, the data could be fit to get a more accurate value for the maximum luminescence; however, the error introduced by using the maximum luminance value was found to be acceptable.

As can be seen in Figure 4.9A, the contrast ratio of standard SWNT ink (low concentration, 30 mg/L SWNTs in SDBS) is small and the features are barely discernible on the medium (Figure 4.10). Using an f-number of 3.5 and a detector gain of ISO200, the shutter speed was varied to under-and over-saturate the image. With each layer of ink, the contrast ratio increases from 1.19:1 for one layer to 1.86:1 for five layers. A second data set was obtained with the f-number set to 4.5 and the gain to ISO200. The range of contrast ratios changed from 1.19 to 1.88. These low measured ratios and visibly poor contrast demonstrate that low-concentration SWNT ink compares unfavorably to commercial black ink.

The processing efficiency of Sweet Nanotube Ink is considerably better than that of low-concentration SWNT ink, so high concentrations are easier to attain. However, concentrations above 800 mg/L are not readily inkjet printable, as the high concentration of nanotubes tends to clog the inkjet nozzles. Several concentrations were printed and the contrast ratios were measured. For the highest printed concentration, the contrast ratio

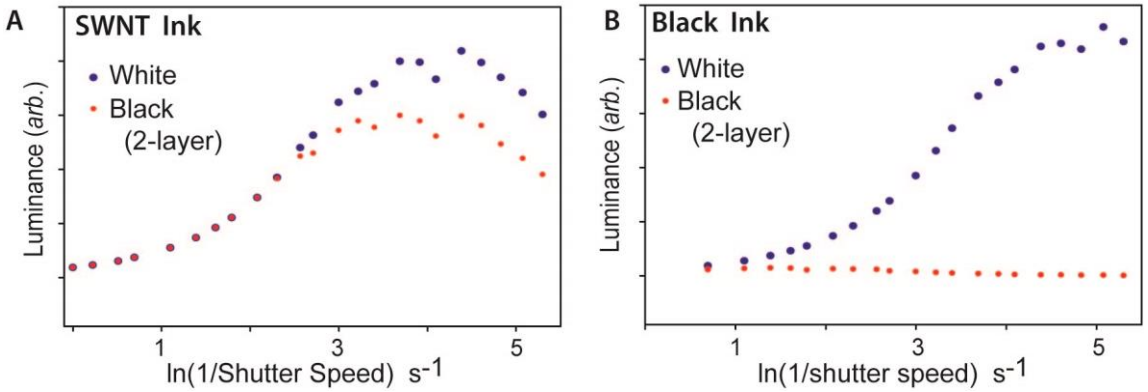

Figure 4.9. Luminance intensity plotted as a function of ln(1/shutter speed). Low-concentration SWNT ink on an index card (A) has a low contrast ratio (1.4:1), as can be seen from the closeness in intensity (and therefore shutter speed settings) of the black and white peaks. The consumer black ink on photo paper (B) has a much higher contrast ratio (32:1). Not only are the luminance intensities different (the black peak is barely visible at this scale), but the shutter speed required for each maximum varies, indicating a different saturation for the black and white regions.

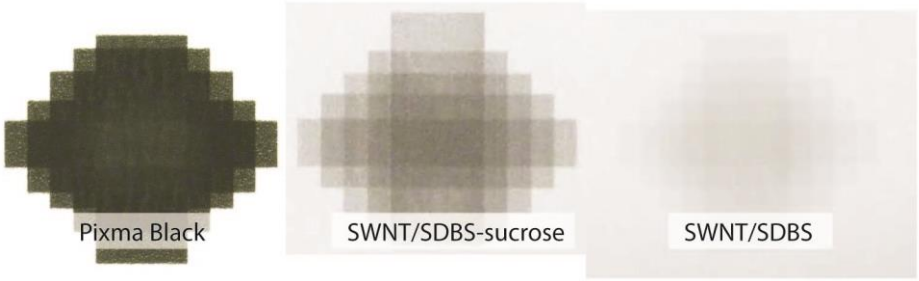

Figure 4.10. Printed contrast patterns of consumer Canon Pixma black pigment, SWNT/SDBS-sucrose (Sweet Nanotube Ink) and standard SWNT/SDBS inks. Unlike the optical illusion seen in Figure 4.6B, the light interior of the Pixma Black feature is real (measurable). The contrast ratio decreases after three layers of ink due to the larger amount of ink and solubilization of whitening agents found in the paper coming to the surface of the feature.

remained low even with five layers of printed ink. With a Sweet Nanotube Ink concentration of 800 mg/L printed on photo paper, the contrast ratio was 1.78:1 for a single layer and 5.32:1 for five layers. The printed SWNT features still looked light gray compared to features printed with consumer black ink. While SWNTs are good blackbody absorbers in the visible region, a much higher surface density is required to cover the paper so that no white shows through. To achieve this surface density, a higher concentration would have to be used (inkjet printing is not possible without optimization) or more layers would have to be printed.

The consumer-grade Canon PIXMA black pigment contrast ratio was tested in the same way. The results for these trials allowed us to compare these inks to standard values found in the market and evaluate how well the Sweet Nanotube Ink performs. The contrast ratio of PIXMA black ink was higher, with ivory resume paper having a contrast of 8:1 for a single layer and 15:1 for three, four, and five layers. As expected, the photo paper had a higher contrast with 18:1 for a single layer and a maximum of 34:1 for three layers. Interestingly, the contrast decreases for successive layers after three, a phenomenon that is visible to the naked eye on the image (Figure 4.10). This contrast decrease may be due to

whitening agents in the paper coating solubilizing in the large amount of ink to give the ink a higher reflectivity. EIZO, the manufacturer of E Ink hybrid computer monitors, reports that the contrast ratios for photo paper, copy paper, and recycled paper are 49:1, 31:1 and 10.7:1 respectively. While our measured ratios are lower, our conditions were purposely kept from ideal to mimic more closely how the ink would be seen from a consumer standpoint.

Electronic book (eBook) reader screens generally have a lower contrast ratio than printed paper, and so provide a good comparison for our SWNT based ink. The contrast ratio of a first-generation NOOK Simple Touch, an eBook reader sold by Barnes and Noble, was also tested. Note that after these experiments were performed, Barnes and Noble released a new backlit eBook reader that has the same name of Simple Touch. In testing several areas of the screen under the same conditions, the electronic ink screen was found to have a contrast ratio between 7:1 and 9:1. Thus, the eBook screen's contrast ratio is still better than our SWNT-based ink.

4.11 – Conclusion

In principle, Sweet Nanotube Ink should be an excellent true black ink due to the large absorbance background in the visible region. A true black ink would allow for a high contrast ratio when printed on white media and could be used for consumer applications. Sweet Nanotube Ink was inkjet printed on different media and the contrast ratio was measured. A consumer digital camera was used to image and calculate the luminance values for black and white elements. The ratio of these luminance values was then used directly as the contrast and was compared to other types of ink and consumer electronic

media. We found that the Sweet Nanotube ink has a low contrast ratio, even when compared to other low contrast systems such as E-Ink screens. The low contrast was due to an overall low surface density of SWNTs. Even though the carbon nanotube concentrations that were inkjet-printed are considered high for this field, they are actually low compared to concentrations of typical pigments, inks, and coatings.[80] To achieve a higher contrast ratio, a higher surface density of SWNTs would need to be placed on the medium. A higher concentration of Sweet Nanotube Ink would provide a higher surface density of nanotubes. While higher concentrations of this ink are available, we showed in Chapter 3 that they did not print well using a consumer inkjet printer. Professional and research-grade inkjet systems are available and may allow higher concentrations to be printed. These systems may also allow for more layers of ink to be printed faster with a higher placement accuracy.

Chapter 5: Dried-state interaction of single-walled carbon nanotubes with small molecules

Surfactants can be used to stabilize and suspend SWNTs individually in aqueous solution. However, stabilization is lost when the solution is dried. In Chapter 3, small molecules, such as disaccharides, were used at high concentration to give a higher processing efficiency by crowding the nanotubes during ultrasonic processing. The conclusion was drawn that in solution, small molecules do not interact with SWNTs. Also, when high concentrations of disaccharides are present in individually-dispersed SWNT solutions, the small molecules form a matrix around the SWNTs that prevents the nanotubes from re-bundling upon drying. Due to the individualized state of nanotubes, their photoluminescence is largely retained even in thin films and dried ink.

It is interesting to consider whether a solution of individually dispersed SWNTs drop-cast onto a disaccharide thin film will form the same small-molecule matrix around the nanotubes and allow them to fluorescence. As is the case in SWNT solutions, fluorescence can be used to evaluate the SWNT/small-molecule interactions. In this Chapter, I introduce a method of casting SWNTs on paper substrates to study the SWNT fluorescent spectra. When the paper is pretreated with a thin film of small molecules, interactions with these molecules lead to a shift in the SWNT fluorescence spectrum.

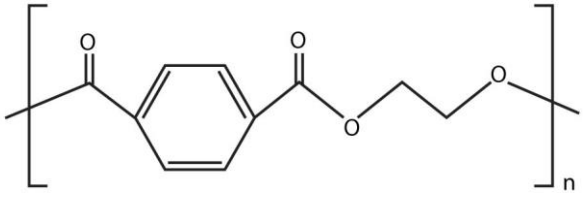

Figure 5.1. The chemical structure of polyethylene terephthalate (PET), showing the conjugated double bond system on the benzene ring that can interact with SWNTs through π-π stacking.

5.1 – Substrate choice for thin-film studies

To study the interactions of SWNTs drop-cast onto thin films of small molecules, thin films of SWNTs should be used as a control. A suitable substrate must be chosen to allow for good casting of SWNT and small-molecule thin films. Glass and silicon are popular substrates for many laboratory studies due to their smooth, controlled surfaces. However, SWNTs are known to bundle when cast on these substrates. Many polymers, such as PET, interact with carbon nanotubes, promoting adhesion.[81] The conjugated double bond in PET allows for π-π stacking with the SWNT sidewall (Figure 5.1). In certain cases, this interaction may be able to prevent bundling to a certain extent; however, if the interactions are too strong over large areas, the electronic properties of the nanotubes may be perturbed. A uniformly rough surface is thus preferred, as SWNTs will adhere to ridges, leaving pristine gaps in which electronic properties will be unaffected.

5.2 – Paper

Paper is another possible choice for a substrate.[82–85] Paper is often thought of as having a uniform surface, but the surface smoothness depends on the scale of interest. At a macroscopic level, the surface of paper is rough with random but uniform paper fibers.

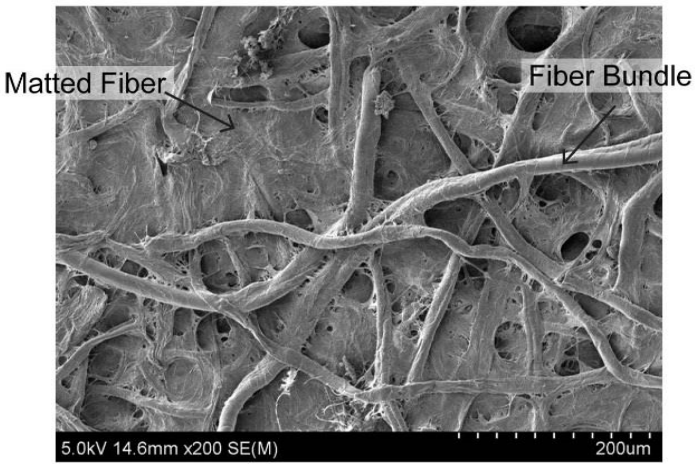

Figure 5.2. A scanning electron micrograph of chromatography paper. The paper consists of two structures: cellulose fiber bundles with average diameter 30 µm and matted fiber. This structure generates pores with two primary size distributions, larger than 30 µm and smaller than 30 µm.

At a microscopic level, the paper appears to be less uniform and contains multiple types of structures, including fiber bundles with diameters on the order of 30 µm and freely matted fibers (Figure 5.2). The fibers are made from cellulose that is thousands of saccharides long (Figure 5.3). While the fibers appear to form a continuous range of pore sizes, the pores can actually be grouped into two distributions: those larger than the fiber bundle diameters (> 30 µm) and those significantly smaller than the fiber bundle diameters (<< 30 µm). This fiber structure is discussed more in Chapter 6.

5.2.1 – Paper coatings

Paper is manufactured from cellulose fibers in the paper milling process.[86] Cellulose fibers are broken apart from their source during milling, to form what is known as pulp. The free fibers in the pulp initially have a random orientation. After compression to form sheets, the fibers have a mostly uniform alignment in the *z*-axis (i.e., normal to the sheet) but a random orientation in the *xy*-plane. Starch (long-chain saccharides) is often

used to help bind the fibers together.[86] In addition, many general-purpose white papers contain whitening agents that absorb ultraviolet (UV) light and fluoresce in the visible part of the spectrum.[87] For some molecules, the whitening agent's fluorescence could interfere with measurements of the molecule's fluorescence. SWNTs have a relatively long excitation wavelength with a small bandgap, causing the fluorescence of most semiconducting SWNT species to be in the NIR range, where whitening agent fluorescence does not interfere (Figure 3.13).

5.2.2 - Fluorescence of SWNTs on paper

In most cases, quenching due to bundling causes the optical properties of individual nanotubes to be lost when individually-dispersed SWNT solutions are dried.[31] On paper substrates, however, the fluorescence is partially retained and a fluorescence spectrum can be measured using long integration times and high-sensitivity detectors. Due to the porous nature of paper, the interaction of nanotubes with paper fibers helps to prevent bundling, leaving segments of nanotubes pristine. If the pristine region is longer than the exciton diffusion length of 90 nm, then excitons can undergo radiative decay and fluoresce.[88] When cast on paper, the retained SWNT optical properties can be used as a baseline to

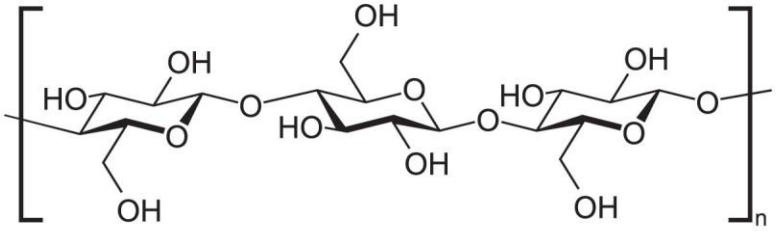

Figure 5.3. Paper fibers are made from the polysaccharide cellulose that can be hundreds to thousands of units long.

compare shifts and intensities (assuming cellulose does not interact electronically with SWNTs and cause a shift).

5.2.3 - Inconsistency of paper structure

The rough surface and nonuniform structure of paper at a microscopic level can lead to inconsistency when measuring the fluorescence of SWNTs. Two methods allow us to circumvent this problem. First, paper reservoirs help make treatment with small molecules more uniform by limiting wicking of the small-molecule solution. Second, rapid measurements, low substrate cost and small sample volumes (as small as 500 nL) allow for a large number of samples to be tested. Statistical analysis can be performed on these replicates to evaluate the average and the variance of the collected data.

5.2.4 – Paper Reservoirs

The density of the small-molecule thin films should be consistent to allow for the accurate study the interaction of SWNTs with the film. When a solution is placed on paper, it wicks or bleeds into the fiber structure of the paper. Unfortunately, this wicking process is hard to control and results in uneven and inconsistent coverage. To overcome the density variation, wax paper microfluidic reservoirs were created by using a commercially-available, wax-based printer and reflow process.[89] The wax precisely controls the reservoir's volume, allowing for the small-molecule solution to oversaturate the paper without the solution spreading. Once this solution has dried, a small volume of the nanotube solution can be dispensed in the middle of the reservoir, where the solution penetrates into the small molecule film and dries.

5.3 – Methods and materials

To study the electronic interactions of SWNTs with small molecules in thin films, CoMoCAT (6,5) nanotubes (Southwest Nanotechnologies) were first dispersed in the surfactant SDBS using the technique discussed in Chapter 2. Paper reservoirs were prepared following the procedure found in Chapter 6. Briefly, a Xerox ColorQube 8570 was used to print rectangles with dimensions of 10 mm × 7 mm on Whatman 1Ch chromatography paper. These structures were reflowed on a hot plate at 100 °C for five minutes to make solid hydrophobic barriers throughout the thickness of the paper. A saturated solution of trehalose was made with Nanopure (18 MΩ) water and then 3-5 mL of this solution was added to the center of the reservoir.

A Horiba Jobin Yvon NanoLog was used with an InGaAs CCD detector array (Symphony) to acquire fluorescence data from 900-1600 nm. The excitation monochromator was set to 570 nm to excite the high population of (6,5) SWNTs in the sample. The stock SWNT sample was diluted by a factor of 10. The fluorescence was then measured with an integration time of ten seconds. Dark noise was measured and subtracted from the signal. A stock SWNT sample volume of 500-2000 nL was added to the reservoir after the small-molecule film had dried. The sample fluorescence was then again integrated for 45 seconds and the dark noise subtracted from the signal.

In some cases, a digestion solution was added to the small-molecule/SWNT film after the initial fluorescence reading to break down the small molecules. The enzyme amylase was added to the reservoir and allowed to dry. The fluorescence measurement

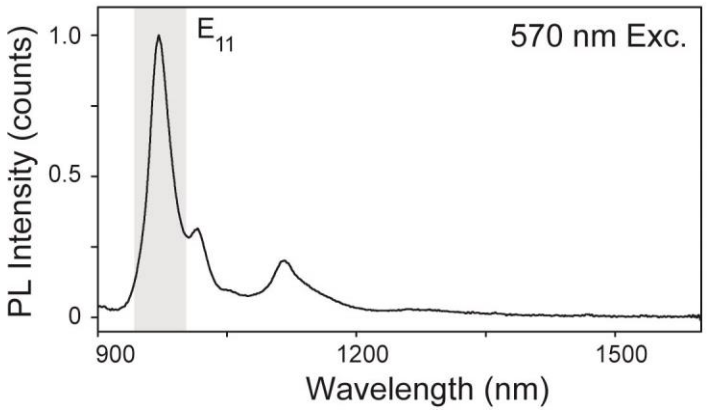

Figure 5.4. The fluorescence spectrum of CoMoCAT (6,5) SWNT solution following excitation at 570 nm. The E_{11} peak of the (6,5) nanotubes is centered at approximately 970 nm.

was then retested. Additional cycles of enzyme addition/fluorescence measurement could be performed.

5.4 – Results and Discussion

CoMoCAT (6,5) SWNTs were used due to their high percentage of (6,5) nanotubes. This species has an E_{22} absorbance at 570 nm and an E_{22} emission at ~970 nm. The stock solution was diluted to lower the absorbance and prevent quenching by re-absorption. The SWNT solution fluorescence spectrum is shown in Figure 5.4. The maximum intensity at 970.82 nm is the E_{11} emission peak from (6,5) nanotubes. This wavelength can be used to find the spectral shift of the SWNTs both on paper and on small-molecule thin films.

Control thin films of SWNTs on paper reservoirs were prepared. Figure 5.5 shows the fluorescence spectra for three different control samples (replicates). The average peak location for the (6,5) E_{11} emission peak is 974.8, nm with a standard deviation of 1.3 nm. The emission intensities varied by about 10% during these runs. The variation in the intensity ratios of the three distinguishable peaks most likely arises from a varying distribution of nanotube species. Removal of surfactant interactions would be expected to

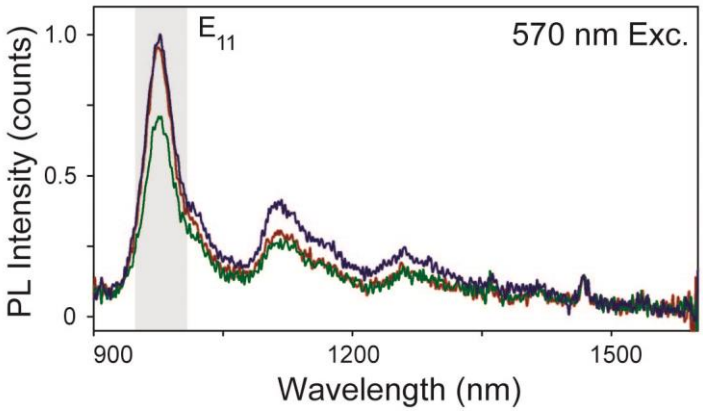

Figure 5.5. Fluorescence spectra of three replicates of a CoMoCAT (6,5) SWNT solution drop-cast on a paper substrate. The intensity of the (6,5) E11 peak varies along with the ratio of the all three visible peaks due to the inconsistency of the paper structure.

lead to a blue shift due to the loss of the dielectric screening of the SDBS and of the π-π interactions between SWNTs and SDBS. The red shift therefore must arise from interactions with the paper fibers.

The disaccharide trehalose was used in the first set of small-molecule experiments. Trehalose is a close analogue to sucrose, consisting of two α-α linked α-glucose molecules. Trehalose was reviewed briefly in Chapter 3, in which the sugar was used as an alternative to sucrose as a viscosity enhancer to boost the processing efficiency of carbon nanotubes. Trehalose has the advantage of easily forming a monohydrate, even at low humidity levels. Unlike sucrose, after the trehalose monohydrate is formed no additional water is absorbed, so the molecular weight of the compound is not influenced by high humidity levels. A 25% aqueous concentration of trehalose was used to form a thin film. Several sequential replicate experiments were performed. In nine samples, the peak position of the (6,5) E_{11} transition shifted to 997. 7 nm with a standard deviation of 1.6 nm. While the standard deviation of the peak position remains low, the change in intensity increased to 20%, with the data points scattered further from the average. Figure 5.6 shows spectra from the

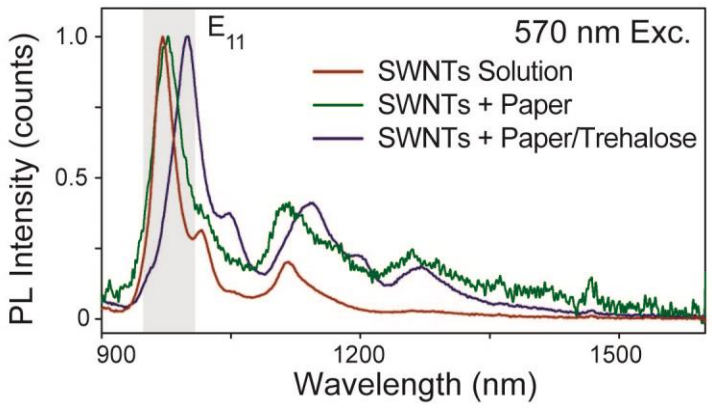

Figure 5.6. Fluorescence spectra comparing the peak shifts for a SWNT solution, a SWNT solution drop-cast on paper, and a SWNT solution drop-cast on paper pretreated with trehalose. The sample treated with trehalose has a shift of 26.9 nm in the E_{11} peak (~970 nm) relative to that of the SWNT solution. Intensities have been normalized to the E_{11} peak for comparison.

SWNT solution, a SWNT thin film, and a SWNT solution drop cast onto a trehalose thin film. The E_{11} peak has a shift of 26.9 nm between the SWNT solution and SWNT-trehalose thin film samples.

Starch is a polysaccharide built from glucose subunits. Because of the similarity of these subunit structures, we speculated that starch might lead to a spectral shift in the SWNT fluorescence similar to that of trehalose. Previous studies have reported that both starch[90] and dextrin[91] can wrap around SWNTs and can therefore be used as biologically-inert stabilizing agents for individual dispersion. However, in these previous reports the individual dispersion of the carbon nanotubes was not monitored with fluorescence.

The paper reservoirs were pretreated with a starch paste made by dissolving 500 mg of starch in boiling water. The resulting solution was allowed to cool. Using a positive displacement pipette, 5 µL of the paste was introduced onto the paper reservoir and smeared across the reservoir with a plastic spatula. After the paste dried, the SWNT stock solution was pipetted onto the reservoir and the sample's fluorescence was measured. The

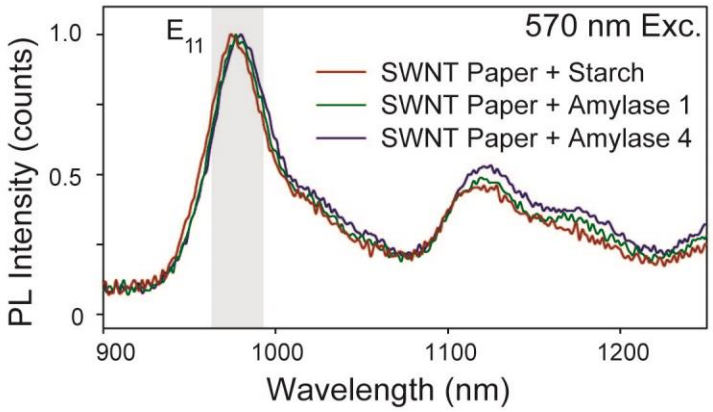

Figure 5.7 The fluorescence spectra of SWNTs drop-cast on paper pre-treated with starch. Only a small spectral shift is observed, so additions of the enzyme amylase were used to digest the starch into smaller polysaccharides, such as maltose. After the addition of amylase, a small but continuous shift was seen in the E_{11} peak of the (6,5) nanotube from 960 nm to 980 nm.

resultant spectral shift was minimal, however. 5 uL of amylase was added to the sample to digest the starch into shorter maltose chains. The fluorescence was again measures, and more enzyme was added. Figure 5.7 shows a small, yet continuous red shift in the spectrum among no amylase, one addition of amylase and four additions of amylase. At this point, more tests need to be performed to verify that the shifts arise from SWNT interactions with the shorter-chain polysaccharides.

5.5 – Conclusion

The interactions of SWNTs with different materials including substrates and small molecules is of great interest. On method to evaluate SWNT interactions is by studying the fluorescence of individually dispersed SWNTs. As discussed in Chapter 1, the electronic band structure of SWNTs is sensitive to the nanotube environment and so shift are expected upon drastic changes to the environment. Previously, it was difficult to study the spectral shifts in the fluorescence of dried SWNT solutions due to nanotube bundling. However, we showed that paper can be used as a substrate to measure SWNT fluorescence

shifts even in dried states. SWNTs can adhere to the fibrous structure of paper preventing nanotube aggregation but leaving prestine regions of SWNTs intact for fluorescence. The non-uniformity of the paper structure can be overcome by comparing a large number of samples. When SWNTs are placed on paper pretreated with trehalose, the (6,5) SWNT E_{11} emission peak shifts by as much as 26.85 nm. In addition, a small shift is observed upon drop casting of SWNTs on paper. The shift is caused by the loss of interaction with the surfactant SDS and/or the introduction of an interaction with cellulose.

Chapter 6: High-resolution paper microfluidics

In Chapter 5, paper was used as a substrate for fluorescence analysis of SWNT/small-molecule interactions. A wax-boundary reservoir was created to contain the small molecule solutions and prevent them from spreading out (bleeding) into the paper. To produce the reservoirs at a faster pace, a sheet consisting of 81 pretreated and reflowed reservoirs was prepared. An interesting phenomenon was observed during the reflow process. Typically, a significant loss in resolution occurs during reflow due to the wax bleeding into the paper fibers. However, treatment of the paper with trehalose before reflow reduced the loss in resolution. After reflow, the final line width decreased from 280% of the initial printed feature size to only 120% when the device was pretreated with sugar. In this chapter, I discuss the details of this process; this work is adapted from a manuscript to be submitted as a Technical Note to the journal *Lab on a Chip*.

6.1 – Introduction to paper microfluidics

Microfluidics continues to reshape the way many fields of science and diagnostic medicine operate.[1] For many applications, the cost of investing in microfluidics can be offset by the corresponding reduction in consumption of samples and reagents, as well as

in sample processing time. Nonetheless, certain applications require the most inexpensive of techniques, and the cost of conventional microfluidic technology remains too high. For example, third-world countries have little money to spend on diagnostic medicine .[2] Some researchers have turned to paper as a microfluidic substrate to meet these budget requirements, reducing device cost substantially.[3–5]

Paper microfluidic devices typically use a hydrocarbon/polymer material to form hydrophobic barriers through the depth of the paper, thereby forming channels and reservoirs.[3,6,7] Paper reduces the cost considerably relative to silicon, glass or polymer devices, but offers more limited functionality. The use of paper with hydrocarbon-based hydrophobic barriers is incompatible with many organic and acidic/caustic solvents. Applications of paper microfluidics have therefore been largely in the field of medicine, where buffered aqueous solutions are common. The relatively low resolution of paper microfluidics has also restricted the devices that can be manufactured. While larger devices can be created to counter this problem, when channels are too long solutions cannot be transported by capillary forces. Thus, paper microfluidics are typically large and relatively simple devices with a limited number of features.

The cost of producing paper microfluidic devices must be at a minimum for third-world applications. One low-cost approach is to use a wax-based inkjet printer to deposit the hydrophobic material, and then to follow up with a reflow step.[8,9] In reflow, the wax is heated above its melting point and is drawn into the paper to create an impenetrable,

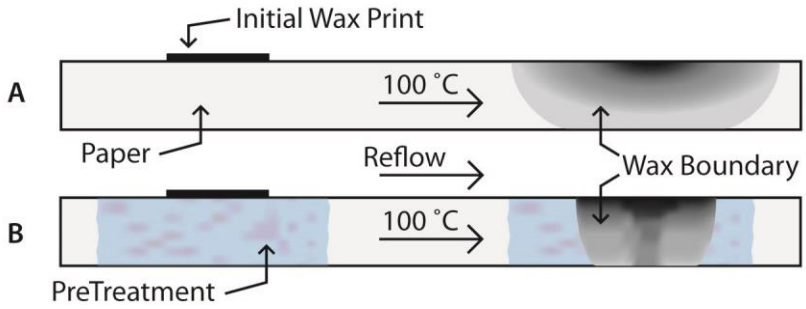

Figure 6.1. A cross section showing the reflow process of melting wax printed on paper to form hydrophobic barriers (wax boundaries). Reflow in untreated paper (A) has a large loss in resolution due to the wax wicking into the paper. The paper in B is pretreated before reflow to decrease wicking in the lateral direction limiting the loss of resolution.

hydrophobic barrier (Figure 6.1). Solutions placed inside a reservoir will remain in place, and solutions placed in a channel will wick through the paper via capillary-driven flow.

In our experiments, a Xerox ColorQube 8570 wax ink printer was used to create paper microfluidic devices. This printer has a resolution between 600 and 2400 DPI which should be able to create pixels between 10-40 μm.[10] However, with our non-ideal conditions, especially uncoated paper, and the need for features that are several pixels wide, the minimum feature size was expected to be larger. Multiple pixels are needed to guarantee solid ink coverage and provide a surface density of wax high enough to form complete barriers after reflow. The printer's ability to print feature size was measured by printing a series of lines with varying widths (Figure 6.2). The printed line width and

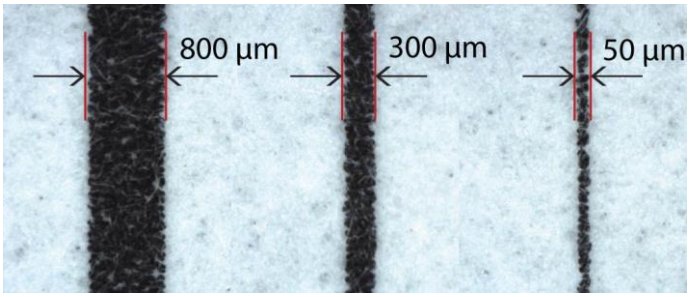

Figure 6.2. Lines printed with a Xerox ColorQube 8570 wax ink printer. The widths listed are the designed widths sent to the printer. The decrease in wax density of the 50 μm line can cause a incomplete barriers to form. The print-head orientation was parallel to these lines.

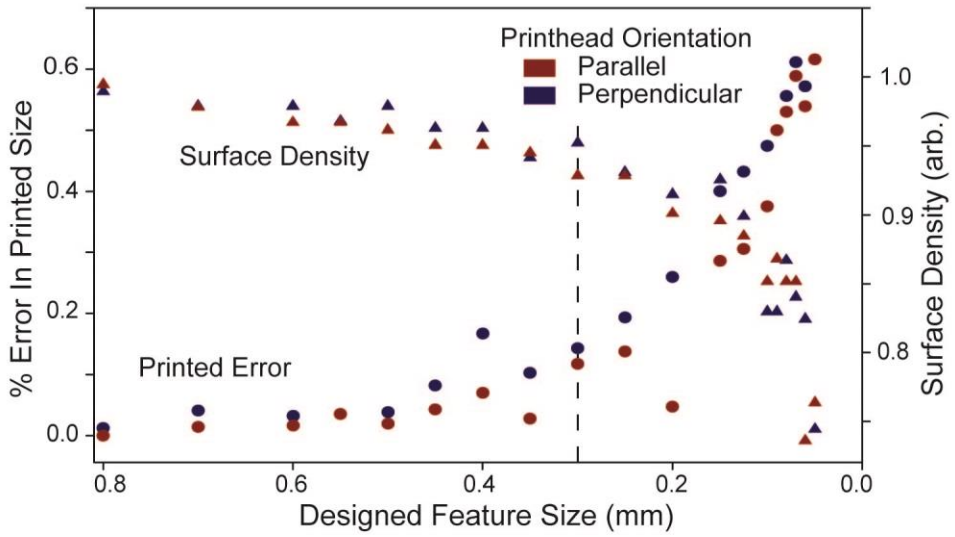

Figure 6.3. Line widths for both parallel and perpendicular orientations (to the print head) showing increased error in both printed size and surface density as smaller line widths are printed. The error increases rapidly below the chosen printed barrier size of 300 µm (vertical dashed line).

surface density were measured using the method described in Section 6.3. These measurements were compared to the designed line width with 100% surface density. When lines with a designed width of 300-µm were printed, it was found that the features were oversized by less than 10% and had a surface density greater than 90% (Figure 6.3). Designed line widths smaller than 300 µm were oversized by more than 10% and had less ink coverage. While 300 µm is acceptable for a barrier width, the reflow process increases the feature size by nearly 300%, giving a final barrier width of almost 1 mm.[9] To circumvent this sort of loss in resolution, materials such as photoresists have been used to create the hydrophobic barrier.[4,11] However, photolithographic techniques increase the cost of paper microfluidics considerably.

Here we demonstrate an in inexpensive approach for increasing the resolution of paper microfluidic devices printed with wax. By treating the paper substrate with a disaccharide such as sucrose or trehalose prior to reflow, the loss in resolution during the

reflow process is decreased substantially (Figure 6.4). An optical method was developed for monitoring the lateral (parallel to surface) and axial (normal to surface) bleeding of lines during reflow, allowing us to demonstrate that treatment with sugar slows down the kinetics of the wax transport through the paper by nearly eliminating some transport mechanisms. This increased resolution can be used to produce smaller devices and to expand device functionality.

6.2 – Methods and materials

All of our experiments were performed using a modification of the process introduced by Lu *et al.*[8] and evaluated in detail by Carrilho *et al.*[9] All printing was performed on Whatman 1 Chr standard chromatography paper. The printer settings were fixed to black and white with enhanced resolution. The wax was reflowed by placing the device on a digital hotplate set to 100 °C. The actual surface temperature of the hotplate varied from 77 °C to 93 °C as the heating element turned on and off. This wide variation in temperature did not have an adverse effect on the reflow process, which proved highly consistent from sample to sample.

For sugar-treated devices, enough saturated disaccharide solution was added to the back side (the opposite of the printed side) of the paper to saturate the region around the wax (typically around 10-20 uL depending on the design). The solution was allowed to spread and soak into the paper before reflow. The device was then placed in a glassware oven at 65 °C (top rack) for five minutes followed by 70 °C (bottom rack) for five minutes to dry the disaccharide solution. Saturated disaccharide solutions were prepared by adding

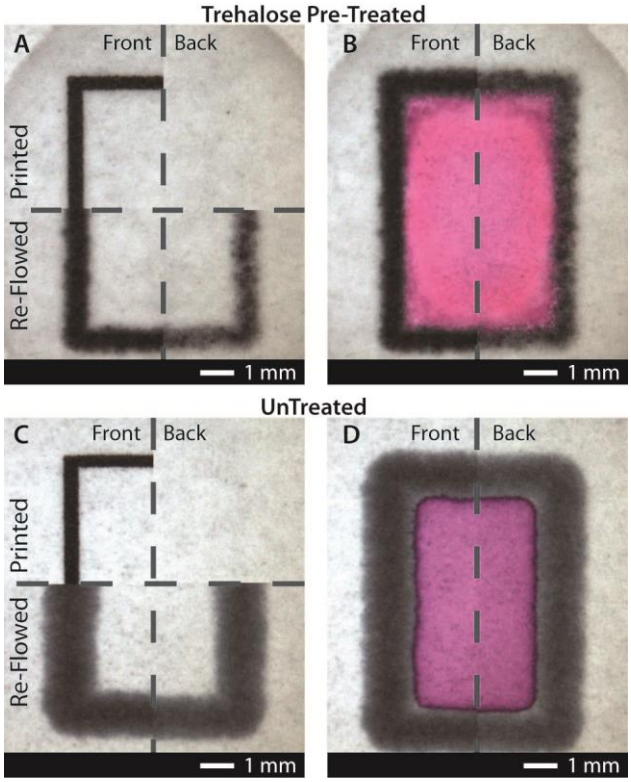

Figure 6.4. Paper microfluidic reservoirs before and after reflow showing the large loss in resolution for untreated devices (C) compared to trehalose treated devices (A). Rhodamine B dye can be retained in each (B and D) even with the blotchy back of the pre-treated device.

an excess of the disaccharide (trehalose: Swanson Ultra 100% - dietary grade, super-saturation: ~ 0.9 mg/mL; sucrose: Sigma ACS grade, super-saturation: ~1.5 mg/mL) to boiling water. After dissolving the disaccharide and cooling to crystallize out the excess sugar, the mother liquor was used as the saturated solution. The saturation point of sucrose is higher than that of trehalose, so sucrose solutions were diluted to 55% of the saturated concentration before use. The ability to make a saturated solution with no laboratory equipment greatly simplifies the process and increases the usefulness of the method when cost is a concern.

6.3 – Digital image correlation setup

During reflow, the devices were monitored visually to measure the material transport rate (Figure 6.5). Digital image correlation (DIC) allowed the width and surface density to be measured before, during and after reflow. A front-lit stereo microscope with 7.5× zoom and a 5-megapixel camera was used for imaging (AMScope MA500). Time-lapse video imaging with a resolution of 2 s was used to collect images during the reflow process. LabVIEW (including the Vision Development module) was used to analyze the image sets. Absolute dimensions were determined using a calibration standard (AMScope MR400).

6.3.1 – Line-width measurements

The change in barrier width during reflow was recorded using video capture. To compare treated and untreated devices during reflow, the barrier widths in each image were

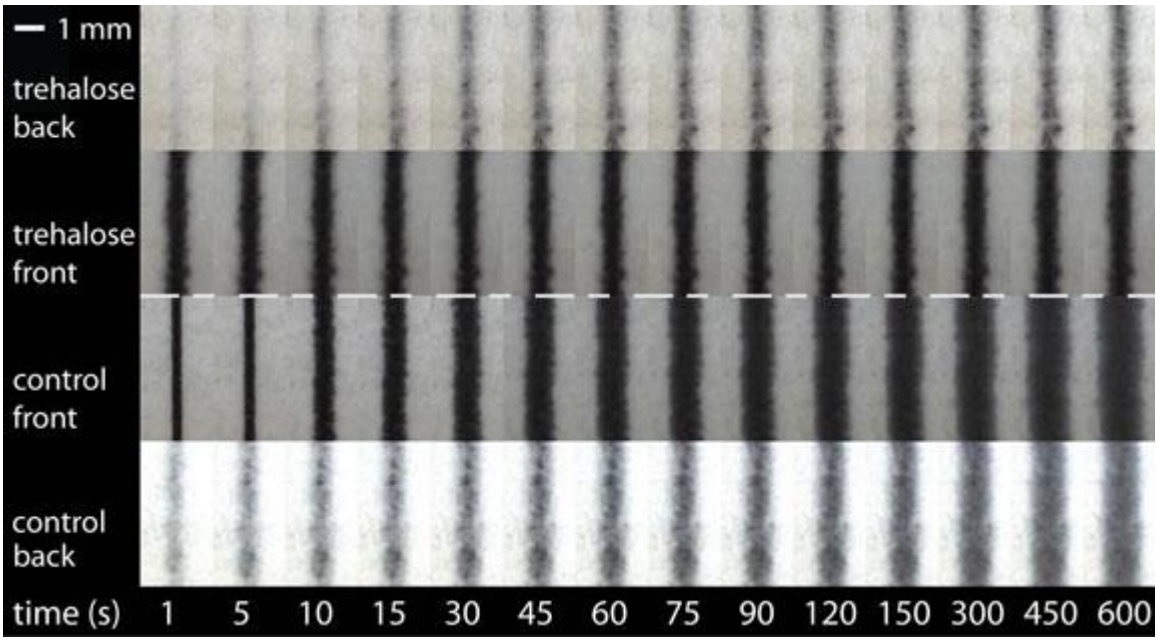

Figure 6.5. Time-dependent imaging of the reflow process allowed DIC to be used to evaluate changes in both the width and the surface density of the features.

measured using DIC by evaluating the line profile normal to the printed feature. The width of the barrier was determined from the full width at half maximum of the measured line profile (Figure 6.6). To account for feathering and edge roughness of the printed features, a line parallel to the barrier was chosen and the program measured line profiles across multiple random points. The data from these points were then averaged.

6.3.2 – Surface-density measurements

The relative surface density of the printed area was also monitored during reflow, allowing us to estimate the transport of wax through the paper in the axial direction. Using the same image set as in the width measurements, a central region of interest (ROI) incorporating only the printed feature was selected for evaluation. The LabVIEW program gathered information from each frame based on the selected ROI. Due to the black color of the wax ink on white paper, the amount of wax on the surface can be evaluated in a manner similar to that used for contrast ratio measurements in Chapter 4. The three color planes were separated and the average pixel integer was calculated for the ROI. A color-weighting function of 1:1:1 was used to combine the RGB integers together, giving an

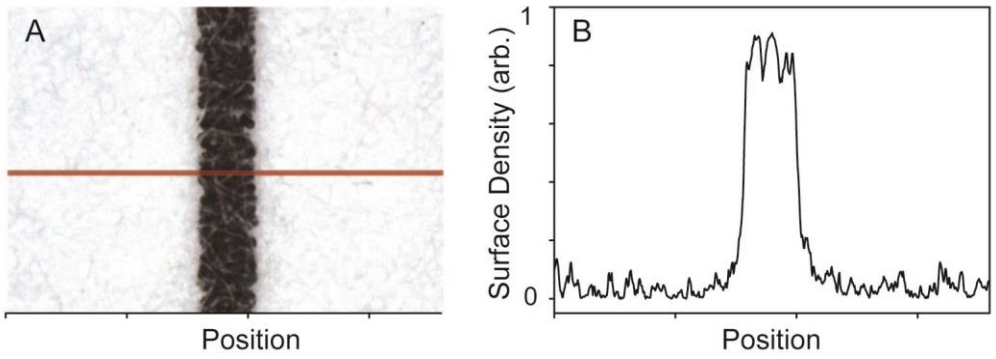

Figure 6.6. The width of the printed line in **A** can be calculated by measuring the line profile across a line normal to the feature (red horizontal line). The width is calculated to be the full width at half max of the line profile (**B**).

average 8-bit value for the region. This value is the relative surface density, and can be compared to other frames from the same sample.

6.4 – Results

For reservoirs, a designed barrier width of 300 μm was chosen. To study the loss in resolution from reflow of 300 μm lines, a set of reservoirs was printed and the line widths of the devices were monitored. Three replicates of both treated and untreated devices were tested. The barrier width for untreated devices increased to 280% of the printed line width. However, devices treated with trehalose had a final line width of 120% of the printed line.

To study how the wax bleeds into the paper structure, we want to evaluate a system where the initial material transport is not limited by the available wax (material limited) but instead by the transport mechanism itself (transport limited). A 4 mm × 4 mm solid rectangle was printed and reflowed to evaluate a system that is not material limited. During reflow, the surface density of wax in the center of the device was monitored to determine how the wax bleeds into the paper. For each solid rectangle measured, the front (printed) side still had a different appearance from the back side even for times much greater than the time of melt ($t>>t_m$) when reflow was complete (Figure 6.7A). Due to the excess of wax in the center of the device, this difference in front and back demonstrates that the mechanism is transport limited. For solid rectangles treated with trehalose, the rate of material transport through the paper/disaccharide matrix was slower than that of the untreated devices, indicating the transport kinetics are slower in the treated devices. In addition, even with the lower backside density, trehalose-treated devices exhibit good aqueous solution retention over long time periods (Figure 6.4).

For the solid rectangle devices, the changes in feature width and surface density with time are plotted in Figure 6.7B. Note that the program is only used to measure widths on the device front (printed side), due to low initial contrast on the backside. For an untreated device, the width increases linearly with time during the data collection period. The shape of the width expansion and surface density increase are quite different. However, when the device is treated with trehalose, the change in width during reflow is considerably smaller at any given time. This change from a linear expansion of width in the untreated case to an asymptotic limit in the treated case suggests that there are multiple

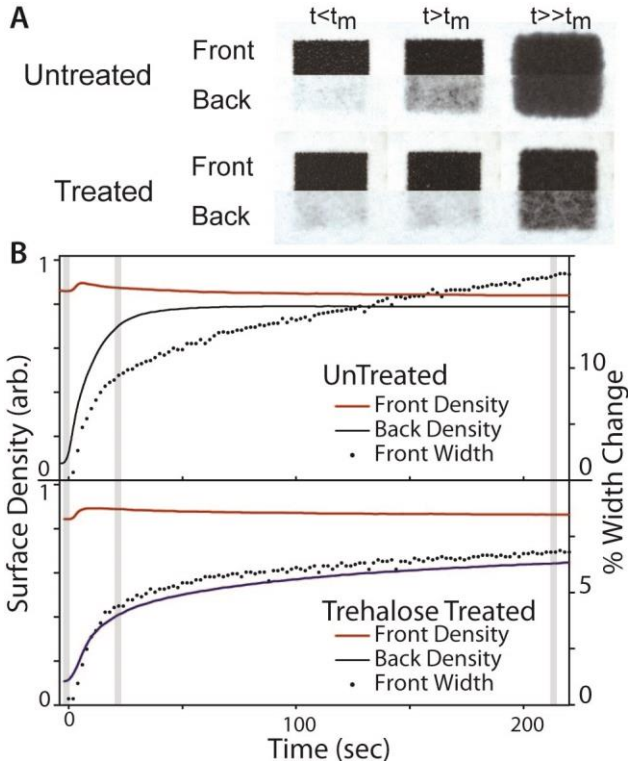

Figure 6.7. Optical images (A) of the front and back of devices designed to be transport limited. Note that the back is distinguishable from the front even for $t>>t_m$. DIC was used to monitor the surface density and width of the feature during reflow (B). In a treated device, the change in surface density is slower for both the front and the back of the device. The change in feature width of the trehalose-treated device has a shape that is similar to that of the change in backside density, suggesting a similar transport mechanism for the wax bleeding laterally and axially through the paper.

material transport mechanisms in an untreated device. Similar results were found using sucrose treatment.

6.5 – Discussion

Carrihlo *et al.* showed that the bleeding in a transport-limited system such as wax in paper can be modeled using Washburn's equation:[9]

$$L = \frac{\gamma D t}{4\eta} \qquad \text{Eq. 6.1}$$

where L is the distance a solution with viscosity η and surface tension γ travels through a porous medium with average pore diameter D in time t. Eq 6.1 implies that the material transport is a function of pore size. However, paper contains a large distribution of pore sizes and structures. In general, the pore-size distribution can be grouped into two ranges: those smaller than the diameter of the paper fiber bundles and those much larger than the diameter of the paper fiber bundles. Here, we refer to these groups as primary pores, which are interior to the fibers, and secondary pores, which correspond to the voids among the fibers (Figure 6.8). Due to the compressive nature of paper milling, the orientation of the paper fibers is random in the lateral direction but is highly oriented in the axial direction. Thus, transport through primary pores is constrained largely to the lateral direction, while transport through secondary pores is omnidirectional.

Comparison of the width and surface density data for untreated and treated devices suggests that the transport through primary pores is present in the former but is virtually eliminated in the latter, leaving only transport through the secondary pores. This effect causes the axial and lateral transport kinetics to be similar in the sugar-treated devices. The blocking of primary pores is proposed to be caused by either the disaccharide completely

filling the primary pores of the paper fiber or completely encapsulating the fiber, thus blocking access to the primary pores.

6.6 – Conclusion

Paper microfluidics are a low cost version of microfluidics which can fit into many budget constrained systems. However, to this point the techniques used to manufacture paper microfluidics such as wax-based printed barriers can only provide low resolution

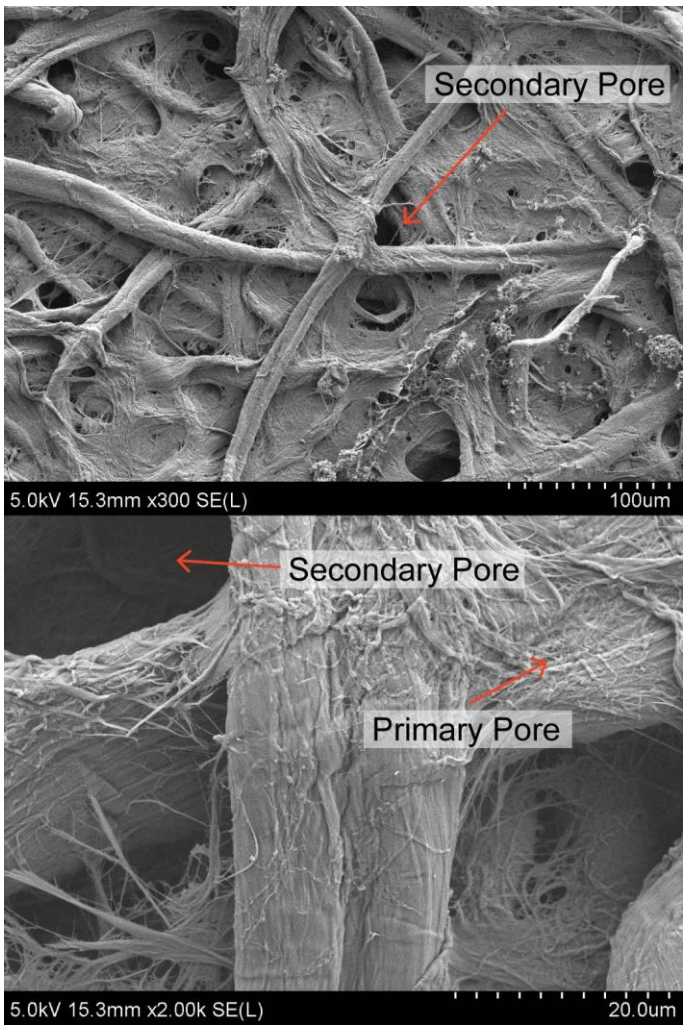

Figure 6.8. Scanning electron micrographs of chromatography paper showing primary pores (smaller than a paper fiber bundle) and secondary pores (much larger than a paper fiber bundle).

devices. Low resolution devices loose functionality due to their large size and inability for solutions to wick through the paper over long distances. Turning to other methods to produce higher resolution devices has proved to increases the cost of paper microfluidics. We found that pretreating paper microfluidic devices with disaccharides before the reflow process decreased the size of the devices by decreasing the amount of bleeding in the lateral direction during reflow. Solutions, including the molten-wax-based ink, are transported (wicked) through the pores of the paper. Blocking one of the types of pore structures with sugar allows for greater control over reflow to produce features with a final size that is 60% smaller than features on untreated devices. Smaller feature sizes can be used to increase the functionality of paper microfluidic devices by allowing more features to be implemented within the wicking region of the sample reservoir.

Chapter 7: Conclusions and future work

7.1 Conclusions

Much progress has been made in the carbon nanotube field since their structure was elucidated in 1991. Many of the properties have been predicted theoretically and later verified experimentally; however, while a large number of potential applications are envisioned few have been translated to widespread consumer products. Many studies of SWNT solutions are restricted to small and limited systems that are incompatible with the complexities of consumer applications. A better understanding of how SWNTs interact with complex mixtures beyond their stabilizing surfactants is critical to expanding the field.

In Chapter 2, a cooling jacket and a more effective surfactant were used to almost double the processing efficiency. The cooling jacket stabilizes the SWNT solution temperature during sonication. Sodium dodecylbenzenesulfate (SDBS) was used as a surfactant. SDBS is similar to sodium dodecylsulfate (SDS) but contains a benzene ring between the polar head and non-polar tail. The conjugated double bonds in the benzene ring can undergo π- π stacking with the SWNT sidewall. While better surfactants exist for dispersing SWNTs, SDBS's commonality makes it readily available at a low price.

Temperature control and a more efficient surfactant allowed SWNTs to be individually dispersed with a yield of 7.44% which remained linear to unprecedented concentrations.

Viscosity enhancers (increasers) were studied in Chapter 3 to further boost the efficiency of individual dispersion. After cavitation exfoliates a SWNT from a bundle, presumably there is a finite period of time to stabilize the nanotube with surfactant encapsulation or polymer wrapping before the nanotube will rebundle. The high aspect ratio of SWNTs gives them a slower motion in solution than surfactant molecules. By increasing the viscosity, the difference in this motion can be exaggerated thus increasing the time period for stabilizers to act on the SWNT. Several molecules were evaluated as viscosity enhancers but sucrose was studied in depth. Using sucrose, SWNTs were dispersed to concentration as high as 3.35 g/L with an efficiency of 24%. The upper bound of this concentration was limited by the shear amount of initial solid material to solvent ratio and not the dispersion process itself. These highly concentrated solutions were verified to contain individual SWNTs by showing the retention of the SWNT photoluminescence.

An additional study performed in Chapter 3 involved using these highly concentrated solutions as inks. While these solutions can be loaded into technical pens for handwriting, their properties give them good jettability in consumer inkjet printers. Several patterns were printed and an interesting discovery was made. Fluorescence was retained after the ink dried on the paper substrate. Typically, when solutions of individually dispersed SWNTs are dried, the encapsulating surfactants lose the ability to stabilize the nanotubes and bundles are then formed. When our sucrose-laced samples were dried, the sucrose acted as a scaffolding that prevented SWNT bundling and, therefore, quenching

with metallic nanotube species. Alternatively, the nanotubes could be spread on a flat polymer surface using a Mayer Rod. Fluorescence was once again retained in these samples. However, upon washing the samples with ethanol and water, the sucrose scaffolding was removed and the fluorescence quenched.

The contrast ratio of highly concentrated Sweet Nanotube Inks was measured in Chapter 4. The black body absorber background of SWNTs was expected to provide a *true black* base for the ink. A consumer digital camera was used to take images of the printed features in an everyday environment and then the luminance values from different elements were calculated. A comparison was made with both consumer-grade black inkjet ink and a First Edition NOOK Simple Touch. Unfortunately, the contrast ratio was found to be poor, on the order of 1.8: – 5.3:1 depending on the number of layers of Sweet Nanotube ink. Consumer-grade black ink and the NOOK had contrast ratios of 34:1 and 9:1, respectively. The low contrast ratio of Sweet Nanotube ink was due to a low surface density of printed nanotubes. While the achieved concentration is high for nanotube science, the concentration is more than 10× lower compared to the concentration of pigments and dyes used in inks and coating.

Chapter 5 approached the interaction of individually dispersed and surfactant stabilized SWNTs with small molecules. Paper was chosen as a substrate due to the rough surface and the interaction of cellulose fibers with nanotubes. SWNTs drop cast on paper partially retained their fluorescent properties. The paper fibers act as a scaffolding thus allowing SWNT regions longer than the exciton diffusion length to remain unbundled. The SWNT fluorescence could therefore be measured using long integration times. Paper microfluidic reservoirs were made to control the spreading of trehalose and starch solutions

on the substrates. On paper, the E_{11} peak for (6,5) SWNTs was found to have only a small ref-shift compared to the SWNT solution. A shift of 26.8 nm was seen in the E_{11} peak when the paper was pretreated with trehalose. Only a small spectral shift was seen in the E_{11} peak with starch treatment. However, upon the addition of amylase, the starch was digested to smaller polysaccharides similar to trehalose. The peak position red-shifted by a small amount with each addition of amylase. Additional studies need to be performed to verify the interaction of SWNTs with these smaller chain polysaccharides.

Chapter 6 explores the effects of small molecules on a similar system without carbon nanotubes; cellulose rods (paper fibers) with trehalose. During the work in Chapter 5, a discovery was made that the paper microfluidic reservoir resolutions could be significantly increased by pretreating the paper with trehalose or sucrose. The paper structure has pores that can be grouped into two broad classes: pores that are larger than the diameter of a fiber bundle (>30 μm) and pores that are much smaller than this diameter (<<30 μm). The kinetic rate of transport becomes similar in both the axial and lateral direction when the disaccharide blocks a transport path that only exists in the lateral direction. The resolution of the final features increased by 40% due to the greater control in the reflow process caused by blocking the secondary lateral transport.

7.2 – Future Work

7.2.1 – Sweet Nanotube Ink

The highly concentrated SWNT ink studied in Chapter 3 and Chapter 4 retains its fluorescent properties even after being dried on a substrate. The complex structure

associated with the fluorescence spectrum along with the E_{11} fluorescence in the near infra-red (NIR) part of the spectrum makes the highly concentrated ink a great candidate for security and identification ink. Applications for security ink include anti-counterfeiting, document security and tracking. A full patent application has been filed through the Department of Office Technology Commercialization (OTC) at the University of Maryland. Over the past year, the technology was chosen and has been used in two graduate entrepreneurships courses taught in the Smith School of Business at the University of Maryland. The students in these classes have identified several market areas and companies to pitch this product to. Support for them and OTC will continue in making samples for demonstration and commercial testing; however, at this time no further investigation is planned.

7.2.2 - Small molecules interactions with nanotubes

The experiments discussed in Chapter 5 were preliminary work and so future studies are important to better understand the interactions of SWNTs with different small-molecules. The mechanisms need to be verified through additional studies to correspond each shift with specific interactions among the surfactant, paper and the small molecules. These studies could be done using solutions of SWNTs dispersed in different surfactants such as SDS and SDBS, varying the small molecules and adding washing steps with various solvents known to solvate micelles. Many other saccharides, disaccharides and polysaccharides are available to study, including the fundamental building blocks glucose and fructose. Measuring additional replicate samples will allow for a more in-depth

statistical analysis. Performing these additional studies could eventually lead to a better understanding of how SWNTs interact with paper and themselves to form bundles.

References

(1) Radushkevich, L. V.; Lukyanovich, V. M. *Russ. J. Phys. Chem.* **1952**, *26*, 88.

(2) Iijima, S. *Nature* **1991**, *354*, 56.

(3) Saito, R.; Dresselhaus, G.; Dresselhaus, M. S.; Salvetat, J.-P.; Bonard, J.-M.; Bacsa, R.; Stöckli, T.; Forró, L. *Physical properties of carbon nanotubes*; 2nd ed.; Imperial College Press: London, 1998; pp. 467–480.

(4) O'Connell, M. J.; Bachilo, S. M.; Huffman, C. B.; Moore, V. C.; Strano, M. S.; Haroz, E. H.; Rialon, K. L.; Boul, P. J.; Noon, W. H.; Kittrell, C.; Ma, J.; Hauge, R. H.; Weisman, R. B.; Smalley, R. E. *Science* **2002**, *297*, 593.

(5) Moore, V. C.; Strano, M. S.; Haroz, E. H.; Hauge, R. H.; Smalley, R. E.; Schmidt, J.; Talmon, Y. *Nano Lett.* **2003**, *3*, 1379.

(6) Thess, A.; Lee, R.; Nikolaev, P.; Dai, H.; Petit, P.; Robert, J.; Xu, C.; Lee, Y. H.; Kim, S. G.; Rinzler, A. G.; Colbert, D. T.; Scuseria, G. E.; Tomanek, D.; Fischer, J. E.; Smalley, R. E. *Science* **1996**, *273*, 483.

(7) Treacy, M. M. J.; Ebbesen, T. W.; Gibson, J. M. *Nature* **1996**, *381*, 678.

(8) Kim, P.; Shi, L.; Majumdar, A.; McEuen, P. *Phys. Rev. Lett.* **2001**, *87*, 215502.

(9) Zhou, Y.; Gaur, A.; Hur, S. H.; Kocabas, C.; Meitl, M. A.; Shim, M.; Rogers, J. A. *Nano Lett.* **2004**, *4*, 2031.

(10) Ghosh, S.; Bachilo, S. M.; Weisman, R. B. *Nat. Nanotechnol.* **2010**, *5*, 443.

(11) Wong, H. S. P.; Akinwande, D. *Carbon Nanotube and Graphene Device Physics*; Cambridge University Press: Cambridge, 2011.

(12) Bachilo, S. M.; Strano, M. S.; Kittrell, C.; Hauge, R. H.; Smalley, R. E.; Weisman, R. B. *Science* **2002**, *298*, 2361.

(13) Qian, H.; Georgi, C.; Anderson, N.; Green, A. A.; Hersam, M. C.; Novotny, L.; Hartschuh, A. *Nano Lett.* **2008**, *8*, 1363.

(14) Jones, M.; Engtrakul, C.; Metzger, W.; Ellingson, R.; Nozik, A.; Heben, M.; Rumbles, G. *Phys. Rev. B* **2005**, *71*, 1.

(15) Chen, J.; Hamon, M.; Hu, H.; Chen, Y.; Rao, A.; Eklund, P.; Haddon, R. *Science* **1998**, *282*, 95.

(16) Weisman, R. B.; Bachilo, S. M.; Tsyboulski, D. *Appl. Phys. A Mater. Sci. Process.* **2004**, *78*, 1111.

(17) Girifalco, L.; Hodak, M.; Lee, R. *Phys. Rev. B* **2000**, *62*, 13104.

(18) Bergin, S. D.; Nicolosi, V.; Streich, P. V.; Giordani, S.; Sun, Z.; Windle, A. H.; Ryan, P.; Niraj, N. P. P.; Wang, Z.-T. T.; Carpenter, L.; Blau, W. J.; Boland, J. J.; Hamilton, J. P.; Coleman, J. N. *Adv. Mater.* **2008**, *20*, 1876.

(19) Parra-Vasquez, A. N. G.; Behabtu, N.; Green, M. J.; Pint, C. L.; Young, C. C.; Schmidt, J.; Kesselman, E.; Goyal, A.; Ajayan, P. M.; Cohen, Y.; Talmon, Y.; Hauge, R. H.; Pasquali, M. *ACS Nano* **2010**, *4*, 3969.

(20) Davis, V. A.; Ericson, L. M.; Parra-Vasquez, A. N. G.; Fan, H.; Wang, Y.; Prieto, V.; Longoria, J. A.; Ramesh, S.; Saini, R. K.; Kittrell, C.; Billups, W. E.; Adams, W. W.; Hauge, R. H.; Smalley, R. E.; Pasquali, M. *Macromolecules* **2004**, *37*, 154.

(21) Liang, F.; Sadana, A. K.; Peera, A.; Chattopadhyay, J.; Gu, Z.; Hauge, R. H.; Billups, W. E. *Nano Lett.* **2004**, *4*, 1257.

(22) Deng, S.; Brozena, A. H.; Zhang, Y.; Piao, Y.; Wang, Y. *Chem. Commun.* **2011**, *47*, 758.

(23) Strano, M. S.; Huffman, C. B.; Moore, V. C.; O'Connell, M. J.; Haroz, E. H.; Hubbard, J.; Miller, M.; Rialon, K.; Kittrell, C.; Ramesh, S.; Hauge, R. H.; Smalley, R. E. *J. Phys. Chem. B* **2003**, *107*, 6979.

(24) Zheng, M.; Jagota, A.; Semke, E. D.; Diner, B. A.; McLean, R. S.; Lustig, S. R.; Richardson, R. E.; Tassi, N. G. *Nat. Mater.* **2003**, *2*, 338.

(25) O'Connell, M. J.; Boul, P.; Ericson, L. M.; Huffman, C.; Wang, Y.; Haroz, E.; Kuper, C.; Tour, J.; Ausman, K. D.; Smalley, R. E. *Chem. Phys. Lett.* **2001**, *342*, 265.

(26) Bandyopadhyaya, R.; Nativ-Roth, E.; Regev, O.; Yerushalmi-Rozen, R. *Nano Lett.* **2002**, *2*, 25.

(27) Yan, L. Y.; Poon, Y. F.; Chan-Park, M. B.; Chen, Y.; Zhang, Q. *J. Phys. Chem. C* **2008**, *112*, 7579.

(28) Liu, H.; Nishide, D.; Tanaka, T.; Kataura, H. *Nat. Commun.* **2011**, *2*, 309.

(29) Tu, X.; Manohar, S.; Jagota, A.; Zheng, M. *Nature* **2009**, *460*, 250.

(30) Islam, M. F.; Rojas, E.; Bergey, D. M.; Johnson, A. T.; Yodh, A. G. *Nano Lett.* **2003**, *3*, 269.

(31) Ervin, M. H.; Miller, B. S.; Hanrahan, B.; Mailly, B.; Palacios, T. *Electrochim. Acta* **2012**, *65*, 37.

(32) Davis, V. A.; Parra-Vasquez, A. N. G.; Green, M. J.; Rai, P. K.; Behabtu, N.; Prieto, V.; Booker, R. D.; Schmidt, J.; Kesselman, E.; Zhou, W.; Fan, H.; Adams, W. W.; Hauge, R. H.; Fischer, J. E.; Cohen, Y.; Talmon, Y.; Smalley, R. E.; Pasquali, M. *Nat. Nanotechnol.* **2009**, *4*, 830.

(33) Xu, G.-H.; Zhang, Q.; Huang, J.-Q.; Zhao, M.-Q.; Zhou, W.-P.; Wei, F. *Langmuir* **2010**, *26*, 2798.

(34) Bandow, S.; Rao, A. M.; Williams, K. A.; Thess, A.; Smalley, R. E.; Eklund, P. C. *J. Phys. Chem. B* **1997**, *101*, 8839.

(35) Silvera-Batista, C. A.; Weinberg, P.; Butler, J. E.; Ziegler, K. J. *J. Am. Chem. Soc.* **2009**, *131*, 12721.

(36) Strano, M. S.; Moore, V. C.; Miller, M. K.; Allen, M. J.; Haroz, E. H.; Kittrell, C.; Hauge, R. H.; Smalley, R. E. *J. Nanosci. Nanotechnol.* **2003**, *3*, 81.

(37) Wallace, E. J.; Sansom, M. S. P. *Nanotechnology* **2009**, *20*, 045101.

(38) Angelikopoulos, P.; Gromov, A.; Leen, A.; Nerushev, O.; Bock, H.; Campbell, E. E. B. *J. Phys. Chem. C* **2010**, *114*, 2.

(39) Richard, C.; Belavoine, F.; Schultz, P.; Ebbesen, T. W.; Mioskowski, C. *Science (80-.).* **2003**, *300*, 775.

(40) Liu, J.; Ducker, W. A. *Langmuir* **2000**, *16*, 3467.

(41) Matarredona, O.; Rhoads, H.; Li, Z.; Harwell, J. H.; Balzano, L.; Resasco, D. E. *J. Phys. Chem. B* **2003**, *107*, 13357.

(42) Vaisman, L.; Wagner, H. D.; Marom, G. *Adv. Colloid Interface Sci.* **2006**, *128-130*, 37.

(43) Suslick, K. *Sci. Am.* **1989**, 80.

(44) Zeiger, B. W.; Suslick, K. S. *J. Am. Chem. Soc.* **2011**, 14530.

(45) Zhou, X.; Boey, F.; Zhang, H. *Chem. Soc. Rev.* **2011**, *40*, 5221.

(46) Engel, M.; Small, J. P.; Steiner, M.; Freitag, M.; Green, A. A.; Hersam, M. C.; Avouris, P. *ACS Nano* **2008**, *2*, 2445.

(47) Simmons, T. J.; Hashim, D.; Vajtai, R.; Ajayan, P. M. *J. Am. Chem. Soc.* **2007**, *129*, 10088.

(48) Ericson, L. M.; Fan, H.; Peng, H.; Davis, V. A.; Zhou, W.; Sulpizio, J.; Wang, Y.; Booker, R. D.; Vavro, J.; Guthy, C.; Parra-Vasquez, A. N. G.; Kim, M. J.; Ramesh, S.; Saini, R. K.; Kittrell, C.; Lavin, G.; Schmidt, H.; Adams, W. W.; Billups, W. E.; Pasquali, M.; Hwang, W.-F.; Hauge, R. H.; Fischer, J. E.; Smalley, R. E. *Science* **2004**, *305*, 1447.

(49) Hu, L.; Choi, J. W.; Yang, Y.; Jeong, S.; La Mantia, F.; Cui, L.-F.; Cui, Y. *Proc. Natl. Acad. Sci. U. S. A.* **2009**, *106*, 21490.

(50) Ha, M.; Xia, Y.; Green, A. A.; Zhang, W.; Renn, M. J.; Kim, C. H.; Hersam, M. C.; Frisbie, C. D. *ACS Nano* **2010**, *4*, 4388.

(51) Kordás, K.; Mustonen, T.; Tóth, G.; Jantunen, H.; Lajunen, M.; Soldano, C.; Talapatra, S.; Kar, S.; Vajtai, R.; Ajayan, P. M. *Small* **2006**, *2*, 1021.

(52) Mustonen, T.; Mäklin, J.; Kordás, K.; Halonen, N.; Tóth, G.; Saukko, S.; Vähäkangas, J.; Jantunen, H.; Kar, S.; Ajayan, P. M.; Vajtai, R.; Helistö, P.; Seppä, H.; Moilanen, H. *Phys. Rev. B* **2008**, *77*, 1.

(53) Weisman, R. B.; Bachilo, S. M.; Booth, E. C. Fluorescent Security Ink Using Carbon Nanotubes. 7,682,523 B2, 2004.

(54) Barone, P. W.; Baik, S.; Heller, D. A.; Strano, M. S. *Nat. Mater.* **2005**, *4*, 86.

(55) Ghosh, S.; Bachilo, S. M.; Simonette, R. A.; Beckingham, K. M.; Weisman, R. B. *Science* **2010**, *330*, 1656.

(56) Avouris, P.; Chen, Z.; Perebeinos, V. *Nat. Nanotechnol.* **2007**, *2*, 605.

(57) Li, B.; Cao, X.; Ong, H. G.; Cheah, J. W.; Zhou, X.; Yin, Z.; Li, H.; Wang, J.; Boey, F.; Huang, W.; Zhang, H. *Adv. Mater.* **2010**, *22*, 3058.

(58) Oro, J. de X. *J. Biol. Phys.* **2001**, *27*, 73.

(59) Sznitowska, M.; Dabrowska, E. A.; Janicki, S. *Int. J. Pharm.* **2002**, *246*, 203.

(60) Dukovic, G.; Wang, F.; Song, D.; Sfeir, M. Y.; Heinz, T. F.; Brus, L. E. *Nano Lett.* **2005**, *5*, 2314.

(61) Haggenmueller, R.; Rahatekar, S. S.; Fagan, J. A.; Chun, J.; Becker, M. L.; Naik, R. R.; Krauss, T.; Carlson, L.; Kadla, J. F.; Trulove, P. C.; Fox, D. F.; Delong, H. C.; Fang, Z.; Kelley, S. O.; Gilman, J. W. *Langmuir* **2008**, *24*, 5070.

(62) Brozena, A. H.; Moskowitz, J.; Shao, B.; Deng, S.; Liao, H.; Gaskell, K. J.; Wang, Y. *J. Am. Chem. Soc.* **2010**, *132*, 3932.

(63) Sirringhaus, H.; Kawase, T.; Friend, R. H.; Shimoda, T.; Inbasekaran, M.; Wu, W.; Woo, E. P. *Science* **2000**, *290*, 2123.

(64) Gracia-Espino, E.; Sala, G.; Pino, F.; Halonen, N.; Luomahaara, J.; Mäklin, J.; Tóth, G.; Kordás, K.; Jantunen, H.; Terrones, M.; Helistö, P.; Seppä, H.; Ajayan, P. M.; Vajtai, R. *ACS Nano* **2010**, *4*, 3318.

(65) Beecher, P.; Servati, P.; Rozhin, A.; Colli, A.; Scardaci, V.; Pisana, S.; Hasan, T.; Flewitt, A. J.; Robertson, J.; Hsieh, G. W.; Li, F. M.; Nathan, A.; Ferrari, A. C.; Milne, W. I. *J. Appl. Phys.* **2007**, *102*, 043710.

(66) Sen, A. K. *Coated textiles: principles and applications*; 2nd ed.; CRC Press, 2007.

(67) Lee, H. C. *Introduction to Color Imaging Science*; Cambridge University Press: Cambridge, 2004.

(68) Anderson, B. L.; Winawer, J. *Nature* **2005**, *434*, 79.

(69) Gilchrist, A. L. *Science* **1977**, *195*, 185.

(70) NewEgg http://www.newegg.com (accessed Mar 15, 2013).

(71) Shultis, J. K.; Faw, R. E. *Fundamentals of Nuclear Science and Engineering*; 1st ed.; CRC Press: Boca Raton, 2002.

(72) Dror, R. O.; Willsky, A. S.; Adelson, E. H. *J. Vis.* **2004**, *13*, 821.

(73) Joblove, G.; Greenberg, D. *SIGGRAPH Comput. Graph.* **1978**, *12*, 20.

(74) Schnapf, J.; Kraft, T.; Baylor, D. *Nature* **1987**, *325*, 439.

(75) Rossi, L.; Rohe, T.; Fischer, P.; Wermes, N. *Pixel Detectors: From Fundamentals to Applications*; Springer: Heidelberg, 2006.

(76) Bayer, B. E. Color Imaging Array. U.S Patent 3,971,065, 1976.

(77) Compton, J.; Hamilton, J. Color Filter Array 2.0 www.scribd.com (accessed Nov 4, 2011).

(78) *PowerShot SX110 IS Camera User Guide; Technical Manual*; 2011.

(79) Nienhuys, H.-K. Measuring monitor contrast ratios with a camera http://www.lagom.nl/lcd-test/contrast-ratio.html (accessed Jul 18, 2012).

(80) Magdassi, S. *The Chemistry of Inkjet Inks*; World Scientific Publishing Company: Singapore, 2010.

(81) Yun, H.; Hun Han, J.; Kim, S. *Polym. J.* **2012**, *44*, 1238.

(82) Pushparaj, V. L.; Shaijumon, M. M.; Kumar, A.; Murugesan, S.; Ci, L.; Vajtai, R.; Linhardt, R. J.; Nalamasu, O.; Ajayan, P. M. *Proc. Natl. Acad. Sci. U. S. A.* **2007**, *104*, 13574.

(83) Martinez, A. W.; Phillips, S. T.; Butte, M. J.; Whitesides, G. M. *Angew. Chem. Int. Ed. Engl.* **2007**, *46*, 1318.

(84) Siegel, A. C.; Phillips, S. T.; Dickey, M. D.; Lu, N.; Suo, Z.; Whitesides, G. M. *Adv. Funct. Mater.* **2010**, *20*, 28.

(85) Liana, D. D.; Raguse, B.; Gooding, J. J.; Chow, E. *Sensors* **2012**, *12*, 11505.

(86) Toale, B. *The art of Papermaking*; Davis: Philadelphia, 1983.

(87) Iamazaki, E. T.; Atvars, T. D. Z. *Langmuir* **2007**, *23*, 12886.

(88) Deng, S.; Zhang, Y.; Brozena, A. H.; Mayes, M. L.; Banerjee, P.; Chiou, W.-A.; Rubloff, G. W.; Schatz, G. C.; Wang, Y. *Nat. Commun.* **2011**, *2*, 382.

(89) Carrilho, E.; Martinez, A. W.; Whitesides, G. M. *Anal. Chem.* **2009**, *81*, 7091.

(90) Star, A.; Steuerman, D. W.; Heath, J. R.; Stoddart, J. F. *Angew. Chem. Int. Ed. Engl.* **2002**, *41*, 2508.

(91) Xu, J.; Zhao, W.; Ning, Y.; Bashari, M.; Jin, Z.; Xu, B.; Zhang, L.; Duan, X.; Chen, H.; Wu, F.; Xu, X. *J. Mol. Struct.* **2013**, *1036*, 274.